2miy

132893

Interhemispheric Comparison of Atmospheric Circulation

Features as Evaluated from NIMBUS Satellite Data

Annual Report

1 July 1972 — 30 June 1973

Grant NGR 06—002—098

DEPARTMENT OF ATMOSPHERIC SCIENCE

COLORADO STATE UNIVERSITY

FORT COLLINS, COLORADO

ANNUAL REPORT

for

Grant NGR 06-002-098

E. R. Reiter, Principal Investigator

1 July 1972 - 30 June 1973

Prepared by

E. R. Reiter, T. H. Vonder Haar, R. Adler

S. Srivatsangam and Alice Fields

Department of Atmospheric Science

Colorado State University

for

National Aeronautics and Space Administration

TABLE OF CONTENTS

1.0 Grant Objectives

1.1 Objectives During Previous Contract Period

In our last proposal covering the period of study 1 July 1972 to 30 June 1973 the following areas of research were outlined.

(i) Application of Ozone Results to Interhemispheric Circulation Studies

Because of cut-backs in funding this phase of our proposed research effort had to be abandoned. It would have entailed an expansion of Lovill's (1972) dissertation effort, to be conducted by a new graduate student. Funding has not been sufficient to allow the recruitment of a new student.

(ii) Atmospheric Flow Patterns from Radiance Data

Two Ph. D. level graduate students, Mr. R. F. Adler and Mr. S. Srivatsangam, have been successfully engaged in this problem area during the past year. Mr. Adler has presented a paper on preliminary results from his study at the recent annual AGU meeting in Washington, D. C. This paper has been accepted for publication in the Archives of Meteorology, Geophysics, and Bioclimatology. (See Semi-annual Progress Report, 1973.) Mr. Adler focussed his attention on potential and kinetic energies derived from satellite radiance data. These parameters describe well the behavior and variability of the general circulation of the atmosphere in the northern hemisphere. Hence we can assume that such quantities derived from satellite data can be computed for the regions of the southern hemisphere which normally lack conventional data.

A study by Mr. Srivatsangam describes the use of vorticity patterns based on conventional data fields to study the time and space variability of the general circulation. The procedures can and will be applied to geopotential heights derived from satellite data.

Preliminary computational results are very encouraging. We hope to put these computational procedures to a final reliability test during the proposed forthcoming contract period.

(iii) Circulation Inferences Based on Tropospheric Water Vapor Data

This proposed phase of our investigation also had to be abandoned because of lack of funds.

(iv) Complimentary EOLE Ballon Studies

EOLE data tapes have been received as requested. Mr. Robert Banta, M. S. degree candidate, has been engaged in designing smoothing techniques that allow interpolation between individual data points. For some time this study has been handicapped by an urgent requirement to check the tapes for data inconsistencies and errors. A second set of tapes which was provided to us recently, overcomes most of these problems. We have also established contacts with a group of researchers under Dr. Mintz of UCLA in order to avoid unnecessary research duplication in the use of EOLE data.

The subsequent progress report describes our major activities and findings with regard to paragraph (ii) of the grant objectives stated above. Work on the EOLE data tapes [objective (iv)] has been continued by Mr. Banta. Since analyses of these data carried out at UCLA have not yet been received, Mr. Banta proceeded to develop, and has completed, his own objective analysis techniques, including spline function fitting of data points. We should have concrete results of these analyses in support of objectives (ii) forthcoming by the end of our next reporting period.

2.0 Discussion of Results

2.1 A Comparison of Northern Hemisphere General Circulation Parameters Calculated from Conventional Data and from Structure Obtained from SIRS Data

2.11 Method

In order to examine the potentialities and limitations of making general-circulation-type calculations from structure obtained from satellite, multi-channel radiance data, a set of calculations is performed using two different sets of data. One data set consists of geopotential heights and thicknesses from the National Meteorological Center (NMC) northern hemisphere grid. The other data set consists of heights and thicknesses obtained from SIRS data. Calculations are made on a daily basis for the month of January, 1970. NMC data for 1200 GMT are used for each day. SIRS data for a 24-hour period centered on 1200 GMT is combined into one set of analyses for each day in order to obtain sufficient hemispheric coverage.

Thickness or temperature information is determined from the SIRS data by a regression technique. A linear, step-wise, least squared error, multiple regression technique is used. The dependent variables in the regression procedure are the thicknesses for the following layers: 1000-700mb, 700-500mb, 500-300mb, 300-200mb, 200-100mb, 100-50mb, 50-30mb and 30-10mb. The independent variables are the radiances of the eight SIRS channels. Separate regression equations are determined for each layer and for each of the following latitude zones: $20\text{-}40^\circ$, $40\text{-}60^\circ$ and $60\text{-}80^\circ$.

The regression technique is based on a comparison of thickness information and cloud-free radiance data. When the regression equations derived from the comparison are applied to other radiance data, only

cloud-free data are used. To eliminate cloud-contaminated data from the comparison data set and from the application of the regression equations, a simple, objective "cloud check" procedure is used. The "cloud check" procedure is based solely on the satellite radiance information.

The SIRS channels with weighting function peaks in the low troposphere (channels 1 through 3) are most affected by the presence of clouds. Channels with weighting function peaks in the stratosphere (channels 7 and 8) are only rarely affected by the presence of tropospheric clouds. The radiance in the window channel (channel 1, $k=899cm^{-1}$) in the absence of clouds is related to the surface temperature. In the presence of an overcast, the channel 1 radiance is a function of cloud-top temperature, which is, of course, lower than the surface temperature. Therefore, channel 1 radiances much below normal would indicate the presence of clouds. However, the radiance in channel 1 is highly variable even in the absence of clouds because of its dependence on the surface temperature. Large changes in channel 1 radiance occur along satellite tracks in the presence of sharp changes in surface characteristics. This is especially true along land-sea boundaries. Also, large diurnal changes are present in the channel 1 radiance because of large changes in surface temperature. Channels 2 and 3 are also affected by clouds, but are not so severely affected by surface characteristics as channel 1. Therefore, channels 2 and 3 are used for the "cloud check."

SIRS radiance data is eliminated as being cloud-contaminated when the observed radiance in both channels 2 and 3 is below critical values. The critical values for both channels are determined by a comparison of SIRS data and satellite video data and are a function of latitude and

season. Any data with both channel 2 and 3 radiances below the critical levels are eliminated as cloud-contaminated. The "cloud check" procedure is simple and certainly not foolproof. Some slightly cloud-contaminated data may still find their way into the final data set. The procedure as outlined above removes, on the average, about 15 percent of the original data points.

To obtain the regression coefficients, comparison sets of radiance and thickness data are developed. The observations are near-simultaneous and at, or close to, the same geographic position. In the northern hemisphere, for the layer 100 to 1000mb, the SIRS radiance data are matched with the National Meteorological Center (NMC) northern hemisphere fields. For satellite data occurring within three hours of NMC map time, the NMC grid point data are linearly interpolated to the satellite track position. For the layers above 100mb, station data are matched with the satellite radiance information. The station location must be within 180 nautical miles of the satellite position, and the satellite observation time must be within three hours of the station observation time.

The root-mean-square-errors for the thickness fields as produced by the regression technique for January 1970 are given in Table 1.

Geopotential heights for the SIRS-based data set are determined by summing the satellite-based thicknesses from a conventional (NMC) 1000mb height field. Geopotential heights are therefore determined at the following levels: 700mb, 500mb, 300mb, 200mb, 100mb, 50mb, 30mb, and 10mb.

10-30mb	88.4m	2.8°C
30-50mb	44.4m	3.0°C
50-100mb	48.0m	2.4°C
100-200mb	41.0m	2.0°C
200-300mb	29.4m	2.5°C
300-500mb	41.3m	2.8°C
500-700mb	36.5m	3.7°C
700-1000mb	57.2m	5.5°C

Table 1. Root-mean-square-errors by layer for January 1970.

General circulation parameters calculated include the zonal and eddy available potential energy (AZ and AE, respectively) and the zonal and eddy kinetic energy (KZ and KE, respectively). The calculations are made using a 5° by 5° latitude-longitude grid between 20°N and 80°N. The NMC data are linearly interpolated from the NMC grid to the latitude-longitude grid. The SIRS-based data are also linearly interpolated from satellite track positions to the latitude-longitude grid.

The formulations used in the calculations are as follows:

$$AZ = \sum_{i=1}^{8} \frac{[([T_i]_{\lambda})_{\phi}^{2}]_{\lambda,\phi}}{2[\sigma]_{\lambda,\phi}} \Delta p_i \qquad 1$$

$$AE = \sum_{i=1}^{8} \frac{[(T_i)_{\lambda}^{2}]_{\lambda,\phi}}{2[\sigma]_{\lambda,\phi}} \Delta p_i \qquad 2$$

$$KZ = \sum_{i=1}^{8} \frac{[[u_i]_\lambda^2 + [v_i]_\lambda^2]_{\lambda,\phi}}{2g} \Delta p_i \qquad 3$$

$$KE = \sum_{i=1}^{8} \frac{[(u_i)_\lambda^2 + (v_i)_\lambda^2]_{\lambda,\phi}}{2g} \Delta p_i \qquad 4$$

The notation follows that of Reiter (1969) with brackets representing an average over the subscripted variable and parentheses representing a deviation from the average. The summation is over the eight layers in the vertical. The variable T_i represents the mean layer temperature in the ith layer derived from the thickness, λ is longitude, ϕ is latitude, u_i and v_i are the usual scaler horizontal wind speeds, Δp_i is the pressure difference from the bottom to the top of the ith layer and $[\sigma]_{\lambda,\phi}$ is the hemispheric averaged static stability given by

$$[\sigma]_{\lambda,\phi} = \frac{-g}{1000^\kappa R} p^{1+\kappa} [\frac{\partial \theta}{\partial p}]_{\lambda\phi} \qquad 5$$

where θ is the potential temperature, g is the acceleration of gravity and R is the universal gas constant. The u_i and v_i in equations 3 and 4 are calculated using the geostrophic assumption. In this paper contributions to the total energy from individual layers will be noted by, for example, AE (300-500mb), the contribution to the total AE from the layer 300-500 mb.

The hemisphere-averaged stability of equation 5 is calculated separately for each layer, for each day, from hemispheric-averaged temperatures at the top and bottom of the layer. For example, in the

calculation of AE (300-500mb), hemispheric averages of the 300mb and 500mb temperatures are used. In the calculations based on the SIRS data, these temperatures are obtained by using a separate set of regression equations. These regression equations, with temperature at particular pressure levels as the dependent variable, are used only in the calculation of $[\sigma]_{\lambda,\phi}$.

2.12 Distribution of energy with height

The summations in equations 1 to 4 are the finite difference approximations to vertical integrations with limits $p = o$ and $p = p_s$, the surface pressure. The integrand is approximated by the term inside the summation divided by the ΔP_i for that layer. A plot of the integrand versus pressure indicates the relative contributions of the various layers to the total energy.

The average distribution of energy with height for January 1970 for the northern hemisphere calculated from both the NMC data and from the SIRS-derived data is given in figures 1 through 4. The figures are based on daily calculations averaged over the month. Figure 1 shows the vertical distribution of the integrand of zonal available potential energy (AZ). The AZ is a function of meridional temperature gradients; more precisely, it is a function of

$$([T_i]_\lambda)^2_\phi = \{[T_i]_\lambda - [T_i]_{\lambda,\phi}\}^2 \qquad\qquad 6$$

where $[T_i]_{\lambda,\phi}$ is the area-weighted hemispheric mean temperature in the ith layer. The expression in equation 6, which is the numerator in the expression for AZ in equation 1, represents squares of the deviations of longitudinally-averaged temperature from hemispheric-averaged

temperature. In general, the larger the meridional temperature gradient is, the larger AZ is.

The distribution of the integrand of AZ, as calculated from the satellite-based structure, clearly indicates the main features of the distribution as given by the curve based on NMC data. The major contribution to the total AZ comes from the tropospheric layers. The integrand is a maximum in the lowest layer (700-1000mb) in both curves. There is a sharp decrease in both curves in the magnitude of the integrand of AZ from the 300-500mb layer to the 200-300mb layer. The layers above 300mb contribute only slightly to the total average AZ. A relative maximum in the 50-100mb layer is noted by both calculations and the absolute minimum for both curves is in the highest layer, 10-30mb.

Although the curve in figure 1 that is based on SIRS-derived structure indicates the layers of greatest contribution to AZ, and above 300mb is nearly coincident with the NMC curve, below 300mb there is a systematic underestimation of the integrand by about 20 percent. This underestimation is related to a number of factors. A slight underestimation of the meridional temperature gradient results in an appreciable underestimate of the integrand of AZ. For example, if the actual meridional temperature gradient is a linear function of cos ϕ, an underestimation of the slope by 10 percent results in an underestimation of the term in equation 6 by 19 percent, because of the squaring of the deviations.

Another factor in the underestimation in the troposphere is the smoothness of the meridional temperature profile. Because of the squaring of terms in equation 1, the smoother the north-south temperature profile is, the smaller the AZ is. Between two profiles with the same
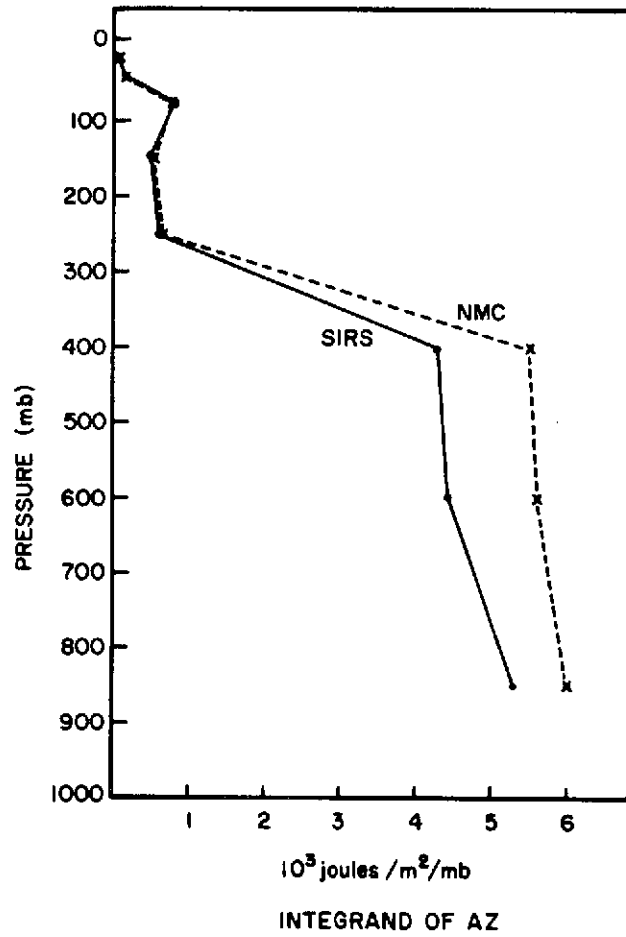
Fig. 1. Vertical distribution of the integrand of AZ for January 1970.

temperature change from equator to pole, the profile with the temperature gradient concentrated into a smaller latitude range has the largest value of AZ. Again a small difference in the smoothness can make an appreciable difference in the computation of AZ, because of the effect of squaring the term.

An examination of the meridional temperature gradients involved in the calculation of the integrand of AZ shows that the two factors just discussed are the major reasons for the underestimation of the integrand in figure 1 in the tropospheric layers. There is a slight systematic underestimation of the temperature difference between 20°N and 80°N. This underestimation is, in turn, related to both an under-estimation of low latitude temperatures and an overestimation of high latitude temperatures in the troposphere. The underestimation in the low latitudes is probably associated with the smoothing of the radiance field in low latitudes, which eliminates points of very high radiance in channels 1, 2, and 3 over land during the day. The overestimation of temperatures in high latitudes is probably related to the elimina-tion of some data points with very low radiance in channels 1, 2 and 3 as cloud contaminated when the low radiance is actually related to low temperatures and not the presence of cloud.

The results of the two calculations of the integrand of the eddy available potential energy (AE) are shown in figure 2. The integrand of AE calculated from SIRS-derived structure has a magnitude less than that calculated from NMC data at all levels, but the difference between the two curves decreases with height. The relative contribution of the various layers to AE is well depicted by the SIRS curve. The maximum contribution is from the lower layers, although the SIRS curve does not show the absolute maximum occurring in the lowest layer.
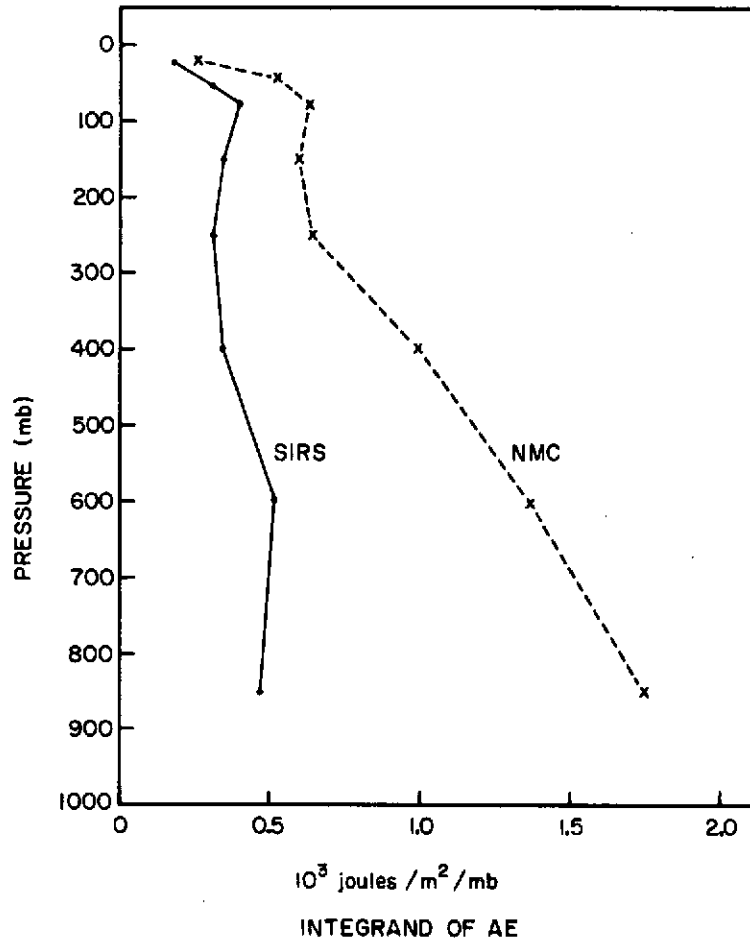
Fig. 2. Vertical distribution of the integrand of AE for January 1970.

There is a relative minimum in both curves near 200mb and a relative maximum in the lower stratosphere in the 50-100mb layer. The absolute minimum occurs in both calculations in the 10-30mb layer.

The underestimation of the integrand of AE from the SIRS-based data is much greater than the underestimation of AZ and occurs in both the troposphere and stratosphere. While AZ is a function of meridional temperature gradients, AE is a function of the variance of temperature around latitude circles. The underestimation of the integrand of AE is due to the underestimation of the amplitudes of waves in the temperature or thickness fields, or to the failure of features in the NMC fields to appear in the SIRS-derived fields. The failure to detect certain features is inherent in the distribution of useful satellite data. The distribution of satellite data also plays a part in the underestimation of wave amplitudes. Although a particular feature may be detected by the satellite data, the lack of a satellite pass directly over the center of the feature results in an underestimation of the amplitude. In addition, 24 hours of satellite data is combined to produce the daily fields from which the SIRS-based calculations are made. These calculations are compared to conventional data fields at a particular time (1200 GMT). If the conventional data fields were first averaged over 24 hours, the calculated values of AE would then be less because the averaging would reduce the amplitudes of moving waves.

The regression technique also tends to aid in producing smoother fields than the NMC fields. The thickness-radiance regression equations work very well near the mean thickness for that latitude band, but tend to underestimate deviations from the mean, producing slightly "smoothed-out" fields.

In addition to the effects discussed above which apply at all levels, in the lowest layers the distribution of satellite data, the slight smoothing of the radiance data and the effect of eliminating cloud-contaminated data combine to produce temperature fields which do not indicate the large east-west gradients that are present. The two calculations of the integrand of AE agree best at higher elevations. This is partly due to the decreasing effect of possible cloud effects, but more importantly due to the change in the character of the dominant waves with height. In the troposphere smaller, rapidly moving waves contribute significantly to AE; in the stratosphere larger, quasi-stationary, or slowly moving, waves dominate. The waves dominant in the stratosphere are much more easily detected and more accurately depicted because of the time and space distributions of the satellite data.

The vertical distribution of the integrand of zonal kinetic energy (KZ) is shown in figure 3. The calculations for the SIRS curve are based on height fields produced by adding SIRS-derived thickness fields to an NMC hemispheric 1000mb height field. The SIRS-based calculation slightly underestimates the integrand of KZ at all levels except 700mb. The underestimation is tied to the slight underestimation and smoothing of the meridional temperature gradient in the troposphere. The vertical distribution of the integrand is well defined by the SIRS-based calcu-lation. From an absolute minimum at 700mb, the integrand increases to a peak at 200mb in both curves. Above 200mb there is a decrease with height to a relative minimum at 30mb, above which there is a small increase to 10mb.

Figure 4 shows the integrand of eddy kinetic energy (KE) for both calculations. The two values are nearly identical at 700mb. This
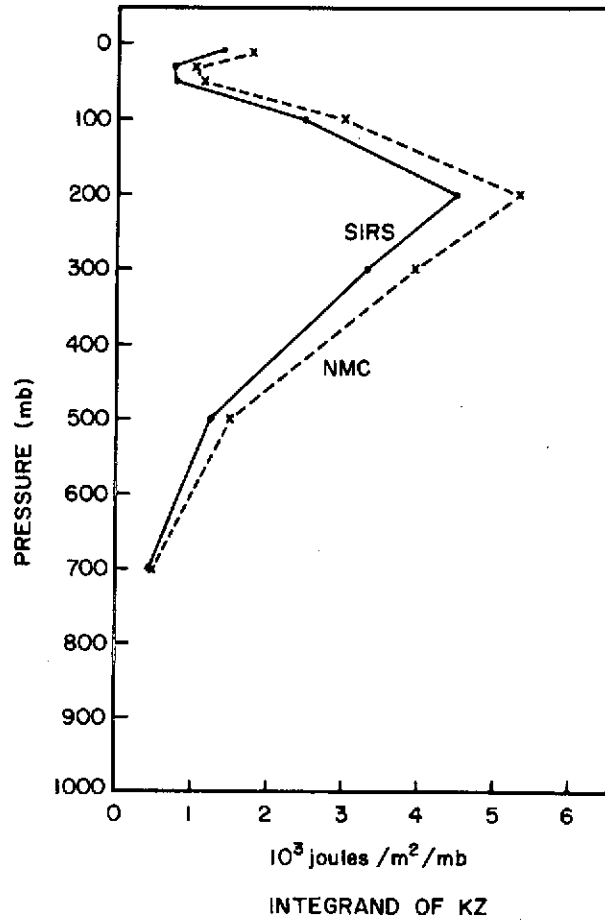
Fig. 3. Vertical distribution of the integrand of KZ for January
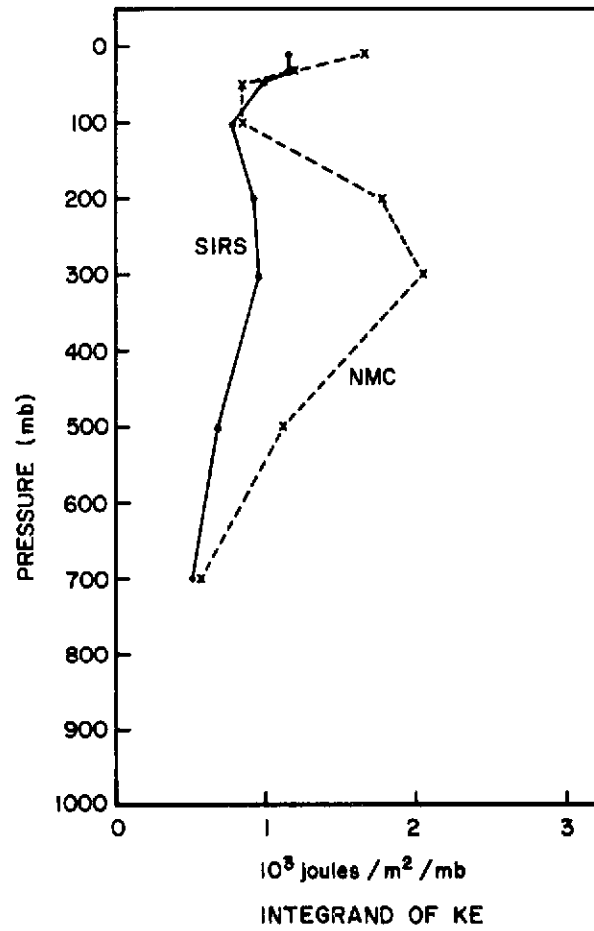1970.

Fig. 4. Vertical distribution of the integrand of KE for January 1970.

agreement at 700mb is due to the use of the NMC 1000mb height field.
Above 700mb both curves indicate an increase to a maximum at 300mb, a
decrease to a relative minimum in the lower stratosphere and a slight
increase above that. There is an underestimation of the integrand of
KE in the troposphere and lower stratosphere with the maximum under-
estimation occurring at 300mb. This underestimation is related to the
underestimation of the amplitude of features in the thickness fields
in the troposphere.

2.13 Time variation of energy

In this section the time variations during January 1970 of various
energy parameters, as calculated from both the conventional and
satellite data, are compared. In the figures to be presented, three-
day running means are used to smooth out small time-scale fluctuations.
In addition to the smoothing of the three-day running means, seven days
are eliminated from the SIRS representation because of insufficient
hemispheric data coverage. The elimination is based on the number of
locations in the five-by-five latitude-longitude grid that are originally
filled with satellite data. The days eliminated are January 1, 5, 13,
21, 26, 28, 31.

Figure 5 shows the time variation of the contribution to AZ from
the 300-500mb layer, AZ (300-500mb). The systematic underestimation by
the satellite-based technique discussed in relation to figure 1 is
again evident. The times of relative maxima and minima agree between
the two curves, and the magnitudes of changes in time are comparable.
The contribution from the same layer, 300-500mb, to AE is shown in
figure 6. The large underestimation by the SIRS-based calculation is
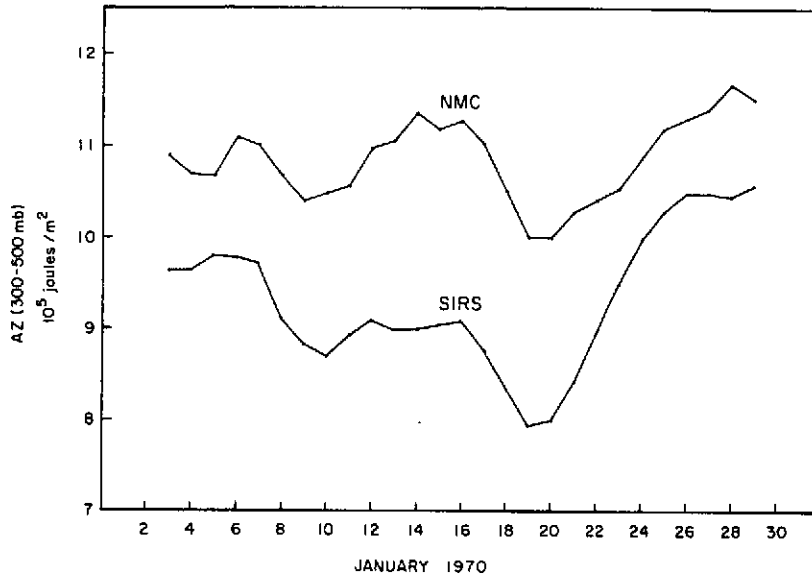obvious. The agreement between the two curves in regard to changes
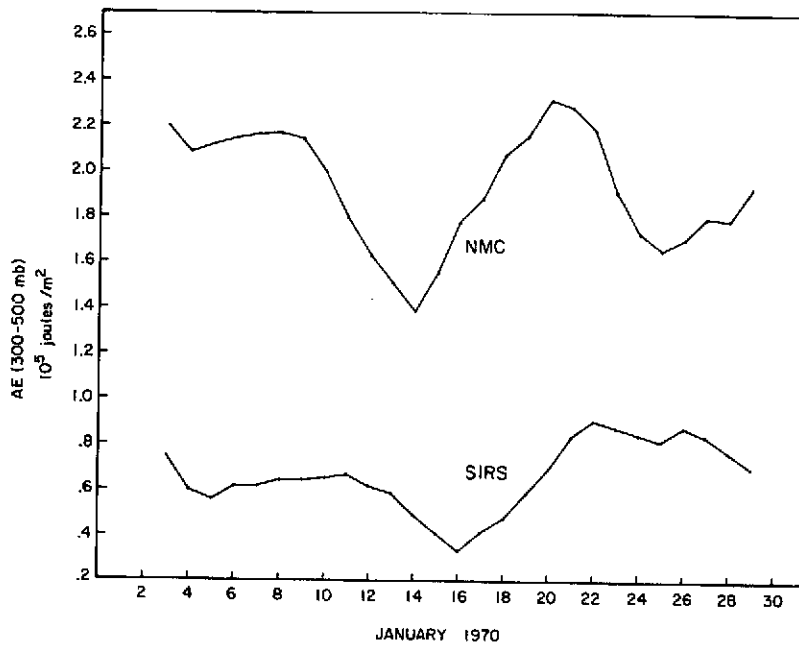
Fig. 5. Time variation of AZ (300-500 mb).

Fig. 6. Time variation of AE (300-500 mb).

with time is poor, compared to the previous figure for AZ (300-500mb).
Major changes are, however, indicated. After a very small decrease at
the beginning of the month, a period of nearly constant, or slightly
increasing, AE (300-500mb) is present from January 4. On the NMC curve
a period of sharp decrease begins about January 9. On the SIRS curve
this decrease does not commence until January 11. The minimum at the
end of this decrease is also delayed in the SIRS curve by two days.
After this minimum, both curves show a large increase to the maximum
value for the month, occurring in the NMC curve on January 20, and in
the SIRS curve on January 22. The cause of this two-day phase differ-
ence is unknown. The last ten days of the month are marked on the NMC
curve by a decrease, then a smaller increase, resulting in a small
net decrease over the last ten days. The SIRS curve also shows a
small decrease over that period, but completely misses the relative
minimum shown in the NMC curve.

The time variations of tropopause level zonal and eddy kinetic
energy are shown in figures 7 and 8 respectively. The zonal kinetic
energy shown in figure 7 is based on 200mb heights, and the eddy
kinetic energy on 300mb heights. These levels are selected because
they are the levels of maximum contribution to the vertically inte-
grated total (see figures 3 and 4). KZ (200mb) actually represents
the contribution from the 150-250mb layer, and KE (300mb) represents
the contribution from the 250-400mb layer. The SIRS curve for KZ (200mb)
compares well with the NMC curve, except in the first ten days of the
month. The increase at the beginning of the month in the NMC curve
is not indicated in the SIRS curve. The analysis during the first ten
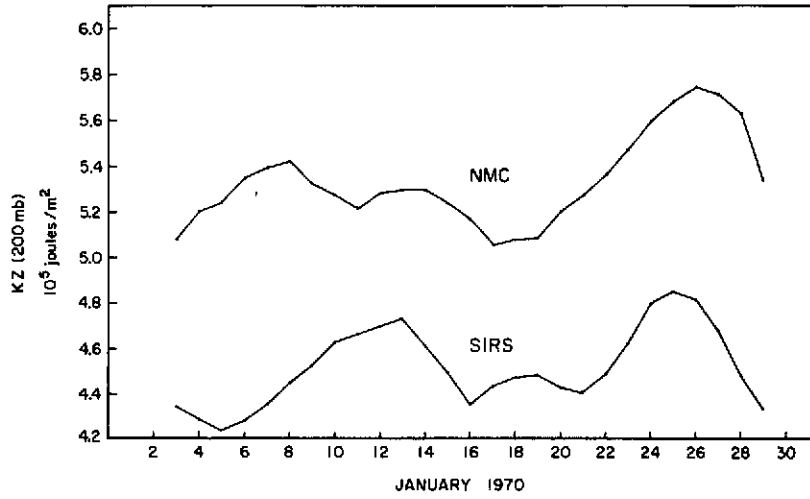days of the month is hindered by a lack of NMC data on January 7 and 8.

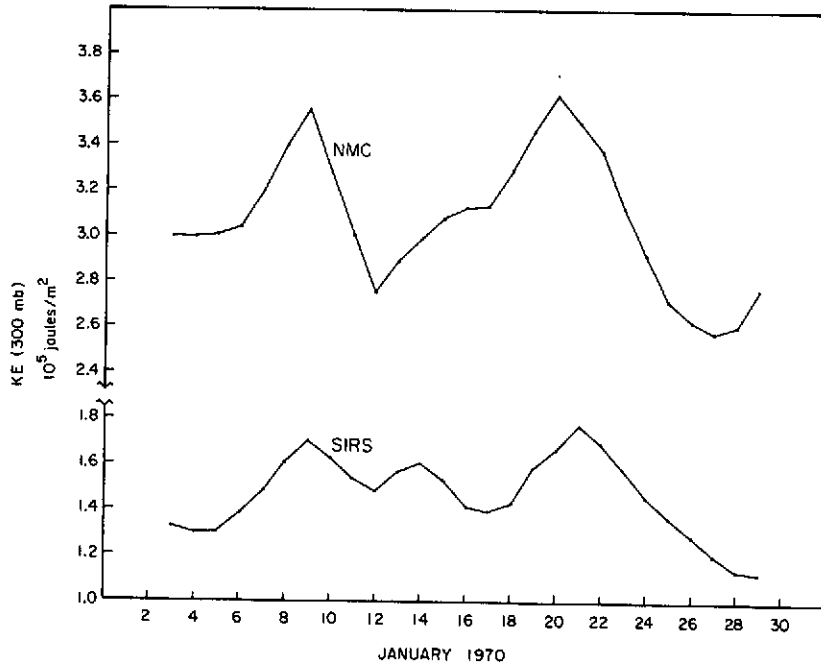Fig. 7. Time variation of KZ (200 mb).

Fig. 8. Time variation of KE (300 mb).

This produces data gaps for those days in the KE and KZ fields for both the NMC-based and SIRS-based calculations. The SIRS-based calculations use the NMC 1000mb height field. The gaps are filled by linear interpolation. A broad minimum centered about January 18 and a maximum on January 25-26 are indicated on both curves. The curves for KE (300mb) in figure 8 compare well, despite the large systematic underestimation. Peaks at January 9 and 20 on the NMC curve also occur on the SIRS curve. Large changes in KE (300mb) during the month are also identified by the SIRS-based curve.

The underestimation of the integrand of AE varies strongly with height (figure 2), decreasing sharply up to the 200-300mb layer, remaining approximately constant above that layer. The underestimation in the 100-200mb layer is 42 percent. The 100-200mb layer also has the lowest root mean squared error for the regression equations for January, 1970 (see Table 1). The time variation of the contribution of this layer to the AE is shown in figure 9. The agreement between the two curves for AE (100-200mb) is good in respect to major features. The 100-200mb layer is probably the optimum layer for comparison. Above this height the amount of conventional data going into the NMC analysis decreases.

Figures 10 through 13 show the time variation comparison for the stratospheric layers. For the available potential energy calculations, the three top layers (10-30mb, 30-50mb and 50-100mb) are used. For the kinetic energy calculations, the 10mb, 30mb and 50mb height fields are used. These three levels combined represent the layer 0-75mb. The AZ (10-100mb) in figure 10 shows the SIRS-based calculation systematically overestimating the NMC-based values by a very small amount (10 percent). Trends, maxima, and minima are well identified by the
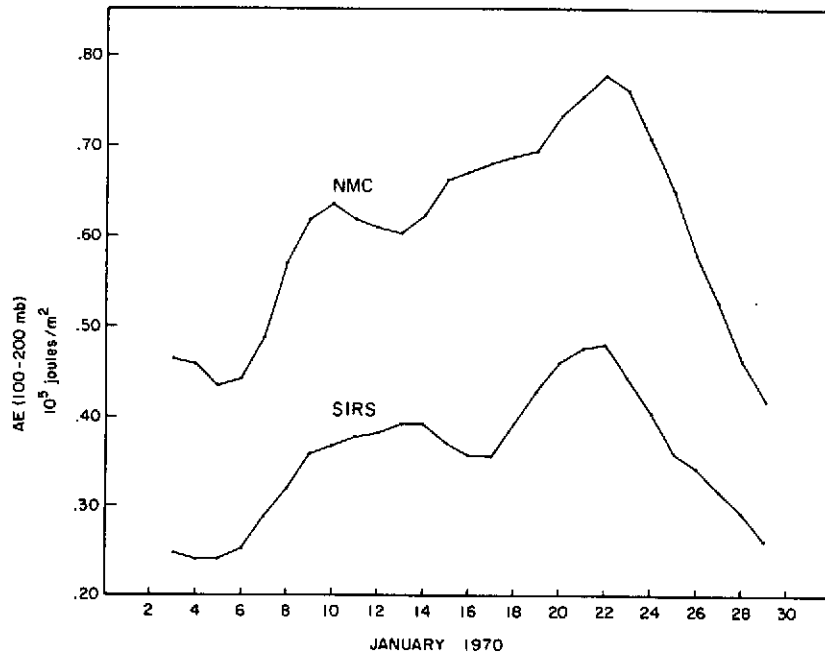
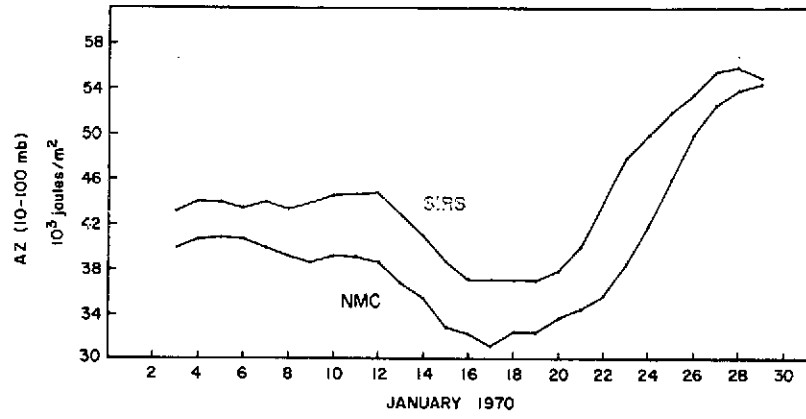Fig. 9. Time variation of AE (100-200 mb).
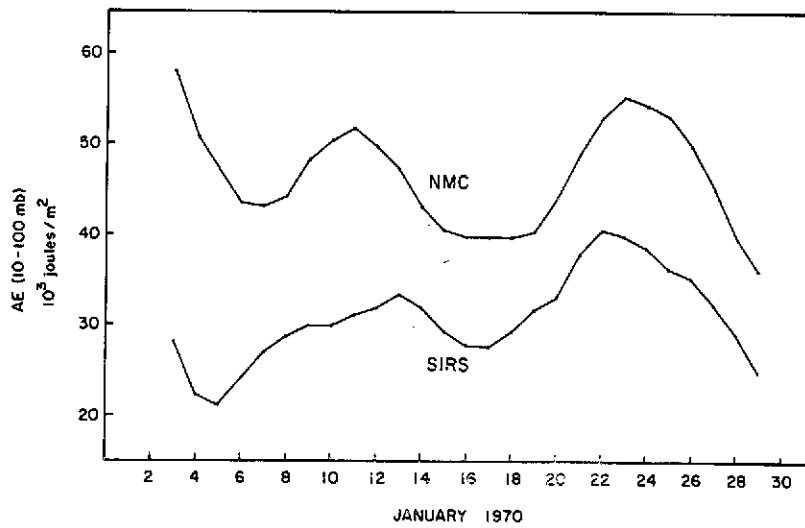
Fig. 10. Time variation of AZ (10-100 mb).

Fig. 11. Time variation of AE (10-100 mb).

SIRS-based calculation. The curves for AE (10-100mb) in figure 11

show the usual underestimation by the SIRS calculation. The curves

also parallel each other fairly well. The curves for KZ (0-75) in

figure 12 also parallel each other well, with the only real major change

being the sharp increase from January 18 to the end of the period. The

curves for KE (0-75mb) in figure 13 both show a decrease from early in

January to the end of the month. The maximum and minimum values for

the month occur at the same time in both computations. However, the

SIRS curve displays values which underestimate the NMC-based values

early in the month and slightly overestimate the NMC-based values after

mid-month. This occurrance is a result of a combination of factors.

During the early part of the month, east-west temperature gradients

in the stratosphere were underestimated for a greater extent than

later in the month, as evidenced in figure 11. This greater under-

estimation in the early part of the month in the temperature or thickness

field results in an underestimation of the KE. Another problem, which

reveals itself in the later part of the month, is a slight noisiness

in the height fields in the stratosphere, related to the accumulation

of small errors from the summing of the thicknesses from 1000mb. The

calculation of KE is most sensitive to this noisiness because of the

finite difference approximations using differences between adjacent

points.

2.14 Distribution of energy in wavenumber domain

In this section harmonic analyses of thermal structure and

kinetic energy based on the two sets of data are compared. The analyses

are based on thickness and height data every ten degrees of longitude.

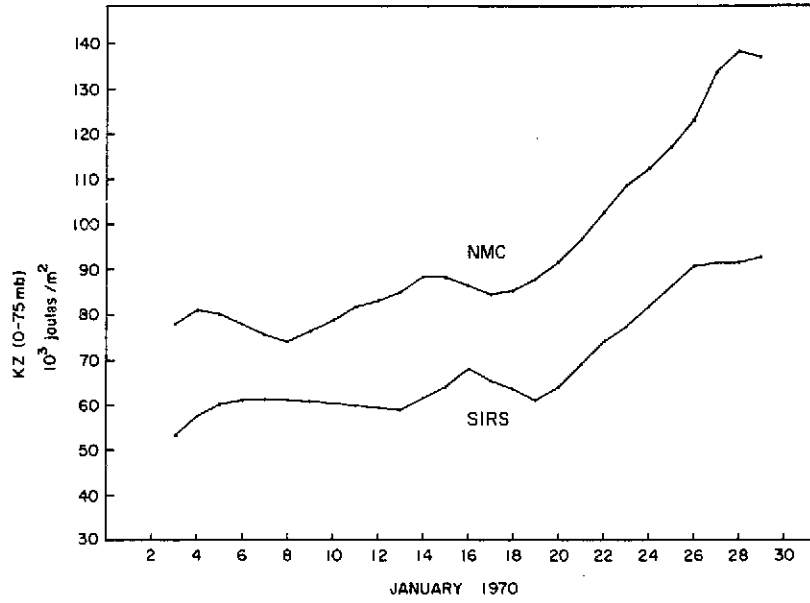The u and v components are computed using the geostrophic assumption
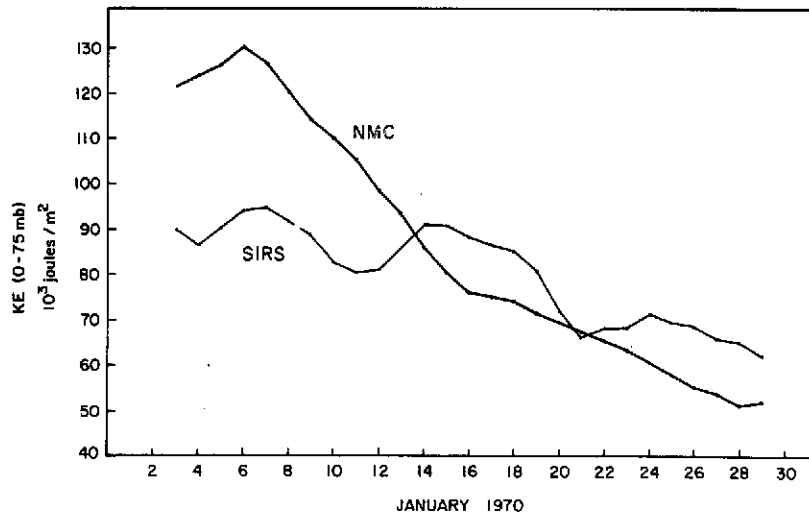
Fig. 12. Time variation of KZ (0-75 mb).

Fig. 13. Time variation of KE (0-75 mb).

The u component is calculated from heights 5° to the north and south of the latitude of analysis. The harmonic analyses are performed on data for 30°, 50° and 70° N. The analysis of thickness or temperature is carried out for three layers: 300-500mb, 100-200mb and 30-50mb. The 200mb surface and 30mb surface are the levels for which the kinetic energy analyses are made.

The results of the harmonic analyses of the temperature fields for the layers 300-500mb, 100-200mb and 30-50mb at 50^ON are shown in figures 14, 15 and 16 respectively. The variance explained, $\frac{T_k^2}{2}$, by each wavenumber k is plotted against k. The variance of temperature around a latitude circle is related to the eddy available potential energy (see equation 2). The harmonic analysis of temperature around latitude circles gives an indication of the relative contribution of various wavenumbers to the eddy available potential energy. In all three figures the SIRS-based computations accurately depict the wavenumbers of greatest influence. The agreement between the NMC-based analysis and the SIRS-based analysis is especially good in the two upper layers. For the 300-500mb layer (figure 14) the SIRS-based computation does indicate that wavenumbers 1 and 2 are the principle contributors to the total variance, but does not indicate the peak at k=2 that appears in the NMC curve. In the 100-200mb layer (figure 15) and the 30-50mb layer (figure 16) the maximum contribution is at k=1 in both the NMC-based and SIRS-based curves. The relative contribution of the other wavenumbers is also indicated well.

The underestimation of amplitudes that is evident from results presented in previous sections, also occurs in the results of the harmonic analyses. The percentage underestimation in general, increases
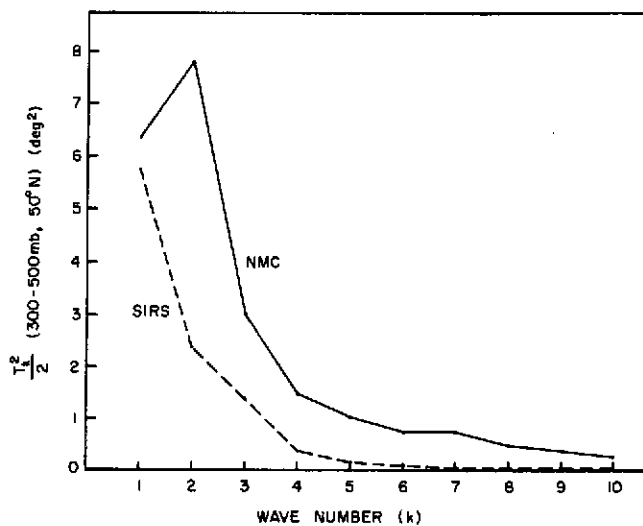
Fig. 14. Mean wave number spectra for January 1970 of the variance of temperature in the layer 300-500 mb, at 50° N.
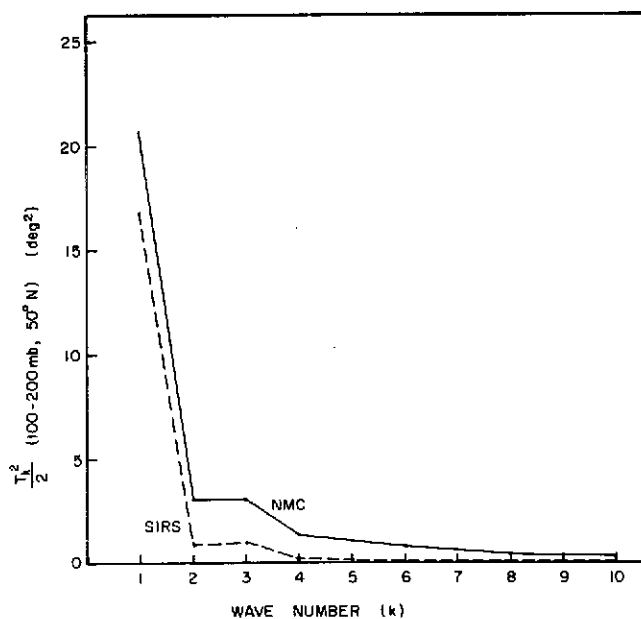

Fig. 15. Mean wave number spectra for January 1970 of the variance of temperature in the layer 100-200 mb at 50° N.
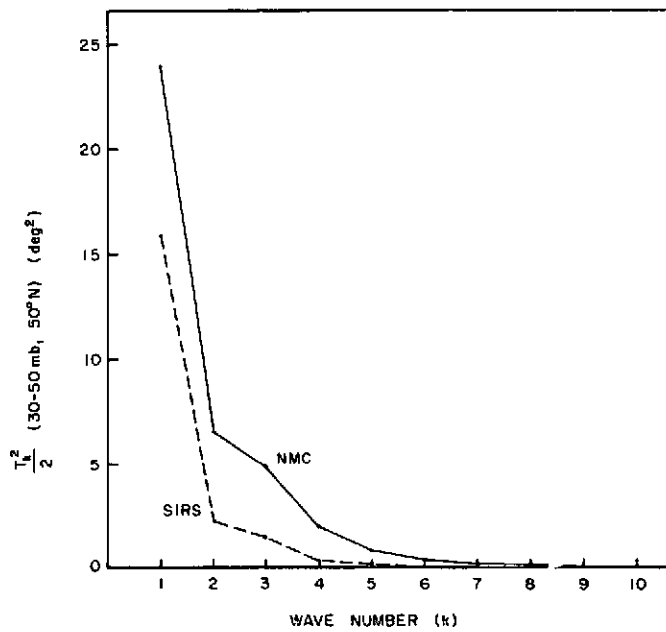
Fig. 16. Mean wave number spectra for January 1970 of the variance of temperature in the layer 30-50 mb, at 50° N.

with increasing wavenumber in all three layers. In other words the low

wavenumber waves are better represented than the waves with larger k.

Because the variance in the 100-200mb layer is concentrated in wave-

number 1, and wavenumber 1 is well defined by the SIRS-based analysis,

the major time variations of AE (100-200mb) as shown in figure 9 are

reproduced very well. However, in the 300-500mb layer there is a

significant contribution to the variance from the first few wavenumbers.

Although the underestimation for k=1 is small, for k=2, 3, 4 the

underestimation is larger, especially for k=2. The problems noted in

the time variation of AE (300-500mb) in figure 6 may be related to the

importance of shorter wave lengths in this layer.

The kinetic energy is evaluated at 200mb and 30mb. Figures 17 and

18 show the variance of u and v respectively at 200mb at 30°N. The

maximum contributor to $u^2/2$ is wavenumber 1, as indicated by both the

SIRS-based and NMC-based curves. The maximum contribution to the

meridional flow kinetic energy is from the synoptic-scale wavenumbers.

The NMC-based curve shows a broad maximum from k=5 to k=7 with a peak

at k=7; the SIRS-based curve shows a peak at k=6. The results of the

30mb analysis are given in figures 19 and 20. At 30mb the major

contribution to $u^2/2$ is made by wavenumber 1, and the major contribu-

tion to $v^2/2$ is made by wavenumbers with k=1 through 3. The major

features of the NMC-based distributions also occur in the SIRS-based

curves. An interesting feature of the curves for 30mb is that at

higher wavenumbers the values on the SIRS curves are higher than those

on the NMC curves. In figure 19 for the zonal component the overestima-

tion by the SIRS-based technique begins at k=2; for the meridional

component the overestimation begins at higher wavenumbers. This over-

Fig. 17. Mean wave number spectra for January 1970 of $u^2/2$ for 200 mb, at 30° N.

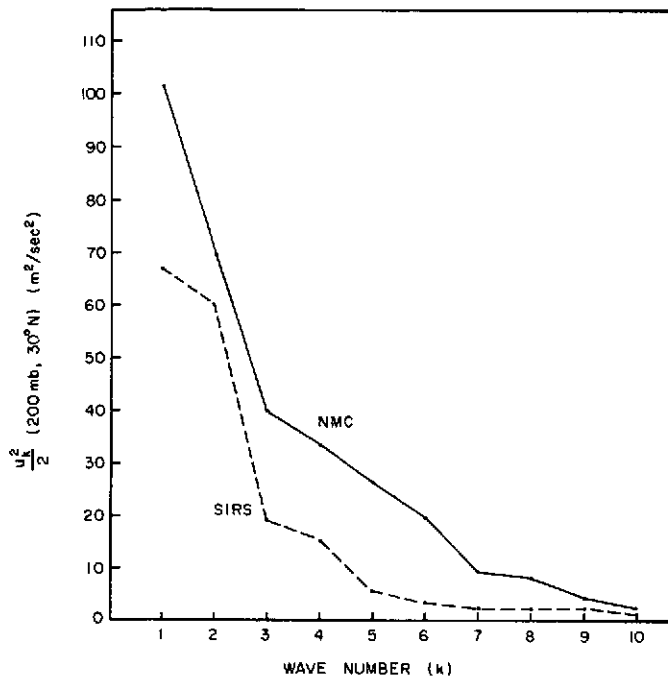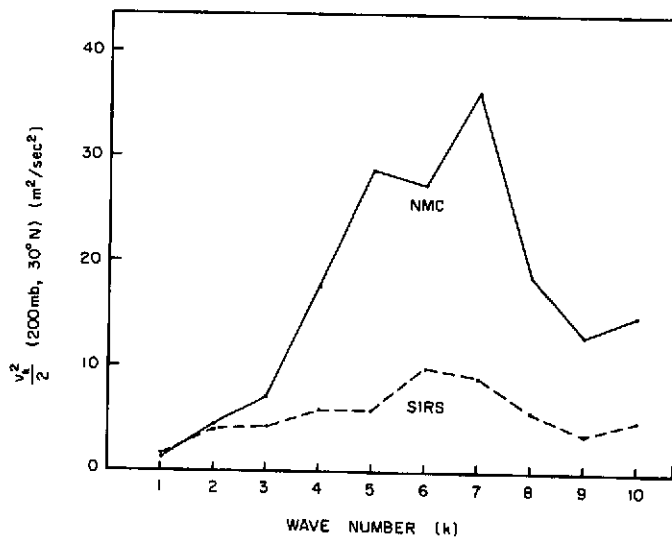Fig. 18. Mean wave number spectra for January 1970 of $v^2/2$ for 200 mb, at 30° N.
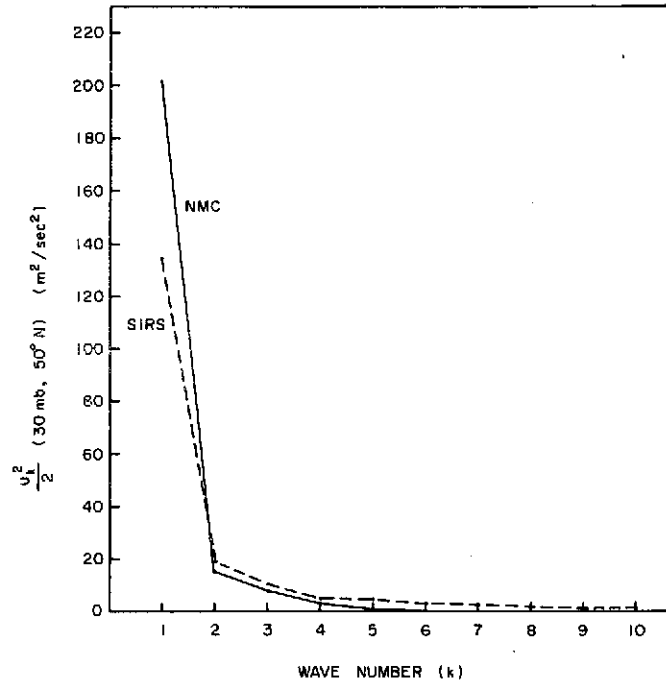
Fig. 19. Mean wave number spectra for January 1970 of $u^2/2$ for
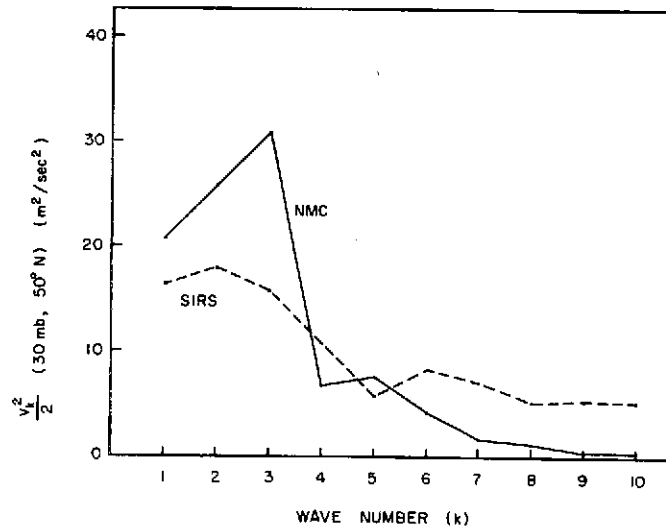30 mb, at 50° N.

Fig. 20. Mean wave number spectra for January 1970 of $v^2/2$ for
30 mb, at 50° N.

estimation is due to an accumulation of small errors during the summing of the thickness fields to produce the height fields. The overestimation does not occur in the individual layers (see figure 16). The overestimation of the energy in larger wave lengths explains the appearance of figure 13, the changes with respect to time of the eddy kinetic energy in the 0-75mb layer. In the early part of the month the eddy kinetic energy is large and is dominated by low wavenumbers. As the energy in these wavenumbers decreases, the total decreases until the overestimation by the SIRS-based technique of the energy in the higher wavenumbers produces an overestimation in the total energy.

The distribution of kinetic energy at 200mb with respect to wavenumber of the standing eddies for January, 1970 is shown in figures 21 and 22. The zonal component (figure 21) has its greatest contribution made by wavenumbers 1 and 2. The meridional component (figure 22) has a peak at k=2 and another around k=5 or 6. These major features occur in the results of both sets of calculations. The percentage of the total variance contributed by the standing eddies as a function of k is shown for the temperature distribution in the three layers in figures 23 through 25. The ratio of standing to total kinetic energy for 200mb is shown in figure 26. The main features of the curves based on the NMC fields are evident also in the SIRS-based technique. This underestimation is probably related to the analysis of the satellite data in producing daily maps. For the satellite data each day's map is analyzed independently. The NMC analysis, however, is accomplished using information from prior analyses, thus tending to reproduce standing features slightly more accurately.

One very significant difference between the NMC-based curves and the SIRS-based curves occurs in figure 24 at k=2. The magnitude of the
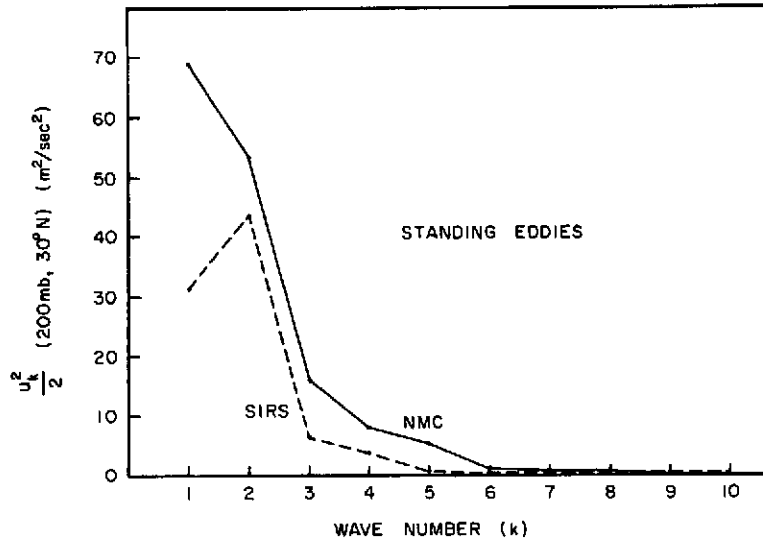
Fig. 21. Mean wave number spectra for January 1970 of $u^2/2$ for standing eddies for 200 mb, at 30° N.
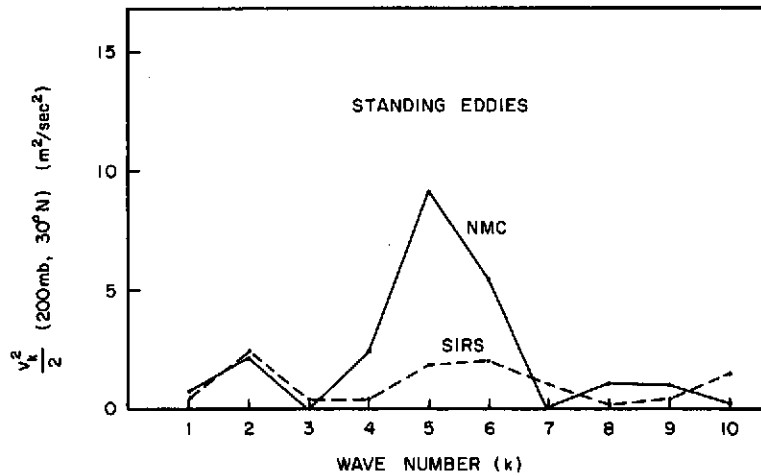
Fig. 22. Mean wave number spectra for January 1970 of $v^2/2$ for standing eddies for 200 mb, at 30° N.

34
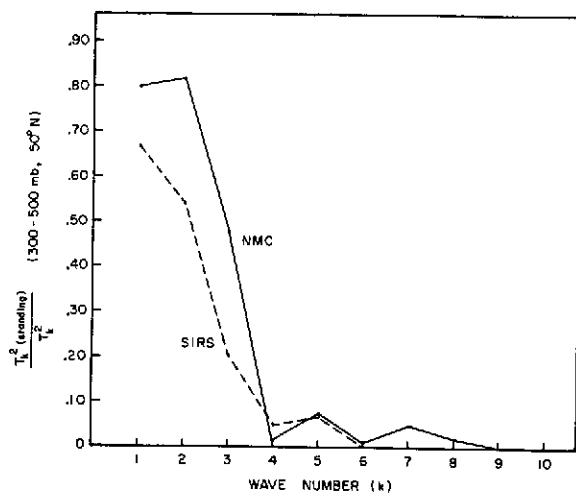
Fig. 23. Ratio of standing eddy variance to total variance as a function of k for temperature in the layer 300-500 mb, at 50° N.
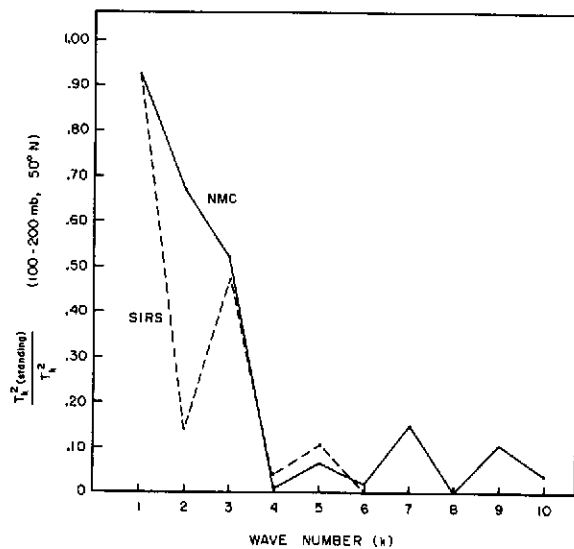
Fig. 24. Ratio of standing eddie variance to total variance as a function of k for temperature in the layer 100-200 mb, at 50° N.
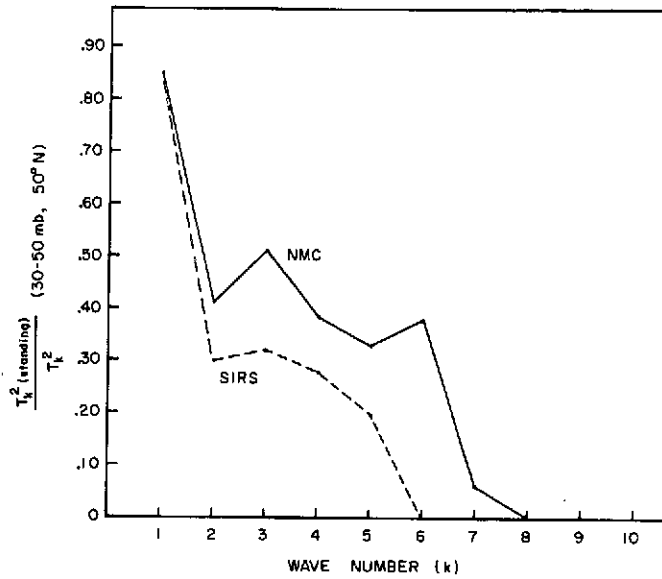
Fig. 25. Ratio of standing eddy variance to total variance as a
function of k for temperature in the layer 30-50 mb, at
50° N.
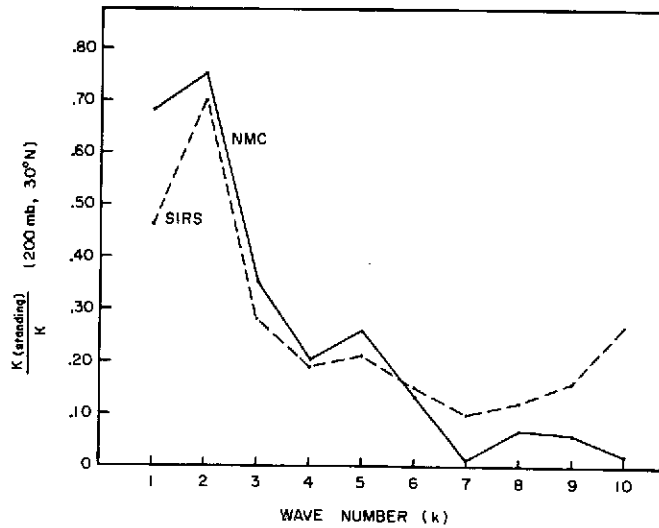
Fig. 26. Ratio of standing eddy kinetic energy to total eddy kinetic
energy as a function of K for 200 mb, at 30° N.
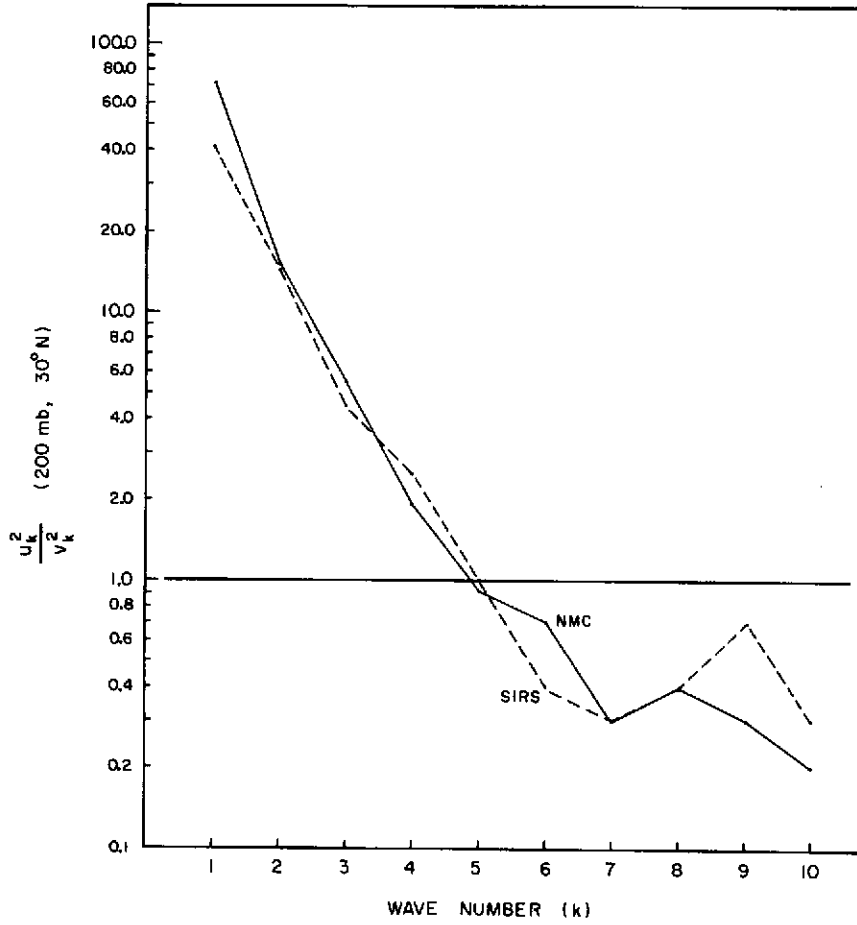
Fig. 27. Anisotropy (u_k^2/v_k^2) as a function of k for 200 mb, at 30° N.

standing contribution is grossly underestimated. The cause of this large discrepency is unknown.

The anisotropy of the horizontal flow at 200mb as indicated by the ratio u^2_k/v^2_k averaged over the month is shown in figure 27 for both the NMC-based and SIRS-based computations. The zonal component dominates in the low wavenumber region with the ratio decreasing rapidly with increasing k. The meridional component dominates at and above k=6. The NMC and SIRS curves agree very well.

2.2 General Circulation of the Extratropics in Terms of Vorticity

In Appendices I and II analyses of the distribution of vorticity in the lower atmosphere are presented. These analyses were made using the geopotential height data for July and October, 1969 and January and April, 1970 on the National Meteorological Center (NMC) data tapes. As this period corresponds to the period for which Infrared Interferometer Spectometer (IRIS) and Satellite Infrared Spectometer (SIRS) data are available with us, comparisons between the two types of data (conventional and satellite) could be made. At the present time these comparisons are being made for the Northern Hemisphere to ascertain the nature of errors which might be introduced into the satellite spectrometric data by the presence of clouds in the field of observation. This would enable proper interpretation of the spectometrically-derived data in the Southern Hemisphere.

The vorticity studies, whose results are presented in Appendices I and II, are the results of an attempt to represent the normal state of the lower atmosphere in the extratropics. Since vorticity is a parameter which represents eddies both in their shear and curvature aspects, it was considered that the root mean square (r.m.s.) values of geostrophic

relative vorticity would be a parameter capable of representing the normal state of the usually disturbed extratropical atmosphere. [It might be noted here that recently greater theoretical attention is being paid to the parameter enstrophy (one-half the vorticity squared). According to Leith (1968) two-dimensional turbulence is characterized by the conservation of enstrophy, which also happens to have a simple spectral representation. The conservation of enstrophy leads to the formulation of two inertial ranges in the spectrum of atmospheric eddies, one of which has a null flux of enstrophy and the other a null flux of kinetic energy.]

The greater applicability of the parameter K (the temporal mean of the zonal r.m.s. values of vorticity) to the normal representation of atmospheric motions in the extratropics is also evident from a comparison of the values of K above and below the 300 mb level in October, 1969 and April, 1970 in the midlatitudes (Appendix II, Figures 3b, 3d). This comparison reveals that although the upper troposphere is characterized by larger values of K in October, 1969, in the lower troposphere the values of K are smaller than in April, 1970. Hence it might be concluded that horizontal eddy activity is greater in the lower troposphere in the middle latitudes in April, compared to October; the reverse is true of the upper troposphere. These conclusions agree well with analyses of large-scale exchange coefficient values computed using 5 years of geopotential height data for ninety-eight North American radiosonde stations by Chen (1973). This observed reversal is not found in the eddy kinetic energy data presented by Oort and Rasmusson (1971).

From these vorticity studies it is shown that in addition to the semipermanent lows and highs in the extratropics there are regions where

maxima of temporal r.m.s. values of vorticity are present at the 300 mb level; the magnitudes of these maxima are comparable, but not their constitution. An analysis of the componental constitution of the oceanic and continental maxima of the temporal r.m.s. values of ζ_g reveals that the oceanic maxima are constituted largely of transient eddies and the continental ones of stationary eddies, in July. In all the other three months analyzed the reverse is true.

The vorticity studies also reveal the organization of the meanders of Extratropical Frontal Jet Streams and their seasonal migrations.

2.3 The Comparative Stabilities of the Arctic and Antarctic Polar Night, Stratospheric Vortices

2.31. Background

The winter-time stratospheric polar vortices of the northern and southern hemispheres exhibit drastically different breakdown climatologies. In most years the northern hemisphere vortex breaks down completely in mid-winter. Often the vortex never becomes re-established. A detailed summary of events during northern hemisphere breakdowns is given by Reiter (1969). The Antarctic vortex, on the other hand, has not been observed to undergo the complete, mid-winter breakdown typical of the Arctic vortex, although mid-winter minor warmings have been observed (Labitzke and Van Loon, 1972). The final, complete breakdown of the Antarctic vortex does not occur until spring.

This difference in breakdown characteristics between the two hemispheres has not been completely explained. Case studies of northern hemisphere breakdowns have shown that the main source of energy for the

breakdowns in the stratosphere is an eddy flux of energy from the tropo-
sphere. The waves which are important in the vertical flux into the
stratosphere are the very long, slowly moving, or stationary, waves.
In the northern hemisphere during the winter, stationary wave numbers
two and three are prominent even in the climatological fields. These
stationary waves are associated with the distribution of geography and
orography in the northern hemisphere. In the southern hemisphere mid-
latitudes, the land-sea variation is essentially non-existent, and the
orographic barriers are minor compared to those in the northern hemi-
sphere. The effect of this rather uniform surface is a relative lack
of standing eddies in the southern hemisphere. This relative lack of
standing eddies may result in a lack of upward propagation of energy
from the troposphere to the stratosphere in the southern hemisphere.
Since this flux of energy has been identified as the major source of
energy for the northern hemisphere breakdowns, the lack of standing
waves in the southern hemisphere may be related to the lack of mid-
winter breakdowns in the southern hemisphere.

Another possible, and perhaps complementary, explanation for the
differences in breakdown characteristics between the hemispheres is a
difference in the stability of the vortices in the two hemispheres.
Considering a fluid with both horizontal and vertical shears, Charney
and Stern (1962), Pedlosky (1964), and Mahlman (1966) derive essentially
identical stability criteria. Charney and Stern (1962) and Mahlman
(1966) apply their criteria to the stratospheric polar vortex. As
derived in these studies, the necessary condition for instability is that
the latitude profile of potential vorticity, $P = (-\frac{\partial \theta}{\partial p})(\zeta_\theta + f)$, must
have a relative maximum or minimum. In other words, $\frac{\partial}{\partial \phi}[(-\frac{\partial \theta}{\partial p})(\zeta_\theta + f)]$

must be zero at some point in the latitude profile. In the expression

for the potential vorticity, θ is the potential temperature, p is pressure,

ζ_θ is the relative vorticity on an isentropic surface and f is the

coriolis parameter.

Both Charney and Stern (1962) and Mahlman (1966) show latitude pro-

files of potential vorticity for case studies just before breakdowns of

the vortex in the northern hemisphere. Both cases show that the

instability criterion is met. A relative maximum in P is located just

poleward of the jet axis. The latitude profiles of the components of the

potential vorticity, the static stability $(-\frac{\partial \theta}{\partial p})$ and absolute vorticity

$(\zeta_\theta + f)$, indicate that the profile of static stability is of primary

importance in meeting the instability criterion (Mahlman, 1966). While

the profiles of absolute vorticity show a continuous increase with

increasing latitude, the static stability shows a sharp decrease from

the jet axis poleward. If the static stability had remained constant

with latitude, the instability criterion would not be met. Thus the

distribution of static stability with latitude is of particular interest

in the breakdown of the polar vortex.

2.32. Arctic and Antarctic Polar Vortex Structure

The latitudinal distribution of static stability is quite different

in the stratospheric polar vortices of the northern and southern

hemispheres. In mid-winter, poleward of the axis of the stratospheric jet,

the stability decreases toward the pole in the northern hemisphere.

Figure 28 shows the distribution with latitude of static stability in

the layer 50-100 mb. The solid line indicates the latitude profile

obtained from January mean cross-sections presented by Craig (1965).

The cross-sections are based on four years of data. The decrease of stability with latitude is evident. Because vortex breakdowns often occur during January, the January mean maps are not the best examples of pre-breakdown conditions. The dashed line in Figure 1 displays an example calculated by Mahlman (1966) of the stability profile before the onset of a major breakdown in 1958. A sharp decrease with latitude is again present, with the value of static stability of 90°N being about 17% less than that at 70°N.

The mid-winter structure for the southern hemisphere is given in Figure 29. The dashed line gives conditions in the 50-100 mb layer in July 1957 from station data presented by Taylor (1961). The stability at 90°S is calculated from July 1957 mean temperatures for station Amundsen-Scott. The point plotted at 69° is an average of conditions at Cape Hallett (72°S, 170°E) and Wilkes (66°S, 111°E). The static stability is nearly constant with latitude. The static stability profile for July 1969 for the layer 30-50 mb is given by the solid line in Figure 2 and is based on maps presented by Labitzke and van Loon (1972). Again from 70°S to 90°S there is little change in stability. The latitude range from 70° to 90° is of the most importance. Figure 3 gives the latitude profile of absolute vorticity at 30 mb for July 1969 as calculated from the latitude profile of zonal wind given by Labitzke and van Loon (1972). While the vorticity on a pressure surface is not the same as the vorticity on an isentropic surface, the author believes
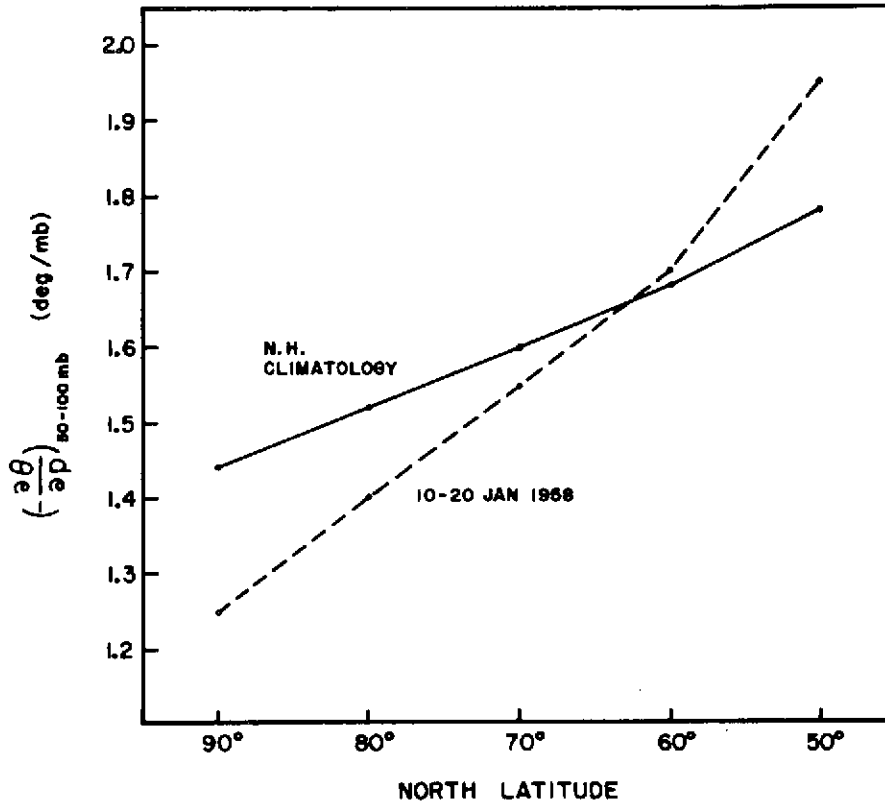
Fig. 28. Static stability in the layer 50-100 mb as a function of latitude in the Northern Hemisphere for January.
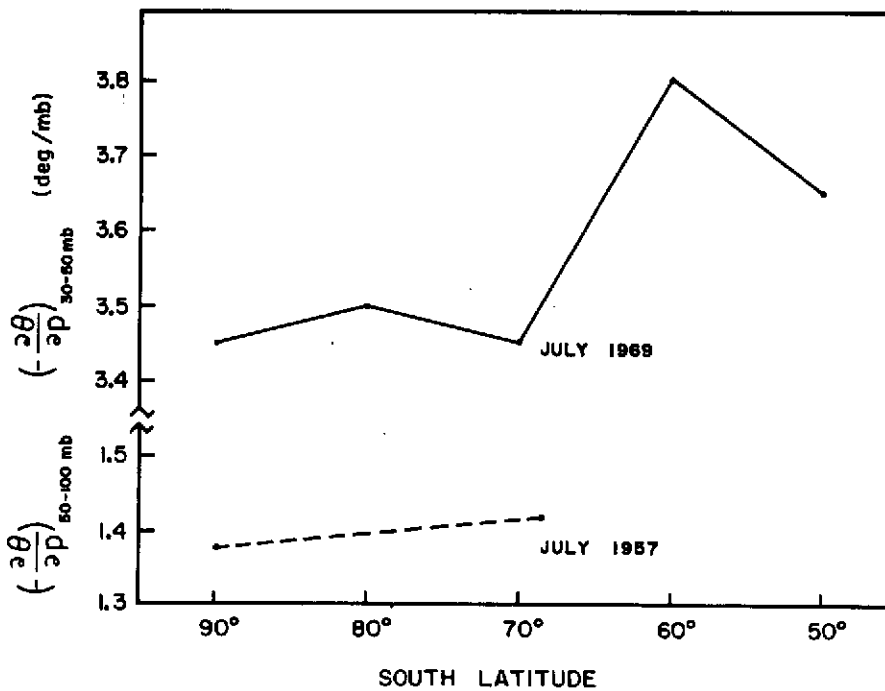
Fig. 29. Static stability in the layers 50-100 mb and 30-50 mb as a function of latitude in the Southern Hemisphere for July.
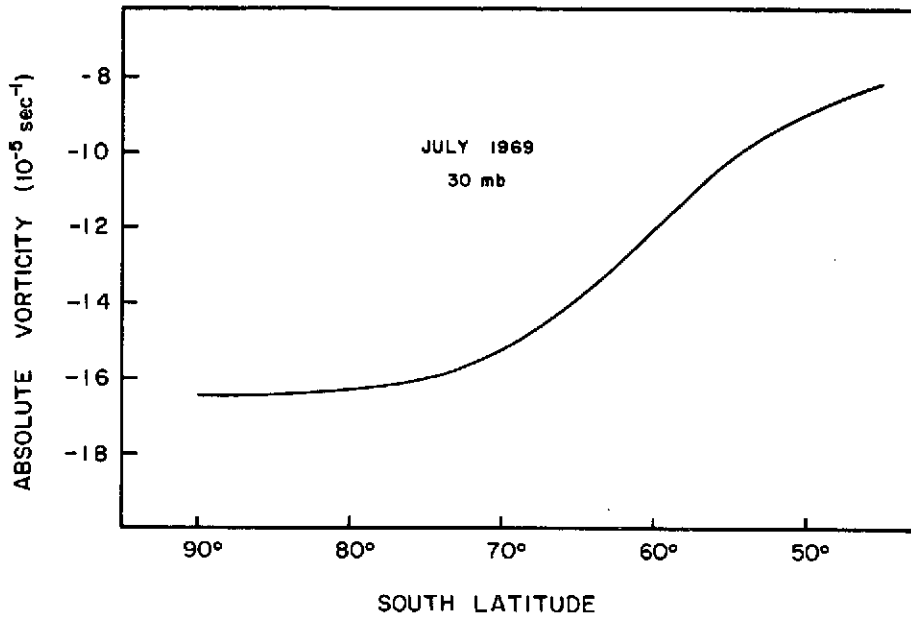
Fig. 30. Absolute vorticity as a function of latitude at 30 mb in Southern Hemisphere for July, 1969.
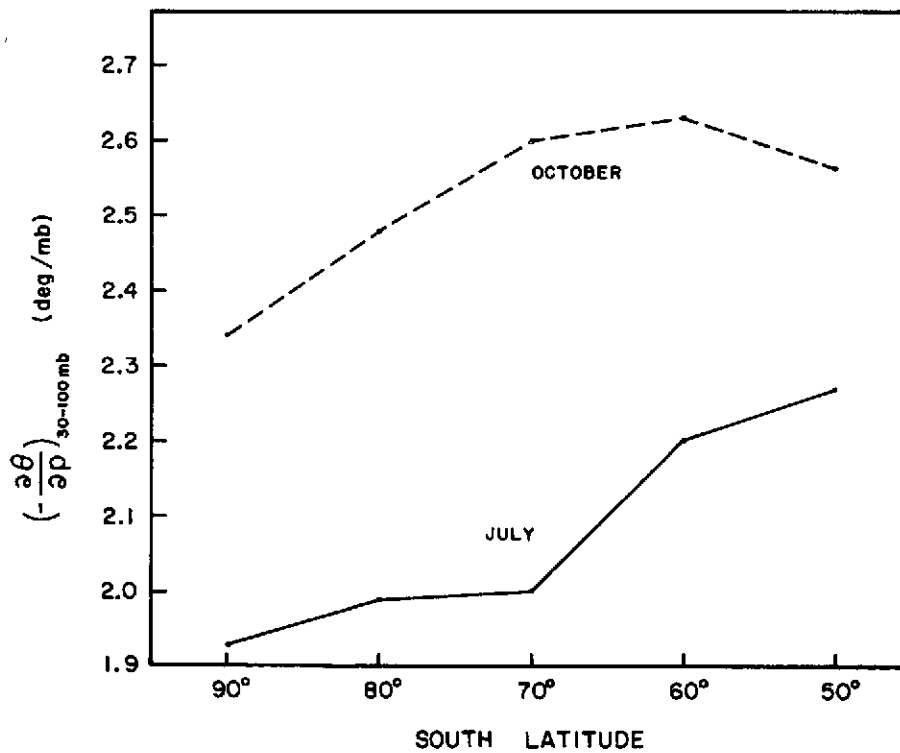
Fig. 31. Static stability in the layer 30-100 mb as a function of latitude in the Southern Hemisphere for July and October.

that the profile in Figure 30 is characteristic of conditions occurring on isentropic surfaces in the mid-stratosphere. All absolute vorticies in Figure 30 are negative. The absolute vorticity decreases (becomes larger negative) with latitude, with the maximum rate of decrease occurring at 60°S at the location of the jet axis. Poleward of about 70°S, the absolute vorticity profile flattens, becoming nearly constant with latitude. It is in this latitude band that a sharp decrease of static stability with increasing latitude will produce an extremum in potential vorticity which means that the criterion for vortex instability discussed previously is met. This appears to be the case in the northern hemisphere where a sharp decrease in static stability with latitude exists in high latitudes (see Figure 28). The southern hemisphere, however, exhibits a near constant-with-latitude profile of static stability from 70°S to 90°S (see Figure 29). Thus, while the instability criterion is met during mid-winter in the northern hemisphere (Mahlman, 1966; Charney and Stern, 1962), it is not to be met during mid-winter in the southern hemisphere.

Another indication of the difference in the early winter (before northern hemisphere breakdown) thermal structure of the Arctic and Antarctic vortices is given in a comparison of satellite-observed radiances over the two polar regions, discussed by Labitzke and van Loon (1972). Although the southern hemisphere pole is much colder in mid-winter at 30 mb, radiances in SIRS channel 8 (665 cm^{-1}) and in channel A of the Selective Chopper Radiometer indicate that the upper stratosphere over the Antarctic is warmer than over the Arctic. Therefore, the static stability would be larger over the south pole than over the north pole. At about 50° latitude the 30 mb temperature and the radiances

indicate that conditions are much alike in the two hemispheres. Thus, the latitude distribution of static stability $(-\frac{\partial\theta}{\partial p})$ is dissimilar in the two hemispheres.

In the southern hemisphere, in mid-winter, the latitude distribution of stability is such that the criterion for instability is apparently not met. This situation is in agreement with the lack of complete breakdowns in mid-winter in the Antarctic. In spring as the sun returns to high latitudes in the southern hemisphere, changes in the stratospheric lapse rate occur. The changes occur in such a way as to produce a latitude gradient of static stability. The heating due to the return of the sun and the presence of ozone results in increases in $(-\frac{\partial\theta}{\partial p})$, with greater increases occurring at lower latitudes because of the greater insolation. Figure 31 shows the changes in stability in the 30-100 mb layer which occur between July and October. For both months 30 mb temperatures for July 1969 from Labitzke and Van Loon (1972) have been used together with 100 mb climatological temperatures from Taljaard, et al. (1969). The static stability increases from July to October at all latitudes shown, but the important change is in the change in the slope of the profile between 70° and 90°S. There is now a sharp decrease in static stability with increasing latitude.

The change in slope from mid-winter to spring is also noted in Figure 32 which shows stabilities in the 50-100 mb layer from 1957 based on monthly mean data from Amendsen-Scott, Cape Hallett and Wilkes stations. The data for Cape Hallett and Wilkes is again averaged and plotted at latitude 69°S. The change in static stability with latitude is a minimum in July. From July and August to September and October, there is a sharp increase in the static stability at both latitudes and
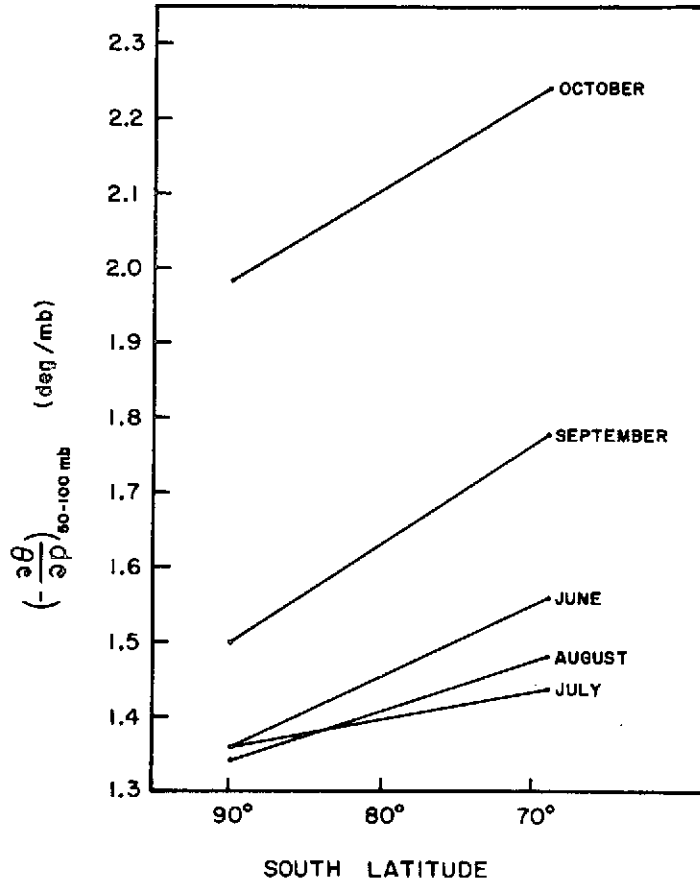
Fig. 32. Variation of static stability slope with latitude in the
layer 50-100 mb in the Southern Hemisphere from June to October.
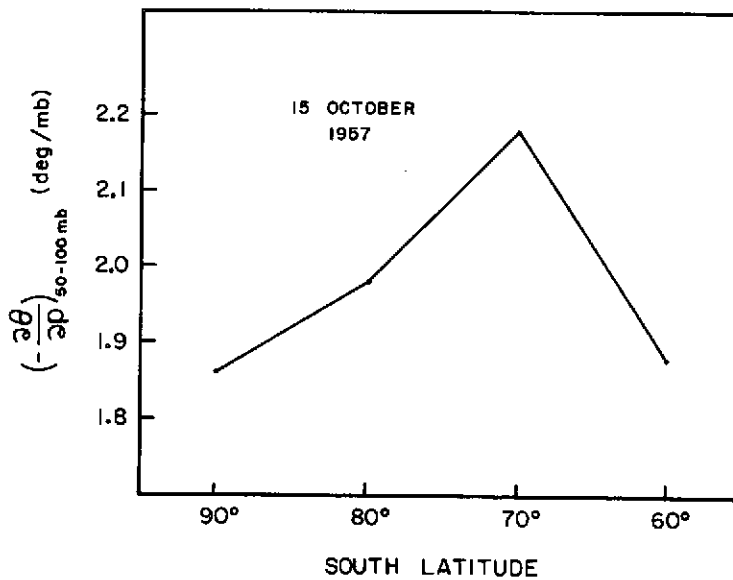
Fig. 33. Static stability in the layer 50-100 mb as a function of
latitude in the Southern Hemisphere on 15 October 1957.

a sharp increase in the slope of the profile. The increased slope in Figures 31 and 32 tends to produce a potential vorticity profile which meets the derived instability criterion. Thus, although in mid-winter the flatness of the static stability profile in high latitudes prevents the instability criterion from being met, in spring the stability profile develops a sharp slope with latitude so that the instability criterion is met. This characteristic is also evident in Figure 33 which is produced from a cross-section across the south pole, presented by Palmer and Taylor (1960), for conditions just prior to a vernal breakdown. The sharp slope with latitude from 70°S to 90°S is again obvious and equal approximately in magnitude to the slope given by Mahlman (1966) for a northern hemisphere, mid-winter breakdown.

2.33 Possible relation of the latitude distribution of static stability and mean meridional motions in the stratosphere

A number of authors, such as Reed, Wolfe and Nishimoto (1963), Teweles (1964), and Mahlman (1966), have discussed the zonally average vertical motions in the stratosphere during the northern hemisphere winter. The consensus is that the northern hemisphere has a two-celled mean meridional circulation in the stratosphere with upward motion over the pole and equator and downward motion in mid-latitudes. The distribution of vertical velocity over the north polar region produces a vertical stretching and a tendency toward lower stability in that region. Thus, the mean meridional circulation in the northern hemisphere stratosphere may be related to the decrease of static stability with latitude in the polar region.

The mean meridional circulation in the stratosphere of the southern hemisphere is not well defined. There are indications, however, that there is a general descending motion over the south pole. Rubin and Weyant (1963) indicate a downward motion between 950 and 75 mb with a maximum at about 500 mb for the winter months and for the entire year. This descent over the pole in the low stratosphere helps account for the observed Antarctic ozone observations and implies a one-celled structure with ascent over the equator (Reiter, 1969, Reiter, 1971). This descent over the south polar region during the winter could possibly be the reason for the lack of a sharp decrease of static stability with latitude in the southern hemisphere.

The possible difference between the hemispheres in the stratospheric mean meridional motions is probably related to the difference between the hemispheres in the importance of eddy motions. The mean vertical motion distribution in the northern hemisphere with upward motion in the polar regions is closely linked to the eddy motions. Mahlman (1966) has shown that if the vertical motion field is evaluated in relation to a corrdinate system tied to the polar-night jet axis rather than a coordinate system tied to latitude, the vertical motion field shows descent poleward of the jet axis and ascent equatorward of the jet axis. Thus, the arrangement of the northern hemisphere eddies in the stratosphere is producing the observed, zonally-averaged vertical motion field.

In conclusion we may state that the Arctic and Antarctic mid-winter, stratospheric vortices differ in their latitudinal distributions of static stability. This difference results in the northern hemisphere vortex meeting the criterion for vortex instability, while the southern hemisphere

vortex in mid-winter does not. The difference in distribution of static stability may be related to differences in the zonally-averaged vertical motion patterns in the stratospheres of the two hemispheres.

3.0 Conclusions

Potential and kinetic energies in their mean zonal and eddy modes, as well as vorticity are parameters which describe atmospheric behavior and variability over relatively large space and time scales. These parameters, therefore, are especially suited to study interhemispheric differences in the general circulation of the atmosphere. They also lend themselves to a description of the interannual variability of the atmosphere which constitutes an important aspect of the earth's climate.

In the preceding sections it has been amply demonstrated that these parameters can be obtained to a certain degree of reliability from radiance data collected by satellites. We are therefore in a position to make interhemispheric comparisons without the bias of different data densities that exists with the use of radiosonde data.

At this time we are still faced with a systematic underestimation of potential and kinetic energies, especially in tropospheric layers. The eddy modes of these energies, in general, appear to suffer more from such underestimates than the zonally averaged modes. Part of this short- coming can be ascribed to insufficient data resolution in space and time by which satellite measurements are plagued at the present, and which necessitate the application of smoothing and interpolation techniques not normally used on synoptic radiosonde data. We consider this, however, a shortcoming that could easily be eliminated by having more than just one polar orbiting satellite available at any given time.

The good agreement achieved between SIRS and NMC data subjected to spectrum analyses in the hemispheric wave number domain offers the encouraging outlook that major atmospheric motion systems on the planetary and cyclone scales could easily be monitored with respect to their

temperature and wind structure by satellite sensing techniques. This outlook is particularly encouraging in view of the reduction in the number of weather ships in the Atlantic and Pacific, dictated, at least in part, by fiscal considerations.

Stratospheric layers can be monitored by satellites even more easily than tropospheric layers. The latitudinal distribution of static stability and vorticity apparently influences the dynamic stability and the tendency towards major breakdowns of the stratospheric polar-night vortex. Stability and vorticity characteristics differ strongly during the winter seasons in the northern and southern hemispheres. Since both, static stability and vorticity are parameters that can be derived -- at least in their large-scale distributions -- from satellite radiance data, one should eventually be able to anticipate polar vortex breakdowns from real-time satellite data analyses.

4.0 REFERENCES

Charney, J. G., and M. E. Stern, 1962: On the Stability of Internal Baroclinic jets in a Rotating Atmosphere. Journal of the Atmospheric Sciences, 19, 159-172.

Chen, T. S., 1973: On the Large-Scale Horizontal Exchange Coefficients. Arch. Meterol. Geophys. Bioklimatol. (To be published)

Craig, R. A., 1965: The Upper Atmosphere: Meteorology and Physics. Academic Press, New York.

Labitzke, K. and H. Van Loon, 1972: The Stratosphere in the Southern Hemisphere. Meteorology of the Southern Hemisphere, Meteorological Monographs, 13, Number 35, 113-138.

Leith, C. E., 1968: Two-Dimensional Eddy Viscosity Coefficients, Proc. Symp. Numerical Weather Prediction, Tokyo, p. 41-44.

Mahlman, J. D., 1966: Atmospheric General Circulation and Transport of Radioactive Debris. Atmospheric Science Paper No. 103, Department of Atmospheric Science, Colorado State University.

Oort, A. H., and E. M. Rasmusson, 1971: Atmospheric Circulation Statistics, NOAA Professional Paper 5.

Palmer, C. E. and R. C. Taylor, 1960: The Vernal Breakdown of the Stratospheric Cyclone over the South Pole. Journal of Geophysical Research, 65, 3319-3329.

Pedlosky, J., 1964: The Stability of Currents in the Atmosphere and the Ocean, Part I. Journal of the Atmospheric Sciences, 21, 201-219.

Reed, R., J. Wolfe, and H. Nishimoto, 1963: A Spectral Analysis of the Energetics of the Stratospheric Warming of Early 1957. Journal of the Atmospheric Sciences, 20, 256-275.

Reiter, E. R., 1969: Atmospheric Transport Processes, Part I: Energy Transfers and Transformations, USAEC Report TID-249868.

_____, 1971: Atmospheric Transport Processes. Part 2: Chemical Tracers. USAEC Report TID-25314.

Rubin, M. J., and W. Weyant, 1963: The Mass and Heat Budget of the Antartic Atmosphere. Monthly Weather Review, 91, 487-493.

Taylor, R. C., 1961: Upper-Air Temperatures at U.S. Antartic Stations - 1956 - 1957. IGY General Report No. 19.

APPENDIX I

A Contribution to the Synoptic Climatology
of the Extratropics

A CONTRIBUTION TO THE SYNOPTIC CLIMATOLOGY

OF THE EXTRATROPICS

by

Srinivasan Srivatsangam

Department of Atmospheric Science

Colorado State University

Fort Collins, Colorado

August, 1973

Atmospheric Science Paper No. 203

Abstract

A relationship is established between relative geostrophic
vorticity on an isobaric surface and the Laplacian of the underlying
layer-mean temperature. This relationship is used to investigate the
distribution of vorticity and baroclinicity in a jet-stream model which
is constantly recurrent in the winter troposphere. The investigation
shows that the baroclinic and vorticity fields of the extratropical
troposphere must be bifurcated with two extrema in the middle and
subpolar latitudes. This pattern is present in daily tropospheric
meridional cross-sections. The reasons for the disappearance of bifurcation
in the time-and-longitude averaged distributions are discussed.

The time-averaged zonal root mean square vorticity, called K for
brevity, is shown to be a parameter which overcomes this deficiency in
the presentation of meridional cross-sections of the atmosphere.

The meridional cross-sections of K indeed indicate that the upper
tropospheric vorticity--and by inference the tropospheric-mean baro-
clinicity--distribution is bifurcated in winter with one maximum over
30 - 45 N, another over 60 - 70 N and a relative minimum at 55 N.

The geographical distribution of the temporal r.m.s. vorticity shows
that the maximum of K over 30 - 45 N in the meridional cross-section
is due to three waves in the vorticity field at these latitudes. Two
of the three maxima imbedded in these waves occur over the
eastern coastlines of Asia and North America, and are considerably more
intense than the maximum occurring over Southern Asia. All three
maxima are quasi-zonally distributed. The maxima over the oceans
have their major axes in the vicinity of cold and warm ocean current
confluences. These maxima, moreover, do not protrude far into the continents.

i

The implications of the above geographical distribution for the maintenance of the observed kinetic energy and baroclinicity distributions in the extratropical troposphere in winter are discussed.

Lastly, it is shown that the subtropical and subpolar ridges are nearly antiparallely distributed as is required by the observed distribution of temporal r.m.s. vorticity at the jet-stream level.

A Note on Nomenclature

We shall denote by the term Extratropical Frontal Jet Streams (EFJ)
all jet streams which occur in the upper troposphere in conjunction with
lower tropospheric baroclinic zones or fronts. The subpolar (60-70 N)
branch of this jet stream will be called the Arctic Front Jet Stream (AFJ)
(see Reiter, 1963, p. 221-224; Petterssen, 1956, p. 208). The midlatitude
(35 - 50 N) branch of the same will be called the Polar Front Jet Stream
(PFJ).

We shall use the term "mean" to denote arithmetic mean only.
Wherever root mean square values are alluded to, the adjective "r.m.s."
will be used. The term "averaging" will be used to refer to both
arithmetic averaging and the process of obtaining r.m.s. values.

Relative geostrophic vorticity will be generally referred to as
vorticity.

TABLE OF CONTENTS

LIST OF TABLES

v

LIST OF FIGURES

1. Introduction

One apparent contradiction in meteorology is made obvious by a consideration of the winter mean meridional distribution of $[\bar{u}]$, i.e., the time-and-longitude averaged zonal wind component, and the mean meridional circulation in the same season (see, for example, Oort and Rasmusson, 1971, p. 23, 24 and 234). The $[\bar{u}]$ field has a maximum at about 30 N, 200 mb and decreases in all directions from that point. This represents, under the assumption of geostrophic flow, a maximum horizontal concentration of isotherms in the troposphere at 30 N and the presence of a hemispheric Hadley cell with warm air rising in the equatorial regions and cold air sinking in the polar regions, with a generation of kinetic energy in the region occupied by this cell, for otherwise friction will destroy the $[\bar{u}]$ field. But the mean meridional circulation shows an indirect cell in the middle latitudes which destroys zonal kinetic energy in the region occupied by that cell. These two illustrations are reconciled by partitioning the daily K.E. and available potential energy (A) fields into zonal-mean and eddy components. A study of these indicates the energy cycle of the atmosphere to be as in Fig. 1, which could be used to reconcile the mean meridional circulation and the field of $[\bar{u}]$ (see, for example, Lorenz, 1967, p. 97 - 113). Although our understanding of the atmospheric energy cycle is thereby enhanced, the meridional distributions remain poor representatives of the extratropical eddy field. However, the eddies are of considerable importance. Therefore we feel that there is a need for the proper meridional representation of extratropical eddies in time-mean cross-sections.

Table 1

Definitions of Symbols

A	Available potential energy
$\mathbb{B}$	The baroclinicity vector
$f(x,..), f(x,y,..)$ etc,	Mathematical functions; not the Coriolis parameter
f	$2\,\Omega \sin\phi$, the Coriolis parameter
H	Geopotential hgt
$K = [\{\zeta_g\}_{(\lambda)}]_{(t)} = [\{\zeta_g{(t)}\}]_{(\lambda)}$,	The time mean of the zonal root mean square vorticity
K.E.	Kinetic Energy
R	The gas constant for dry air
p	Pressure
t	Time
T	Temperature
u_g, v_g	Zonal and meridional components, respectively, of the geostrophic wind
β	$\partial f/\partial y$, the Rossby parameter
ζ_g	Relative geostrophic vorticity
λ	Longitude
ϕ	Latitude
$[f]_{(x)}$	The arithmetic mean of $f(x,...)$ in x
$[[f]_{(x)}]_{(y)} = [f]_{(x,y)}$	
$(f)_{(x)} = f(x,...) - [f]_{(x)}$	
$\{f\}_{(x)}$	Root mean square value of $f(x,...)$ in x
$([H]_{(\lambda)})_{(\phi)} = [H]_{(\lambda)} - [H]_{(\lambda,\phi)}$	The deviation of zonally averaged geopotential height of an isobaric surface from the hemispheric average in the present case

α — Symbol for proportionality

$|x|$ — Modulus of x

$<f(x,y)>$ — Matrix of f in x and y

$-$ — Layer-mean

$$\nabla_2^2 = (\frac{\partial^2}{\partial x^2} + \frac{\partial^2}{\partial y^2})$$ — The horizontal Laplacian operator

In the symbol $[\bar{u}]$ — $^{-}$ is time average and [ ] is zonal average

Most of the existing parameters are poor representatives of the eddies (in time-and-zonal average distributions). One exception is perhaps the generation of kinetic energy. This parameter has been described well by Kung (1971), but there are many difficulties in estimating this parameter, especially over the data-sparse regions of the atmosphere.

Since, in general, vorticity is estimated more accurately than divergence on account of the magnitudes involved, we shall use geostrophic relative vorticity here to represent the eddies in time-and-zonal mean cross-sections.

We shall start by establishing a relationship between geostrophic relative vorticity over an isobaric surface and the Laplacian of the layer-mean temperature $\overline{T}$ of the underlying atmospheric layer. This relationship will enable a study of the association between vorticity and baroclinicity distributions in synoptic-scale extratropical eddies purely in terms of layer-mean temperatures.

2. A Relationship between the Thermal and Vorticity Fields

The zonal component of the geostrophic wind at pressure p_o might be written as

$$u_{g,p_o} = u_{g,oo} - \frac{\partial u_g}{\partial p} \, |\delta p| \qquad (1)$$

where $u_{g,oo}$ is the zonal component of the geostrophic wind at some higher pressure $p_o + \delta p$. Substituting the geostrophic thermal wind in the x, y, p coordinate system, viz.,

$$\frac{\partial u_g}{\partial p} = \frac{R}{\overline{p}f} \frac{\partial \overline{T}}{\partial y} \qquad (2)$$

(where the bar represents mean conditions in the layer p_o to $(p_o + \delta p)$ in equation (1) and differentiating with respect to y

$$\frac{-\partial u_{g,p_o}}{\partial y} = \frac{-\partial u_{g,oo}}{\partial y} + \frac{R}{\overline{p}f} \frac{\partial^2 \overline{T}}{\partial y^2} \, |\delta p| - \frac{R}{\overline{p}} \frac{\partial \overline{T}}{\partial y} \frac{\beta}{f^2} \, |\delta p| \qquad (3)$$

The assumption that $\frac{\partial u_{g,oo}}{\partial y} \simeq 0$ is generally valid if $p_o < 500$ mb and $(p_o + \delta p) > 900$ mb.

If $\left(-\frac{\partial \overline{T}}{\partial y}\right)$ has a value of 0.16×10^{-6} ^{o}K cm^{-1} in the baroclinic region and a value of 0.04×10^{-6} ^{o}K cm^{-1} in the relatively barotropic air masses (see Fig. 3) ,

$$\frac{\partial^2 \overline{T}}{\partial y^2} \simeq -0.12 \times 10^{-14} \, ^{o}\text{K cm}^{-2}$$

if the changes in temperature gradients are obtained over 10 deg. latitude. These values are representative of middle latitude frontal systems. So, if the latitude is 45 deg. such that $f = 1.0 \times 10^{-4}$ s^{-1} and $\beta = 1.6 \times 10^{-13}$ cm^{-1} s^{-1}

$$\frac{-\dfrac{R}{\bar{p}} \dfrac{\partial \overline{T}}{\partial y} \dfrac{\beta}{f^2} |\delta p|}{\dfrac{R}{f\bar{p}} \dfrac{\partial^2 \overline{T}}{\partial y^2} |\delta p|} = \frac{0.16 \times 10^{-15}}{0.12 \times 10^{-14}}$$

$$\approx 1 \times 10^{-1}$$

Hence the third term on the right hand side of equation (3) can be neglected in comparison with the second term. Thus

$$- \frac{\partial u_{g,p_o}}{\partial y} = \frac{R}{\bar{p}f} \frac{\partial^2 \overline{T}}{\partial y^2} |\delta p| \tag{4}$$

A similar equation is readily derived for $\dfrac{\partial v_g}{\partial x}$. The addition of the two equations then shows that

$$\zeta_{g,p_o} = \frac{R}{\bar{p}f} \left(\frac{\partial^2 \overline{T}}{\partial x^2} + \frac{\partial^2 \overline{T}}{\partial y^2} \right) |\delta p| \tag{5}$$

or,

$$\zeta_g \propto \nabla_2^2 \overline{T} \tag{6}$$

This is the relationship that we sought.

3. Application to a Jet-Stream Model

We shall use this in the model of jet-stream flow illustrated in Figure 2, which was inspired by a model presented earlier by Reiter (1972, p. 69). Here the surface wind has been assumed to be zero everywhere and hence the streamlines at the jet-stream level are parallel to the tropospheric mean isotherms. In Fig. 3, the meridional temperature gradient associated with the model of Fig. 2 is presented and in Fig. 4 the corresponding distribution of $\nabla_2^2 \bar{T}$. (N.B.: Here and hereafter we shall refer to the layer-mean temperatures as temperatures).

From these illustrations it is seen that the vorticity maximum is located slightly poleward of the region of maximum baroclinicity and the vorticity minimum equatorward of the region of maximum baroclinicity in that meridional sector. We use the term baroclinicity here to refer to $\partial \bar{T} / \partial y$. However, an analysis of the field of the magnitude of the baroclinicity vector, i.e.,

$$\left| \mathbf{B} \right| = \left[\left(\frac{\partial \bar{T}}{\partial x} \right)^2 + \left(\frac{\partial \bar{T}}{\partial y} \right)^2 \right]^{\frac{1}{2}}$$

shows that the distribution of this quantity is not very different from that of $\partial \bar{T} / \partial y$ except over the 50 - 70 longitude sector.

In Fig. 5 and 6 the zonal averages of $\left| \mathbf{B} \right|$, $\frac{\partial \bar{T}}{\partial y}$, $\nabla_2^2 \bar{T}$ and the zonal root mean square (r.m.s.) values of $\nabla_2^2 \bar{T}$ are presented. From these averages it is seen that if the model of Fig. 2 is indeed representative of extratropical eddy flow, the zonal averages of the various parameters considered here must be bifurcated with extrema in middle and subpolar latitudes.

Figure 7 is the geopotential height field of the 300 mb surface for Jan. 1, 1970. It is typical of the 300 mb height field on almost any day

in January 1970. From this illustration it is obvious that the model
of Fig. 2 indeed occurs in daily maps.

At this point we shall digress from this discussion and elucidate
our averaging conventions.

4. Averaging Conventions*

Here we shall follow the averaging conventions introduced by Reiter (1969a; 1969b, p. 6 - 8). The symbolism is defined in Table 1. A new extension of these conventions is introduced here. This is for the process of obtaining the r.m.s. value of a function f(x) with respect to x. The r.m.s. value in this case will be represented by $\{f\}_{(x)}$.

Note would be made here of an important difference between double arithmetic means and mixed r.m.s. - arithmetic means. Whereas

$$[f]_{(x,y)} = [[f]_{(x)}]_{(y)} = [[f]_{(y)}]_{(x)} = [f]_{(y,x)} \quad (7)$$

where $f = f(x, y, \ldots)$

$$[\{f\}_{(x)}]_{(y)} \neq [\{f\}_{(y)}]_{(x)} \quad (8)$$

unless $<|f(x,y)|>$ is a square symmetric matrix (or of some other simpler but square form, which will not be discussed here), or, if non-square, if and only if all the matrix elements are of equal magnitude. Here it is implied by writing $f(x, y, \ldots) = f(x, y)$ that all other variables are held constant.

The values of $[\{\zeta_g\}_{(t)}]_{(\lambda)}$ and $[\{\zeta_g\}_{(\lambda)}]_{(t)}$ for Jan. 1970 are given in Table 2. It is seen that the two are quite comparable. Simple hand calculations show that the matrices $<|\zeta_g(\lambda, t)|>$ would yield the kind of values presented in Table 2 if the values of $|\zeta_g(\lambda, t)|$ are nearly equal or if standing eddies dominate the matrix. It will be seen below that the middle latitude vorticity field is dominated by (standing) wave number three. In the subtropics, fairly homogeneous values of $\zeta_g(\lambda, t)$ might be expected by climatological considerations. The reasons for the similarity

*NB: In this page f is not the Coriolis parameter.

Table 2

$$[\{\zeta_g\}_{(\lambda)}]_{(t)} \text{ and } [\{\zeta_g\}_{(t)}]_{(\lambda)} \text{ for Jan. 1970.}$$

Units: 10^{-7} s^{-1}

(For an explanation of symbols see Table 1)

$$[\{\zeta_g\}_{(\lambda)}]_{(t)}$$

Pressure	25 N	30 N	35 N	40 N	45 N	50 N	55 N	60 N	65 N	70 N	75 N
700 mb	185	179	198	223	243	245	235	249	237	236	254
500 mb	249	256	297	348	347	324	316	353	360	347	361
400 mb	295	330	367	437	414	383	370	413	412	394	398
300 mb	354	400	455	508	483	419	392	427	422	405	399
200 mb	373	419	508	490	412	318	286	302	293	284	268
100 mb	256	228	244	252	234	208	180	181	184	178	170

$$[\{\zeta_g\}_{(t)}]_{(\lambda)}$$

Pressure	25 N	30 N	35 N	40 N	45 N	50 N	55 N	60 N	65 N	70 N	75 N
700 mb	181	175	189	215	228	235	232	246	227	228	254
500 mb	246	255	291	334	335	320	318	349	345	336	357
400 mb	292	329	360	421	401	382	374	410	398	383	394
300 mb	350	399	450	495	468	420	394	423	408	392	390
200 mb	370	418	495	473	399	319	287	292	274	268	263
100 mb	249	226	236	238	216	193	172	173	171	167	167

of $[\{\zeta_g\}(t)]_{(\lambda)}$ and $[\{\zeta_g\}(\lambda)]_{(t)}$ at subpolar latitudes are not known at this time although characteristic periodicities of the eddies here might be suspected as causing the similarity.

The important conclusion from the above discussion is that the inequality (8) might be considered to be invalid for geostrophic relative vorticity in the extratropical winter troposphere. Hence

$$[\{\zeta_g\}(t)]_{(\lambda)} \; \simeq \; [\{\zeta_g\}(\lambda)]_{(t)} \; = \; K \tag{9}$$

5. The Distribution of Vorticity in Winter

Here we shall resume the discussion of Section 3.

Figure 8 illustrates $[\zeta_g]_{(\lambda, t)}$ which slightly indicates the tendency for the bifurcation of jet-stream level vorticity that we anticipated. We also note that 1) the subpolar zonal-and-time mean vorticity is not anticyclonic but cyclonic and 2) the arithmetic mean value of vorticity in the extratropics is generally much smaller (one-half or less) than the values of K in Table 2.

The reasons for observation 2) above are that although the vorticity associated with extratropical eddies is high, a fraction of it is transient, and this fraction is large in the subpolar latitudes as we shall see below. Time averaging eliminates this component. And when zonal averaging is performed additionally the standing eddies with their large magnitudes of vorticity are also eliminated. The remainder, which is the vorticity of the prevailing zonal mass (or geopotential height) distribution, is indeed very small.

The reasons for observation 1) are that the Arctic Front Jet (AFJ) tends to occur in conjunction with both ridges and troughs and therefore the relative geostrophic vorticity in the subpolar upper troposphere tends to fluctuate between large positive and negative values. The values of $[\zeta_g]_{(\lambda, t)}$ are the small differences between these large positive and negative values.

Figure 9 illustrates the distribution of the parameter K . As mentioned earlier the magnitude of K is everywhere much larger than that of $[\zeta_g]_{(\lambda, t)}$. Whereas $[\zeta_g]_{(\lambda, t)}$ distribution represents the vorticity of the prevailing latitudinal mass distribution only, K tends to conserve the components of vorticity associated with transient

and standing eddies, since the r.m.s. "averaging" neglects the differences
in signs. In the neighborhood of the confluence of the Subtropical Jet
Stream (STJ) and the Polar Front Jet Stream the ratio $[\zeta_g]_{(t,\lambda)}$:K
reaches a maximum indicating the large zonal components of the winds in the
STJ maxima and the relative large zonal wind shears north of these maxima
(see Krishnamurti, 1961). The effect of these shears would appear in the
$[\zeta_g]_{(t,\lambda)}$ distribution only if the waves in the STJ are of small amplitude.
From the illustrations presented by Krishnamurti (op. cit.) and the distri-
butions of $[\bar{u}]$ mentioned above this is seen to be true.

That the vorticity distribution represented by $[\zeta_g]_{(t,\lambda)}$ is the one
associated with the mean mass distribution is apparent from Fig. 10, which
is the January 1970 distribution of

$$([H]_{(t,\lambda)})_{(H)} = [H]_{(t,\lambda)} - [H]_{(t,\lambda,\phi)}$$

i.e., the deviation of zonal-mean geopotential height of isobaric sur-
faces from their hemispheric averages. By hemispheric mean we denote the
average of $[H]_{(t,\lambda)}$ over the latitudes 20 N to 80 N. It is readily seen
from this diagram that the windspeeds and shears associated with the
mean mass distribution must result in the vorticity field of Fig. 8.

The components of vorticity associated with standing and transient
eddies are very large away from the 200 mb, 35-42 N region, as seen in Fig.
9.

It might be considered that the 'normal' state of the extratropical
troposphere is a disturbed state. Then the distribution of K might be said
to represent the 'normal' state of the extratropical troposphere in winter
for it conserves and presents the eddy effects (in addition to the influences
of the time-and-longitude averaged mass field) unlike the $[\zeta_g]_{(t,\lambda)}$
distribution.

6. Vorticity Distribution and Tropopause Structure

A very distinguishing feature of the distribution of K is that the isopleths are quasi-horizontal whereas the isopleths of $[\zeta_g]_{(t,\lambda)}$ are nearly vertical everywhere. Moreover the vertical gradients of K are much larger above about 200-300 mb. Thus it is immediately apparent that a 'normal' distribution of this meteorological parameter, viz., vorticity, is capable of indicating a "lid" over tropospheric circulation features. The reason for this is that jet streams are wind systems associated with tropopause-breaks (see, for example, Reiter 1969C, p. 91-94.) The baroclinicity reversals associated with these breaks produce sharp reductions in vorticity above the jet-stream level (See proportionality 6 above.) The longterm zonal circulation vorticity, since it does not include all the meanders and temporal fluctuations of the jet streams, does not indicate these important reductions whereas the parameter K does.

We see from Fig. 9 that the Arctic Front Jet will normally occur at higher pressures than the Polar Front Jet and that the stratosphere is situated at higher levels in the tropics and midlatitudes than in the sub-polar regions.

7. The Geographical Distributions

In Fig. 11 the geographical distribution of $[\zeta_g]_{(t)}$ is given. Here the $0, \pm 100 \times 10^{-7}$ s $^{-1}$ contours have been omitted for clarity. Since the standing eddy component of vorticity has not been eliminated here as it is in the $[\zeta_g]_{(t,\lambda)}$ distribution the magnitudes of vorticity in the extratropics are higher.

Fig. 12 gives the geographical distribution of $\{\zeta_g\}_{(t)}$. This diagram is discussed below.

Middle Latitudes

A comparison of Fig. 11 and 12 shows that the midlatitude distribution of January mean vorticity has essentially a three-wave pattern, with maxima over the Atlantic and Pacific Oceans and over southern Asia. The magnitudes of $\{\zeta_g\}_{(t)}$ are larger than those of $[\zeta_g]_{(t)}$ everywhere. But the differences between $\{\zeta_g\}_{(t)}$ and $[\zeta_g]_{(t)}$ are not very large at the centers of the vorticity maxima. This shows that the three waves in the middle latitudes have a very large standing component.

All the three maxima are quasi-zonally distributed. The location of the maxima of $[\zeta]_{(t)}$ over the oceans is of particular significance. Both of these maxima have their major axes immediately over oceanic cold and warm current confluences (see, for example, Sverdrup, Johnson and Fleming, 1942, Charts II, IV and VII). The central contours of these maxima are located almost exactly over the east coasts of Asia and North America. The maxima do not protrude far into the continents.

Subpolar Latitudes

Here the values of $[\zeta_g]_{(t)}$ and $\{\zeta_g\}_{(t)}$ differ considerably in the regions of occurrence of vorticity extrema thus indicating the larger transient component of vorticity in these latitudes, compared to midlatitudes.

Perhaps the most interesting feature of these illustrations meteorologically is that the baroclinic field of the extratropical troposphere is divided into two extrema. The vorticity field associated with the midlatitude maxima are located over regions of maximum ocean surface temperature contrast. The vorticity maxima are also located over regions (especially off the East Coast of the USA) where the prevailing winds have significant southerly components. Thus if the vorticity advection theory of development (Reiter 1963, p. 326-332) is applied in these regions, an extremely large amount of kinetic energy would be seen generated by the nascent extratropical cyclones over the regions of ocean current confluence. This generation must overcompensate frictional dissipation and appear in the subpolar latitudes as the Arctic Front Jet. Although the above statements are purely qualitative the author feels that the midlatitude distribution of vorticity maxima significantly influences the region of occurrence of the AFJ. It is possible that the vorticity patterns associated with the AFJ similarly affect the kinetic energy distribution in the middle latitudes but much more intermittently since the AFJ indeed is more transient than the PFJ as might be seen from daily geopotential height fields of the 300 mb surface. The greater part of the kinetic energy of the PFJ is probably derived from interaction with the STJ. These regions have been established by Krishnamurti (1961) to be the regions where the vorticity maxima occur in midlatitudes.

Krishnamurti (1961) showed that in the meridional sectors where the subtropical highs protrude poleward, the troughs associated with the PFJ plunge equatorward. This is also brought out in Fig. 11. But there seems to be very little interaction of this type over southern Asia. This is also true of another analysis performed by the author. Fig. 13 gives the zonal distribution of $\{\zeta_g\}_{(t)}$ at 300 mb, 60 N and of $[\zeta_g]_{(t)}$ at 200 mb, 25 N. From this diagram it is seen that the most barotropic (i.e., smallest values of $\{\zeta_g\}_{(t)}$ regions in the subpolar latitudes are located in the meridional sectors where the subtropical highs protrude farthest poleward; these are also the sectors where the vorticity is a maximum in the midlatitudes.

In view of the observed barotropy in the subpolar latitudes in these meridional sectors, the baroclinic regions in the subpolar latitudes must be in the meridional sectors between those in which the midlatitude distribution of baroclinicity has maxima. This is seen to be the case from Fig. 12. The exception to this rule again occurs over Asia where the midlatitude and subpolar maxima of $\{\zeta_g\}_{(t)}$ occur in the same meridional sector.

8. <u>Some Anomalies of the Circulation of January 1970</u>

An excellent analysis of the circulation of Jan. 1970 has been presented

by Wagner (1970). He notes a number of anomalies of the January 1970

circulation. We consider two of these as of particular significance.

Wagner (op. cit.) notes that "the broad cyclonic flow over the oceans at

midlatitudes was associated with anomaly centers of 100 and 170 m below

normal over the Pacific and Atlantic respectively" at the 700 mb level.

The anomalies at the 300 mb level were not given. But if conditions similar

to those at the 700 mb level were prevalent there, we should expect that the

vorticity extrema over the two oceans are normally less well developed than

indicated by Fig. 8 and 9.

Wagner (op. cit.) also presents the departures from normal of average

surface temperature for January 1970 for the U. S. These are mostly positive west of

105 W and negative east of that longitude. If these could be thought of as

being brought about by upper tropospheric troughs, then, normally the vorticity

maxima over the oceans must protrude more into the continents than indicated

by Fig. 8 and 9.

9. Conclusions

From our results we conclude that the upper tropospheric vorticity field and the tropospheric-mean baroclinic field of the extratropical troposphere are bifurcated in winter. The extrema of vorticity occur over 30-45 N and 60-70 N with a relative minimum at 55 N.

A parameter such as time-averaged zonal root mean square vorticity is capable of bringing out this feature in time-and-zonal average distributions

If these distributions have pressure as vertical coordinate, the existence of a stratosphere which appears as a lid over tropospheric circulation features could be obtained.

These distributions indicate clearly the normal location of the frontal jet-streams of the extratropical troposphere which are otherwise lost in averaging.

Acknowledgements

Bibliography

Krishnamurti, T. N., 1961. The subtropical jet stream of winter, J.
    Meteorol., 18:172-191.

Kung, Ernest C., 1971. A diagnosis of adiabatic production and destruction
    of kinetic energy by the meridional and zonal motions of the atmosphere,
    Quart. J. Royal Met. Soc., 97:61-74.

Lorenz, Edward N., 1967. The nature and theory of the general circulation
    of the atmosphere, World Meteorological Organization, No. 218. TP. 115,
    161 pp.

Oort, Abraham H., 1964. On estimates of the atmospheric energy cycle,
    Mon. Weather Rev., 92:483-493.

Oort, Abraham H., and Rasmusson, Eugene M., 1971. Atmospheric circulation
    statistics, NOAA Professional Paper 5, (U.S. Govt. Printing Office,
    Washington, D.C. Stock Number 0317-0045) 323 pp.

Petterssen, Sverre, 1956. Weather analysis and forecasting, Vol. 1. McGraw
    Hill Book Co. Inc., 428 pp.

Reiter, Elmar R., 1963. Jet-Stream Meteorology. Univ. of Chicago Press,
    Chicago, Ill. 515 pp.

Reiter, Elmar R., 1969a. Mean and eddy motions in the atmosphere. Mon.
    Wea. Rev., 97:200-204.

Reiter, Elmar R., 1969b. Atmospheric Transport Processes, Part 1: Energy
    Transfers and Transformations. TID-24868, U.S. Atomic Energy Commission,
    Division of Technical Information Extension, Oak Ridge, Tenn. 212 pp.

Reiter, Elmar R., 1969c. Tropospheric Circulation and Jet Streams, in
    World Survey of Climatology, Vol. 4: Climate of the Free Atmosphere
    (D. F. Rex, Ed.), Elsenier Publishing Co., Amsterdam-London-New York
    1969. 85-202.

Reiter, Elmar R., 1972. Atmospheric Transport Processes, Part 3: Hydro-
    dynamic Tracers. TID-25731, U.S. Atomic Energy Commission, Division
    of Technical Information Extension, Oak Ridge, Tenn. 212 pp.

Sverdrup, Harold Ulrik, Johnson, Martin W., and Fleming, Richard H., 1942.
    The Oceans, Prentice-Hall Inc., Englewood Cliffs, N.J. 1087 pp.

Wagner, James A., 1970. The weather and circulation of January 1970:
    Record cold in the eastern third of the nation and record rainfall
    in the Pacific Northwest. Mon. Wea. Rev., 98:328-334.
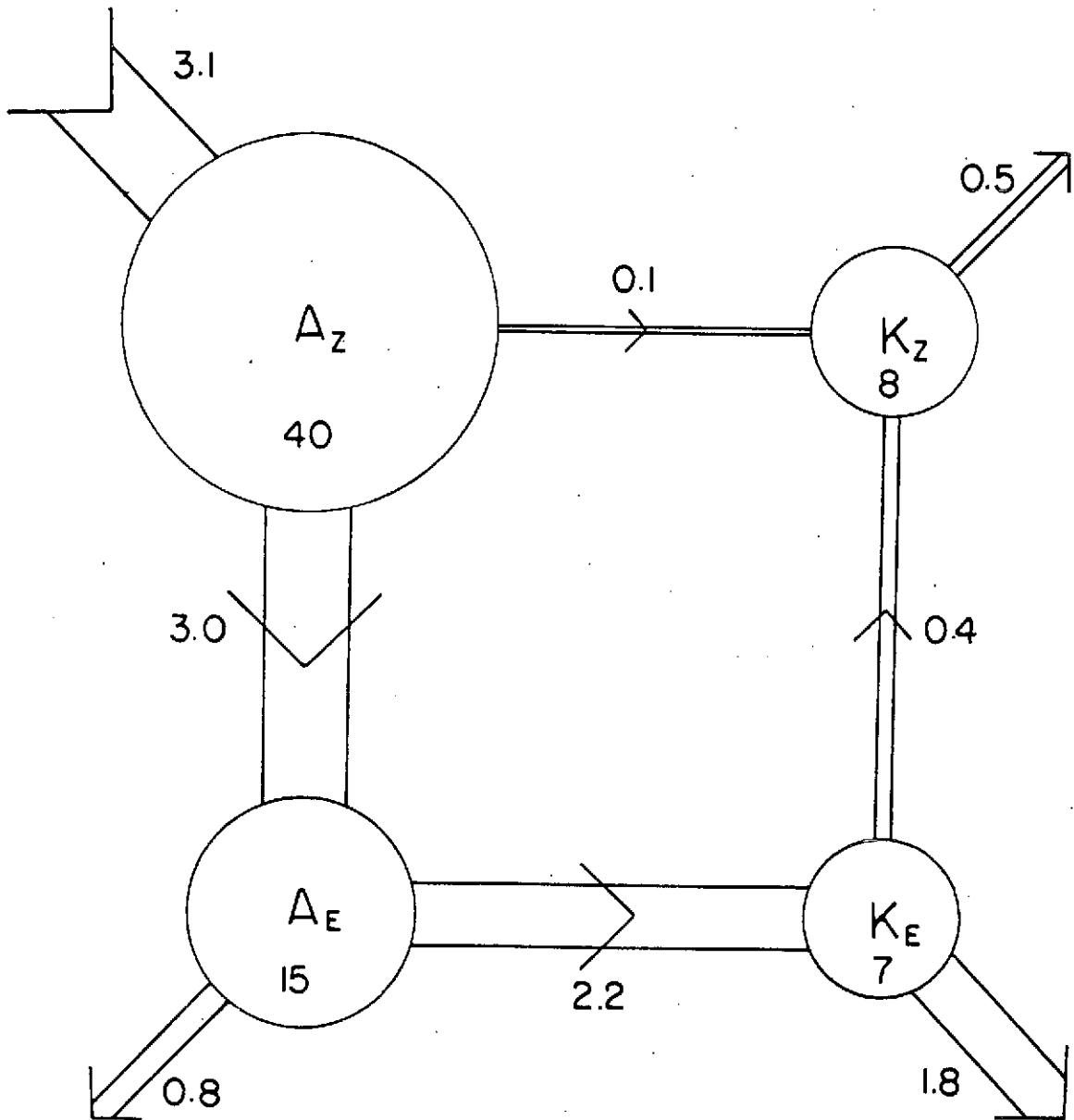
Fig. 1. The energy cycle of the atmosphere as estimated by Oort (1964). Values of energy are in units of 10^5 joules m^{-2}, and values of generation, conversion and dissipation are in watts m^{-2}.
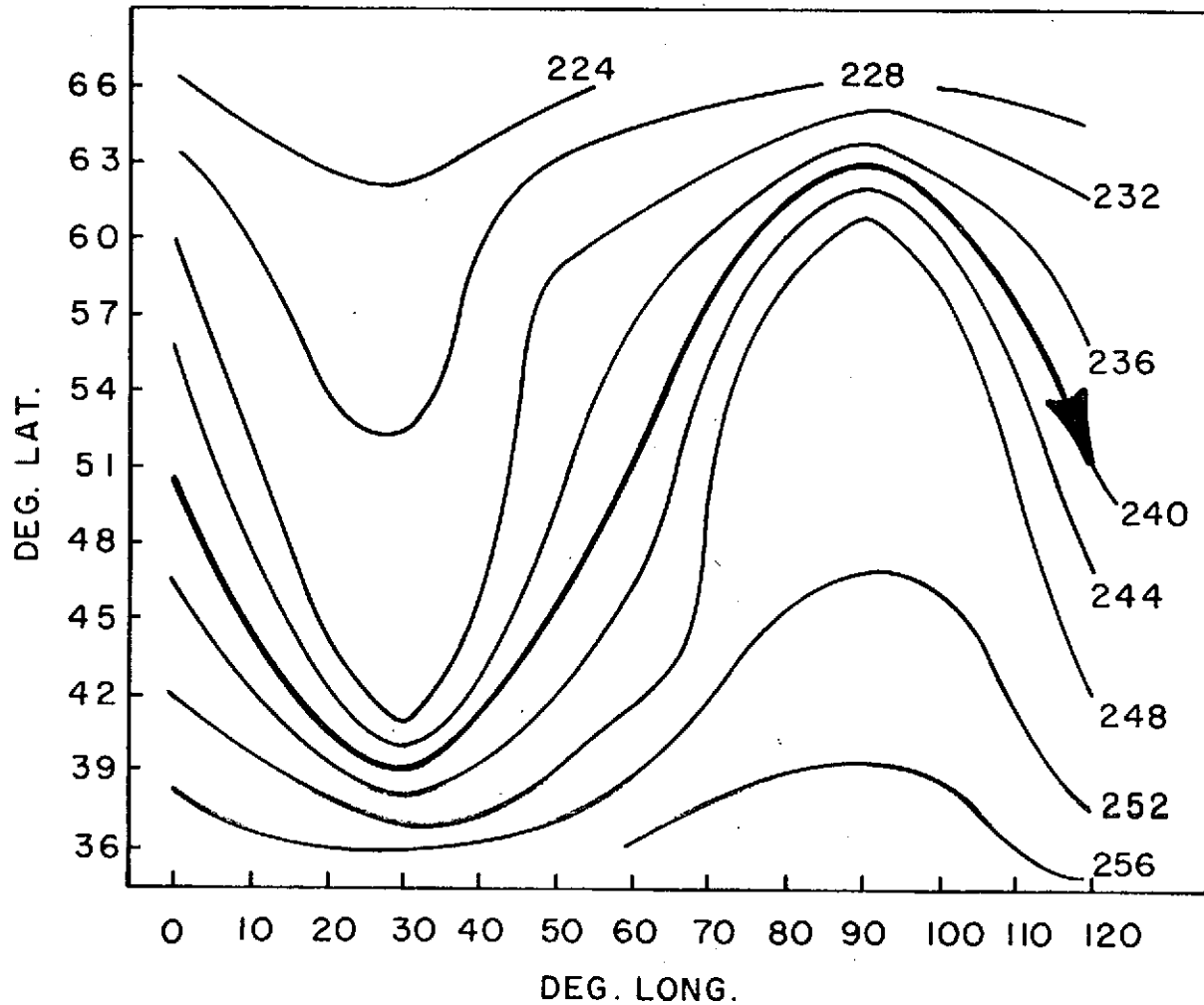
Fig. 2. Schematic illustration of jet-stream level flow and the distribution of underlying layer-mean temperature. The jet axis, the heavy line with arrow-head, is a line joining the maximum wind speeds. The surface wind speed is assumed to be zero everywhere. Hence jet-stream level streamlines are parallel to the layer-mean isotherms (^{O}K).
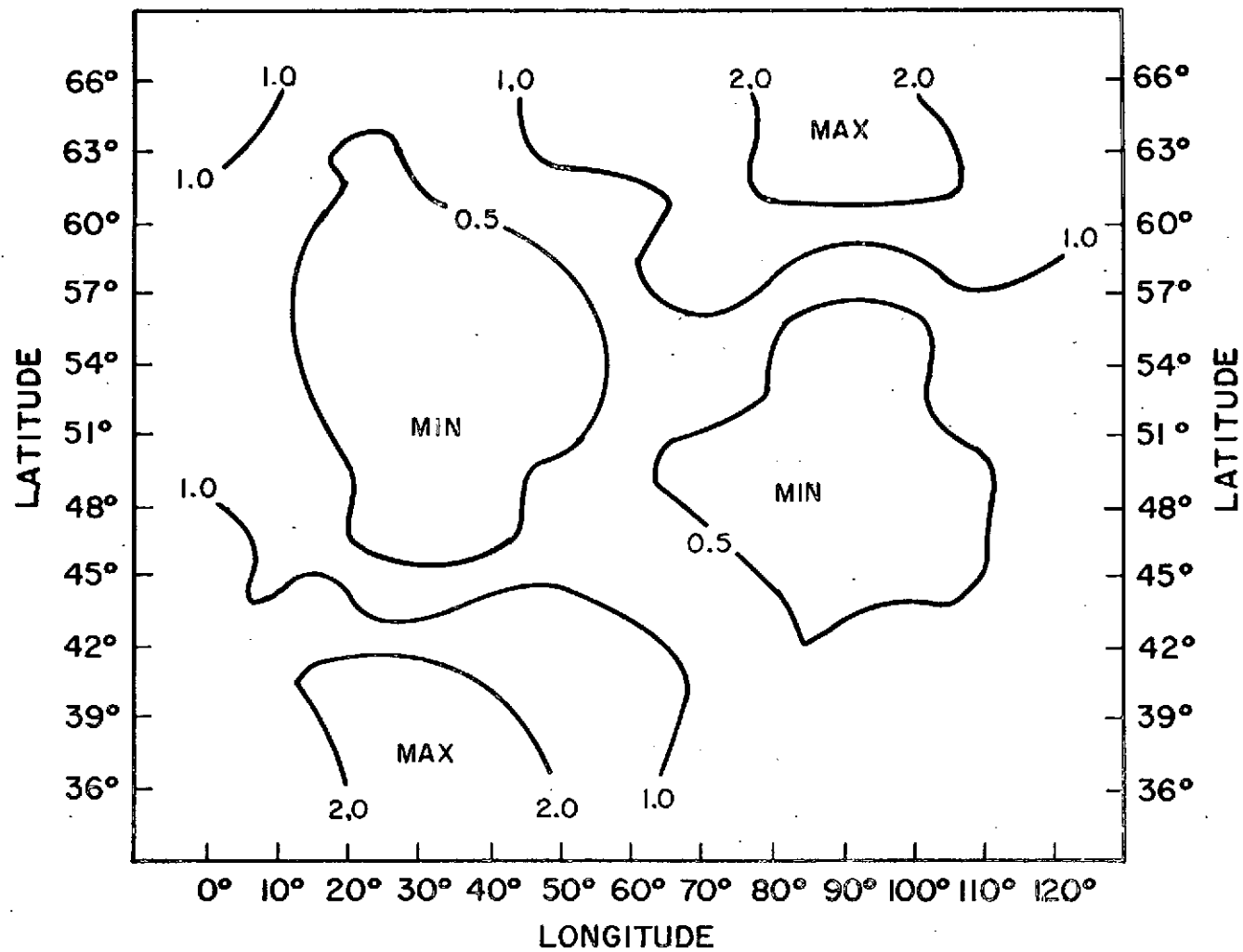
Fig. 3. The meridional temperature gradients $\partial\overline{T}/\partial y$ corresponding to Fig. 2. Units are $^{O}K \ (100 \ Km)^{-1}$.
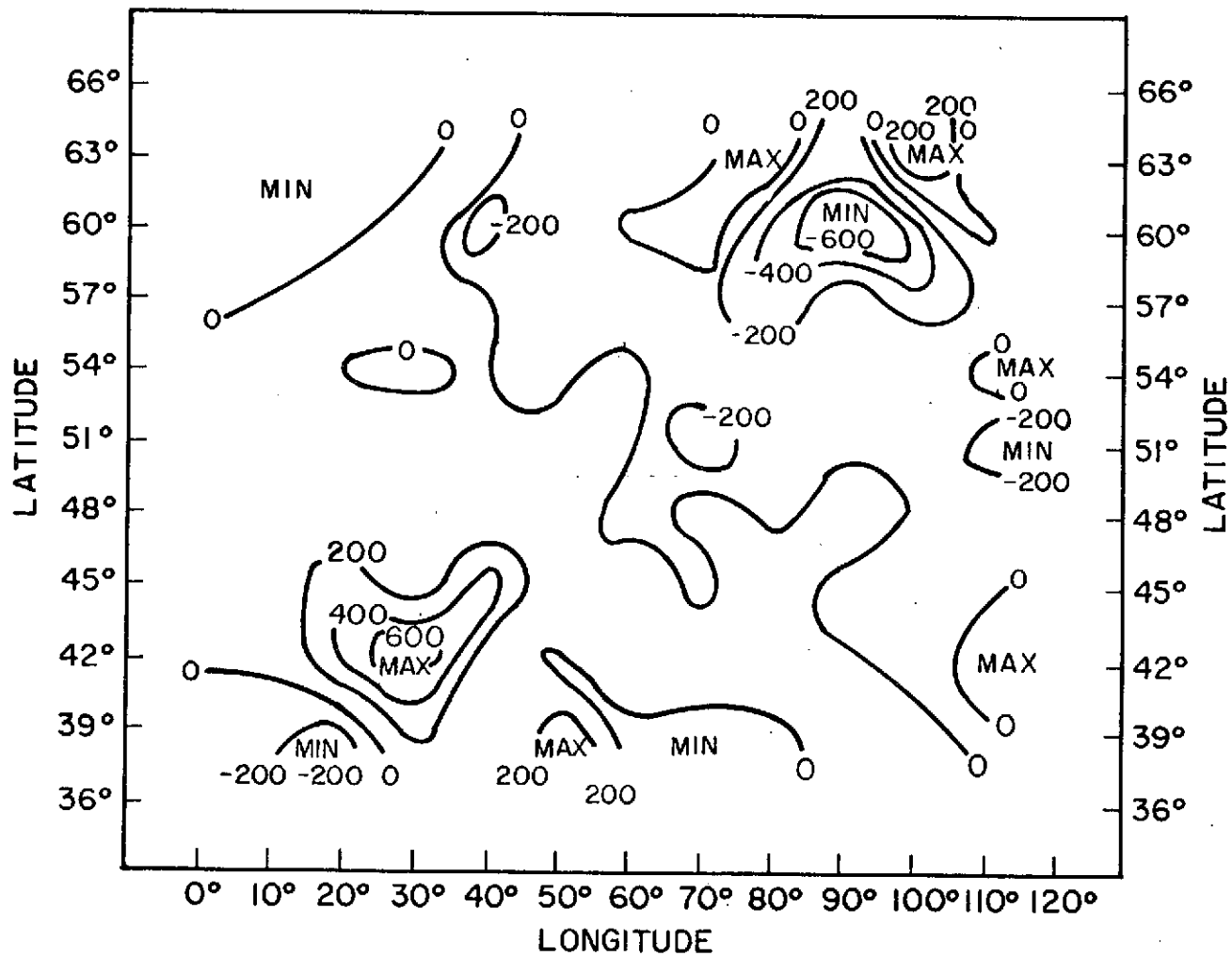
Fig. 4. The distribution of $\nabla_2^2\bar{T}$ corresponding to Fig. 2. Units are $K/10^7 Km^2$.

$$A = \left[\nabla_2^2 \, \overline{T} \right]_{(\lambda)}, \quad °C / 10{,}000 \text{ km}^2$$
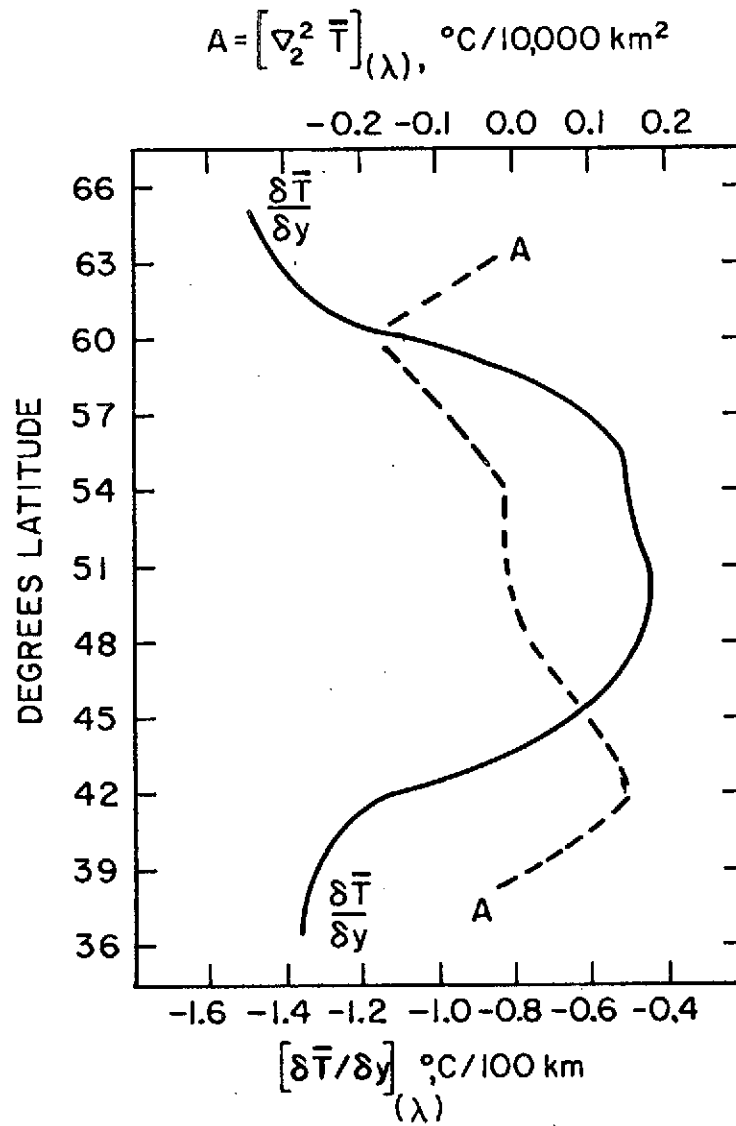
Fig. 5. The zonal averages of $\partial \overline{T} / \partial y$ and $\nabla_2{}^2 \overline{T}$ for the model of Fig. 2.

$$D = \left\{ \nabla_2^2 \, \overline{T} \right\}_{(\lambda)}, \quad °C/10,000 \text{ km}^2$$
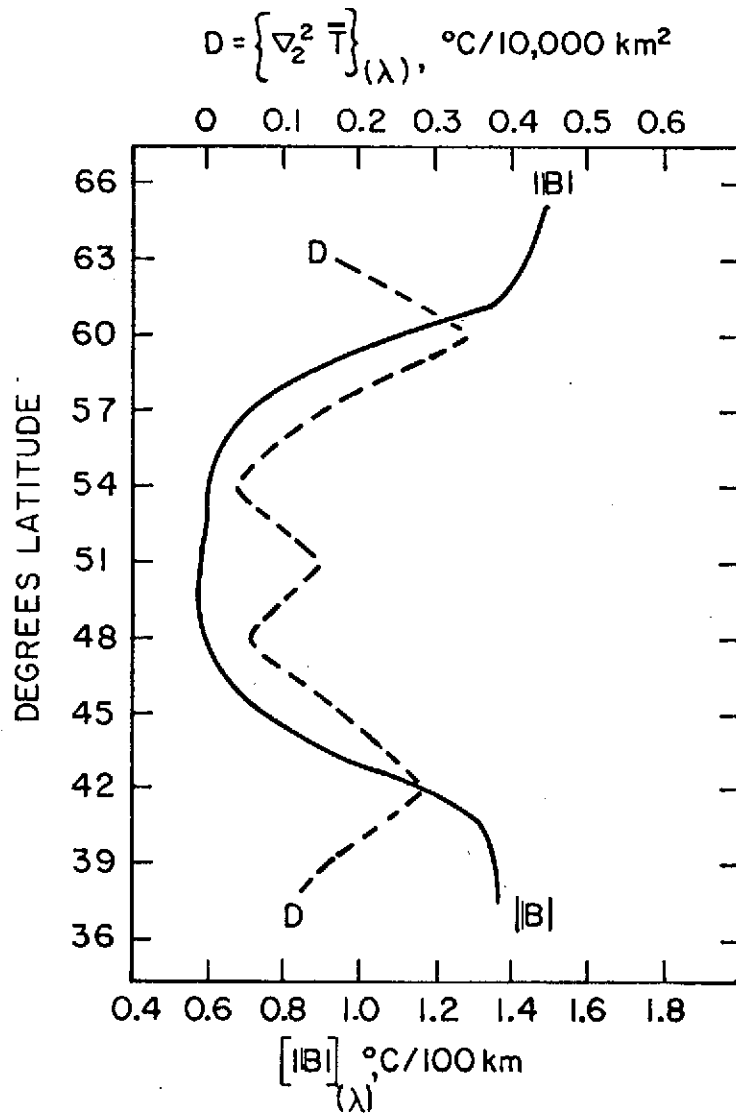
Fig. 6. The zonal averages of the magnitude of the baroclinicity vector $|\mathbb{B}|$; and the zonal r.m.s. values of $\nabla_2^2\overline{T}$ for the model of Fig. 2.
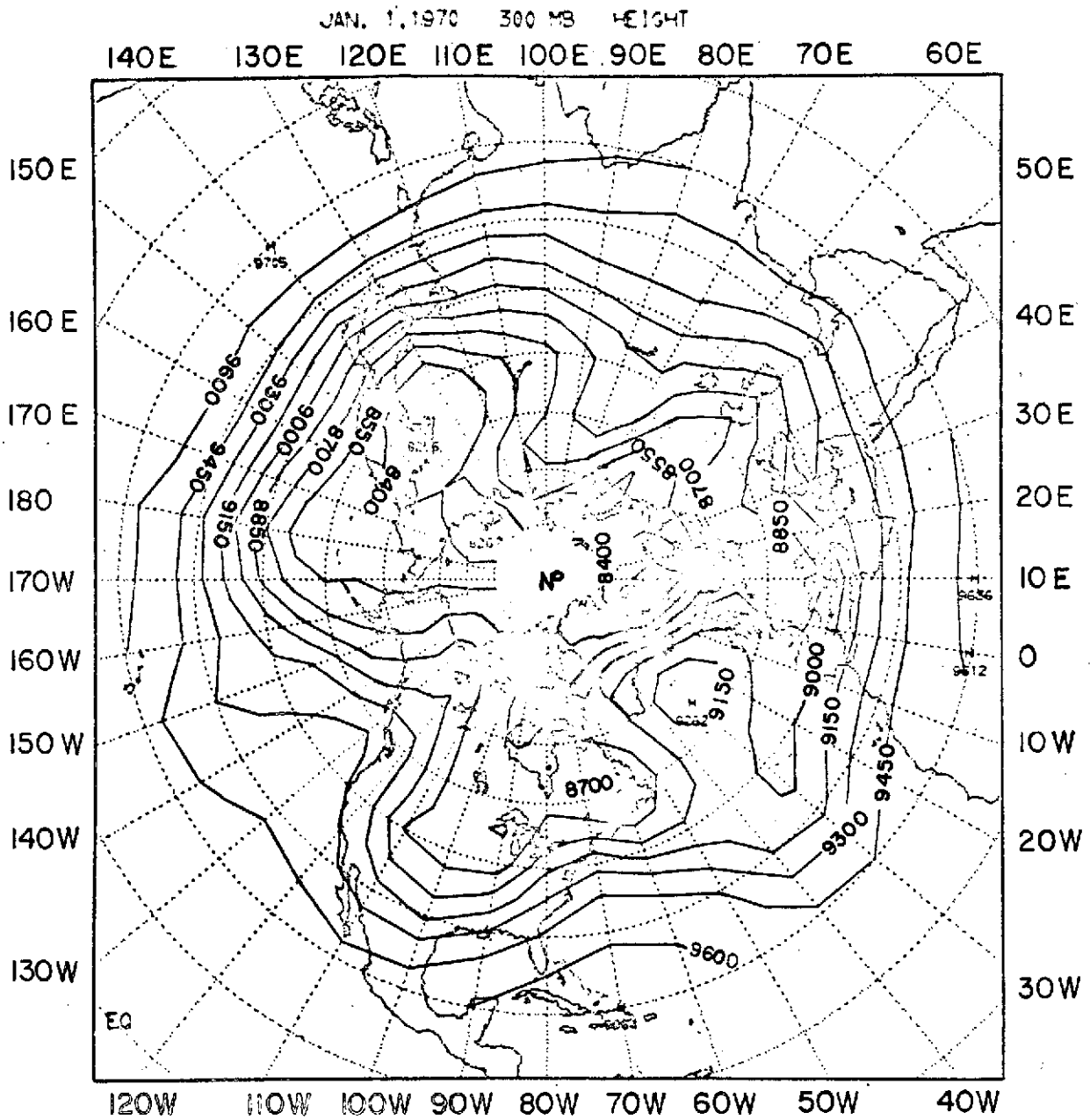
Fig. 7. The geopotential height distribution of the 300 mb surface for
Jan. 1, 1970. Units: geopotential meters.
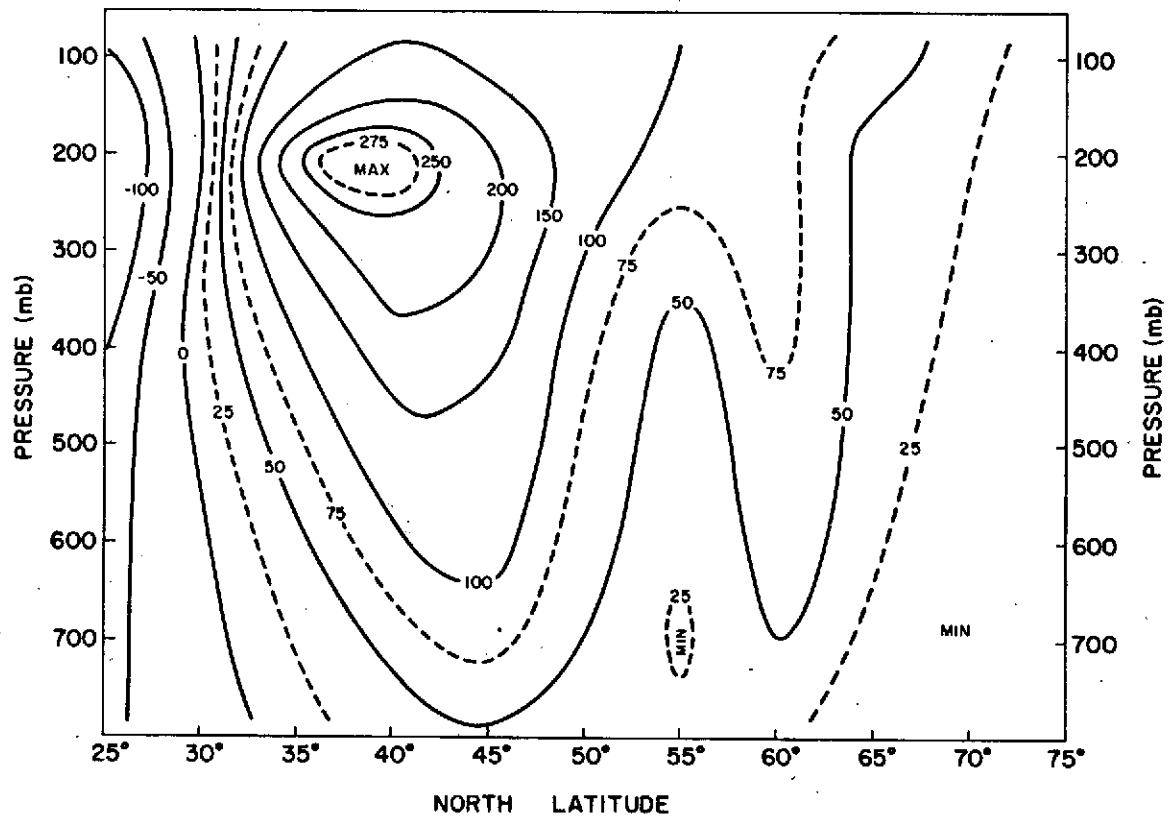
Fig. 8. The distribution of $[\zeta_g]_{(\lambda,t)}$ for Jan. 1970. Units: $10^{-7}s^{-1}$. Symbolism defined in Table 1.
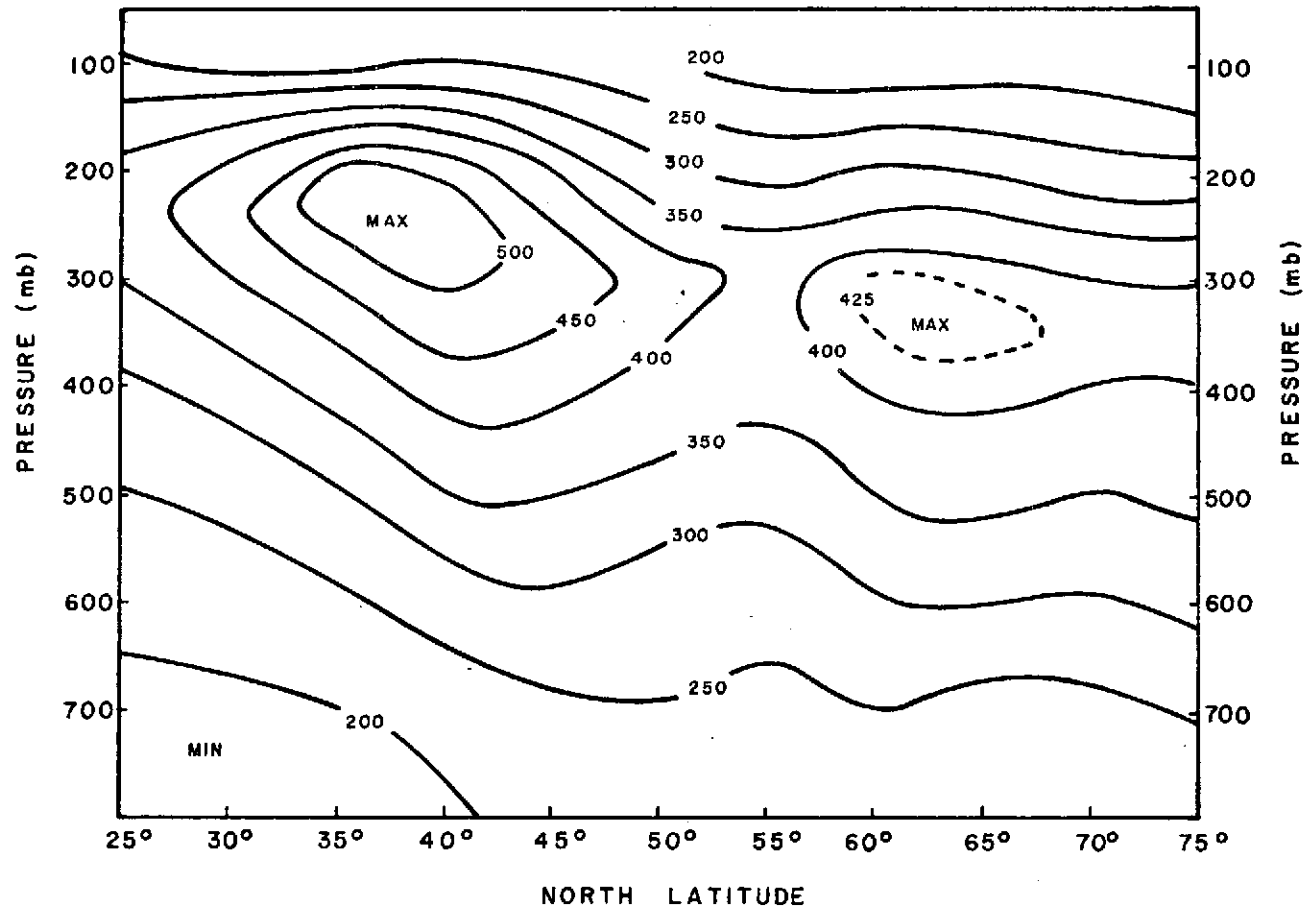
Fig. 9. The distribution of K for Jan. 1970. Units: $10^{-7} s^{-1}$. Symbols defined in Table 1.
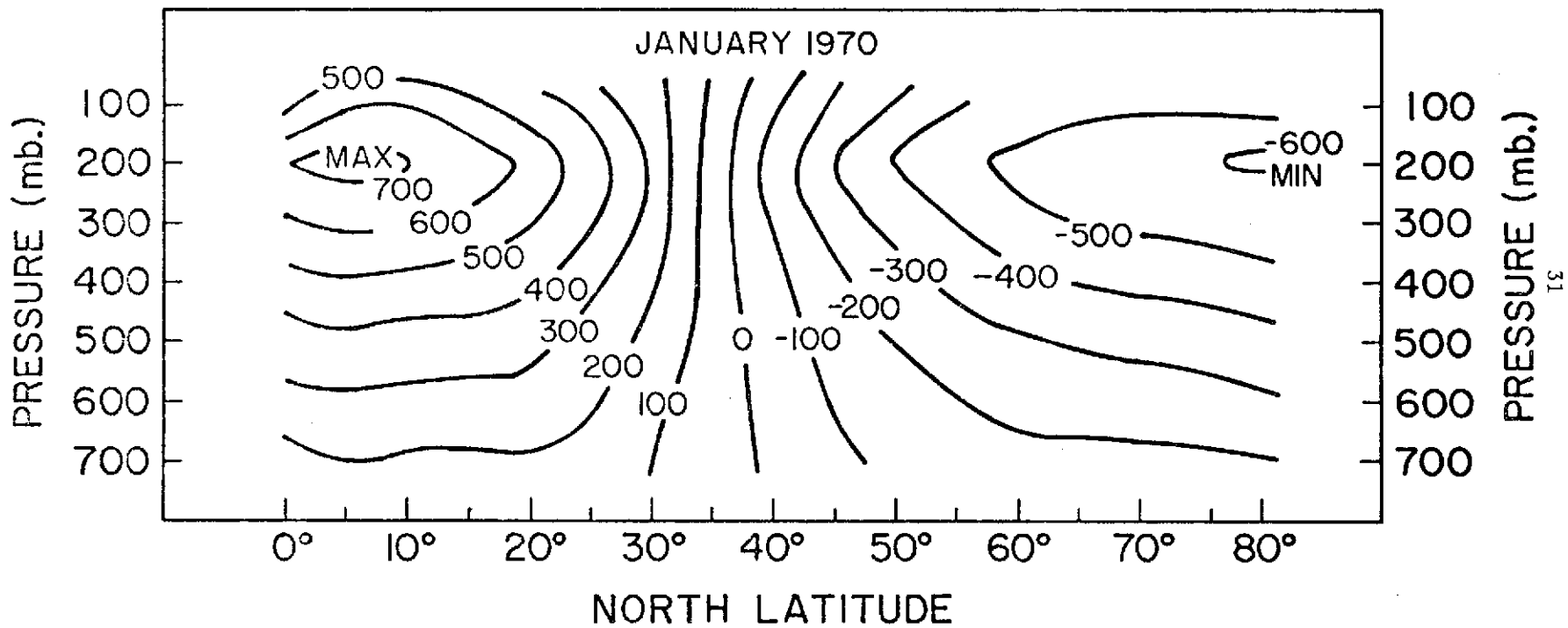
Fig. 10. The distribution of $([H]_{(t,\lambda)})_{(\phi)}$ in Jan. 1970. Units: Geopotential meters. For an explanation of symbols see Table 1.
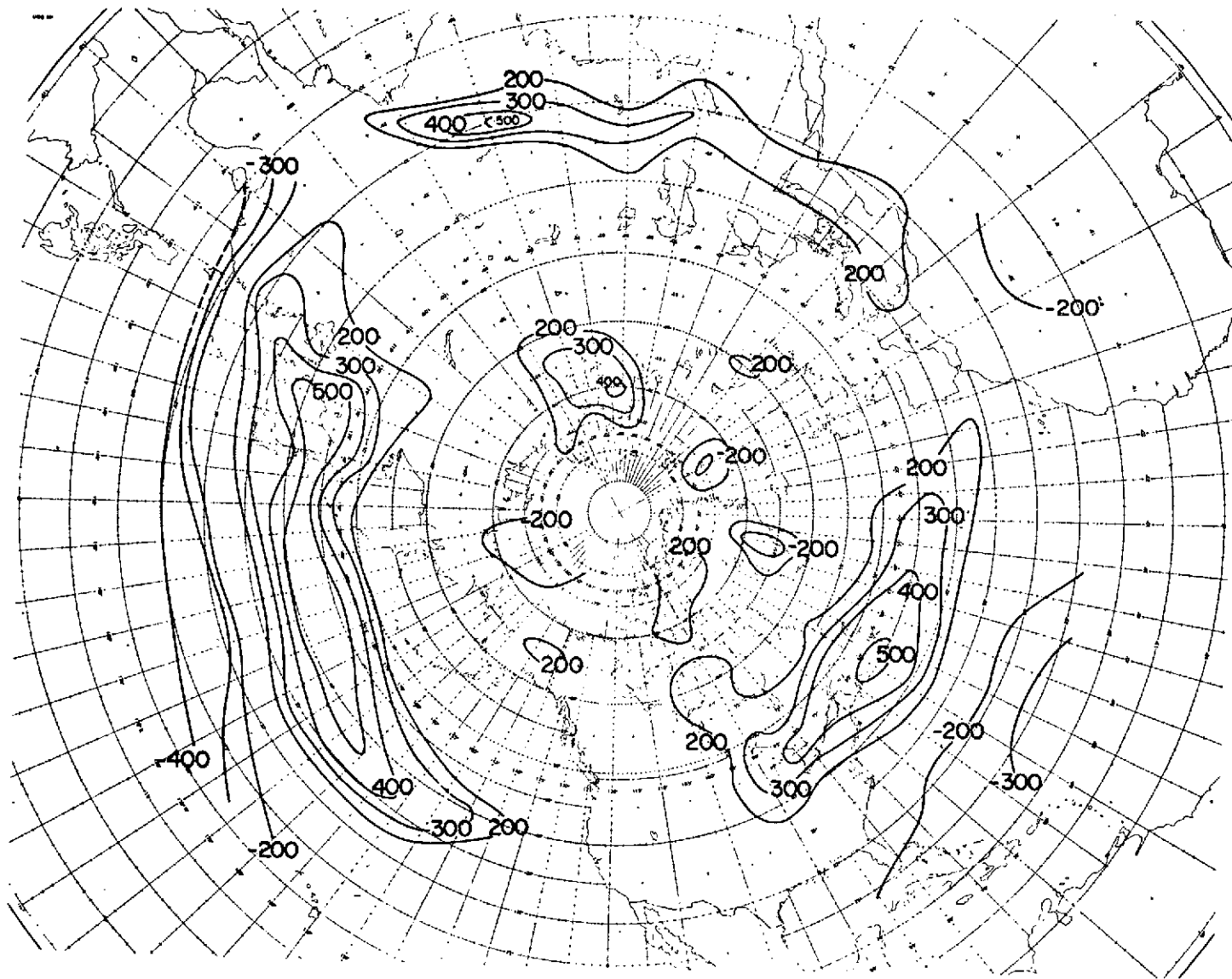
Fig. 11. The geographical distribution of $[\zeta_g]_{(t)}$ at 300 mb in Jan. 1970. Units: $10^{-7}s^{-1}$. The 0, 100, -100 contours were omitted for the sake of clarity.
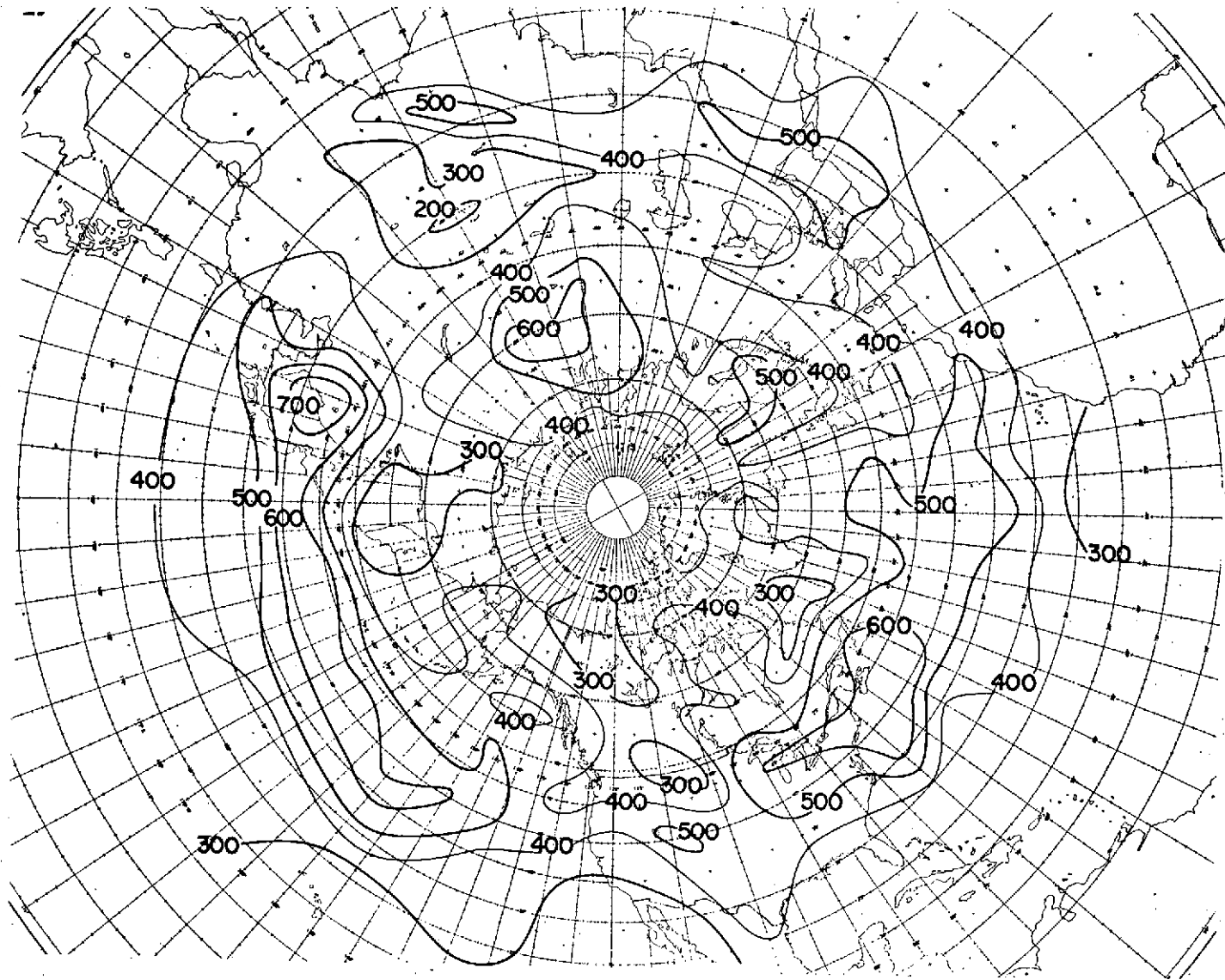
Fig. 12. The geographical distribution of $\{\zeta_g\}_{(t)}$ at 300 mb in Jan. 1970.
Units: $10^{-7}s^{-1}$.
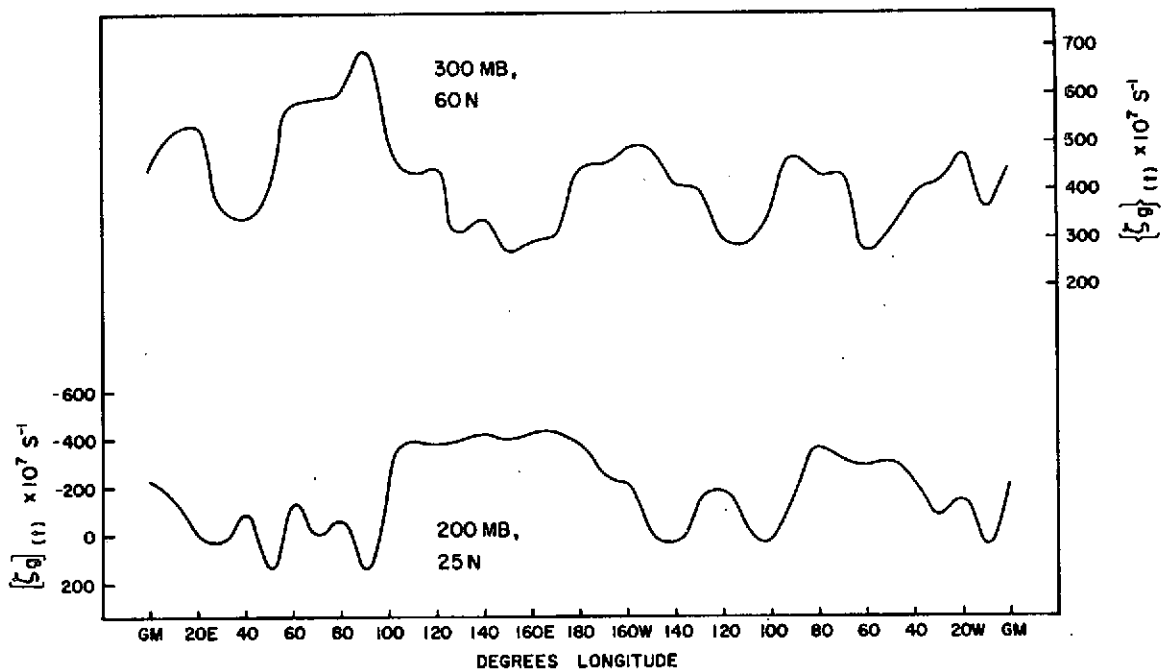
Fig. 13. The zonal distribution of $\{\zeta_g\}_{(t)}$ at 300 mb at 60 N and of $[\zeta_g]_{(t)}$ at 200 mb at 25 N in Jan. 1970.

APPENDIX II

Some Observed Seasonal Changes
in Extratropical General Circulation:
A Study in Terms of Vorticity

SOME OBSERVED SEASONAL CHANGES IN EXTRATROPICAL

GENERAL CIRCULATION: A STUDY IN TERMS

OF VORTICITY

by

Srinivasan Srivatsangam

Department of Atmospheric Science

Colorado State University

Fort Collins, Colorado

August, 1973

Atmospheric Science Paper No. 204

ABSTRACT

Extratropical eddy distributions in four months typical of the four seasons are treated in terms of temporal mean and temporal r.m.s. values of the geostrophic relative vorticity. The geographical distributions of these parameters at the 300 mb level show that the arithmetic mean fields are highly biased representatives of the extratropical eddy distributions.

The zonal arithmetic means of these parameters are also presented. These show that the zonal-and-time mean relative vorticity is but a small fraction of the zonal mean of the temporal r.m.s. relative vorticity, K. The reasons for considering the r.m.s. values as the temporal normal values of vorticity in the extratropics are given in considerable detail.

The parameter K is shown to be of considerable importance in locating the Extratropical Frontal Jet Streams (EFJ) in time-and-zonal average distributions.

The study leads to an understanding of the seasonal migrations of the EFJ which have not been explored until now.

TABLE OF CONTENTS

TABLE OF CONTENTS (cont'd)

LIST OF TABLES

iv

LIST OF FIGURES

1. Introduction

In an earlier paper (Srivatsangam, 1973; hereafter referred to as Paper A) the author presented the results of a study of the distribution of geostrophic relative vorticity in the Northern Hemisphere in Jan. 1970. There vorticity distribution was studied in terms of arithmetic means and root mean square values. The arithmetic zonal-and-time mean values were thereby shown to be but a small fraction of the normal vorticity of the atmosphere. The values of the parameter K given by

$$K = [\{\zeta_g\}_{(\lambda)}]_{(t)} \,\dot{=}\, [\{\zeta_g\}_{(t)}]_{(\lambda)} \tag{1}$$

(for an explanation of symbols please see Table 1) were considered to be the normal values of vorticity in the atmosphere, as opposed to the arithmetic zonal-and-time mean values which represent only the vorticity associated with the long-term zonal circulation, or the field of $[u]_{(t,\lambda)}$ (See, for example, Lorenz, 1967, p. 32.) Since the greater part of the vorticity associated with extratropical jet streams is in eddy form, the consideration of a 'normal' field of vorticity leads to a better understanding of the time-and-zonal mean locations and intensities of jet streams especially because of the great concentration of vorticity just below the tropopause. Above the jet-stream level the concentration of the K isopleths is much greater and helps in distinguishing between the troposphere and the stratosphere.

These encouraging results urged a study of the distribution of K in different seasons and resulted in this report.

1

Table 1

Definitions of Symbols

a   mean radius of the earth.

$f(x,\ldots)$ mathematical function, not the Coriolis acceleration.

$f = 2\,\Omega\,\sin\phi$ Coriolis acceleration.

H   geopotential height

$$K = [\{\zeta_g\}_{(\lambda)}]_{(t)} \simeq [\{\zeta_g\}_{(t)}]_{(\lambda)}$$
$$\simeq \{\zeta_g\}_{(t,\lambda)} \simeq \{\zeta_g\}_{(\lambda,t)}$$

r.h.s.   the right hand side of an Equ.

t   time.

u   zonal component of the observed wind.

u_g zonal component of the geostrophic wind.

$\beta = \partial f/\partial(a\phi)$ the Rossby parameter.

ζ_g relative geostrophic vorticity.

λ longitude.

σ_x the standard deviation of parameter x in some arbitrary independent variable k.

ϕ latitude.

Ω angular velocity of the earth.

$[f]_{(x)}$ the arithmetic mean of $f(x,\ldots)$ in x.

$$[\,[f]_{(x)}\,]_{(y)} = [f]_{(x,y)}$$

$$(f)_{(x)} = f(x,\ldots) - [f]_{(x)}$$

$\{f\}_{(x)}$ the root mean square value of $f(x,\ldots)$ in x.

$$\{f\}_{(x,y)} \simeq \{f\}_{(y,x)}$$

$$([H]_{(t,\lambda)})_{(\phi)} = [H]_{(t,\lambda)} - [H]_{(t,\lambda,\phi)}$$

the deviation of zonally and temporally averaged geopotential height of an isobaric surface from the hemispheric time-mean value.

$|x|$ modulus of x

$< f(x,y) >$ matrix of f in x and y.

2. Data and Analytical Procedure

In this study the distributions of $[\zeta_g]_{(t,\lambda)}, [\{\zeta_g\}_{(\lambda)}]_{(t)}$,
$[H]_{(t,\lambda)} - [H]_{(t,\lambda,\phi)}$ and the geographical distributions of $[\zeta_g]_{(t)}$ and
$\{\zeta_g\}_{(t)}$ for the months July 1969, October 1969, January 1970 and April 1970
are presented and discussed. The data for the study was the daily geo-
potential height distributions of the 700; 500; 400; 300; 200 and 100 mb
surfaces as obtained from the National Meteorological Center (NMC) data
tapes. All months except October 1969 had missing data for a few days.
But for every month studied here we had more than 20 days of data. Thus
the values presented here must be reasonably representative of monthly
averages obtained by including all data. This is not equivalent to
stating that the results presented here are true climatological averages.
This is certainly not the case. Some deviations of these results from
long-period averages will be discussed in later sections of this report.

The analysis for the four months was carried out by Mrs. Alice Fields.
The CDC 6400 computer at the Colorado State University was used for all
calculations. While the daily geopotential height data were being converted
to geostrophic relative vorticity and put on tapes the zonal r.m.s. values
of ζ_g were calculated thus providing us with data for checking the equivalence
of the parameters in Equ. 1. Initially the geographical distributions were
hand analyzed. But later analyses were carried out by the computer.

3. Averaging Conventions

These were discussed in detail in Paper A, and are summarized in Table
1. The averaging conventions followed here are those due to Reiter (1969a;
1969b, p. 6-8) and Srivatsangam (Paper A) . As discussed in Paper A, in
general

$$[\{\zeta_g\}_{(t)}]_{(\lambda)} \neq [\{\zeta_g\}_{(\lambda)}]_{(t)} \tag{2}$$

since the $<|\zeta_g(\lambda,t)|>$ matrices are non-square and do not have identical values for each matrix element. But apparently the $|\zeta_g(t,\lambda)|$ values are sufficiently homogeneous so that the inequality sign in Equ. (2) above may be replaced by an "equal" sign. This was shown to be the case for Jan. 1970 in Paper A. In the present paper we present the values for the other three months of $[\{\zeta_g\}_{(t)}]_{(\lambda)}$ and $[\{\zeta_g\}_{(\lambda)}]_{(t)}$ in Appendices 1, 1a and 1b. From these data it is seen readily that for each of the month considered the approximation of Equ. 1 holds.

4. The Distribution of $[\zeta_g]_{(t,\lambda)}$

In Figures 1a to 1d the distribution of $[\zeta_g]_{(t,\lambda)}$ during each of the 4 months considered is presented. There is considerable similarity between the distributions of July, October and April, especially in the middle latitudes (40N to 60N). In these latitudes mild cyclonic conditions ($\zeta_g \simeq 1 \times 10^{-5}s^{-1}$ at the jet-stream level) prevail. In the subpolar latitudes (60N to 75N) cyclonic velocity of smaller magnitude prevails in October and April, and anticyclonic mean conditions are obtained only in July. The major difference between these 3 months is the July intensification and northward displacement of the subtropical high pressure systems. The movement is seen to be some 10 Deg. latitude northward. The intensity nearly doubles in the 200 mb-300 mb layer. From Appendices 3 and 4 it might be seen that the intensity of the subtropical high pressure systems at 25N, 200 mb in January exceeds the July maximum at 200 mb at 35N. The January distribution of $[\zeta_g]_{(t,\lambda)}$ is also of interest because of the occurrence of the absolute maximum of $[\zeta_g]_{(t,\lambda)}$ among all the 4 months considered. This

is located at the level of the Subtropical Jet Stream (200 mb) but to the north of the STJ axis, which is at about 27N (see Krishnamurti, 1961). The poleward displacement of the $[\zeta_g]_{(t,\lambda)}$ maximum relative to the STJ axis is due to the fact that the isotach maxima imbedded in the STJ are some 5 to 10 deg. latitude poleward of the STJ axis (see Krishnamurti, op. cit.)

Since the distribution of $[\zeta_g]_{(t,\lambda)}$ represents the vorticity distribution due to the zonally and temporally averaged zonal geostrophic motion or $[u_g]_{(t,\lambda)}$ this field offers a valuable check into our calculations. $[u_g]_{(t,\lambda)}$ is readily computed from the $[H]_{(t,\lambda)}$ field by the geostrophic relationship:

$$[u_g]_{(t,\lambda)} = \frac{1}{f} \frac{\partial}{\partial y} [H]_{(t,\lambda)} \tag{3}$$

The values of $[H]_{(t,\lambda)}$ for the 4 months considered here are presented in Appendix 2. From these the geostrophic wind and geostrophic relative vorticity were computed, the latter from the expression

$$[\zeta_g]_{(t,\lambda)} = \frac{\tan \phi}{af} \frac{\partial}{\partial y} [H]_{(t,\lambda)} - \frac{1}{f} \frac{\partial^2}{\partial y^2} [H]_{(t,\lambda)}$$

$$+ \frac{\beta}{f^2} \frac{\partial}{\partial y} [H]_{(t,\lambda)} \tag{4}$$

and are presented in Appendices 3 and 4 respectively. It might be seen that Equ. 4 includes both the meridional shear of $[u]_{(t,\lambda)}$ and the effect of the convergence of meridians on $[u]_{(t,\lambda)}$. A comparison of the values of $[\zeta_g]_{(t,\lambda)}$ in Appendix 4 and the values in Figures 1a to 1d shows that the two are quite comparable.

In order to check the correctness of our results further and to compare the properties of the circulation systems of the 1969-1970 period with those

of more truly climatic averages, the 5-year mean geopotential height data

presented by Oort and Rasmusson (1971, p. 84) were converted into

$[u_g]_{(t,\lambda)}$ and $[\zeta_g]_{(t,\lambda)}$ values and presented as Appendices 5 and 6

respectively. Oort and Rasmusson did not present such computed results

except for $[u_g]_{(t,\lambda)}$ at the 200 mb level (Oort and Rasmusson, 1971,

p. 18).

A comparison of $[u_g]_{(t,\lambda)}$ in Appendices 3 and 5 shows that the monthly

means for 1969-70 did not differ very much from the 5-year means, except

in January. The maxima in July, October and April are in good agreement

with regard to magnitude. In July 1969 the maximum is at 42.5N and has

a value of 22.6 ms^{-1}; the corresponding values for the 5-year period are

42.5N and 21.8 ms^{-1}. In October 1969 the maximum is at 42.5N and has a

value of 27.7 ms^{-1}; the corresponding values for the 5-year period are 37.5N

and 28.6 ms^{-1}, indicating a northward displacement of the maximum in 1969.

In January and April the maxima of $[u_g]_{(t,\lambda)}$ are spread out latitudi-

nally. (This is also true of October.) Table 2 gives the magnitudes.

and the latitudes of occurrence of maxima for these two months from which

it is seen that the April 1970 maximum was relatively more spread-out and

that the January 1970 maximum had a higher value than the 5-year data

maximum, the excess being some 6 ms^{-1} at 32.5N. This excess is probably

due to the anomalies of the geopotential height fields in January 1970 which

amounted to -100m and -170m over the Pacific and Atlantic Oceans respectively,

at the 700 mb level. (For further discussion see Paper A.)

It should be mentioned here that the geostrophic zonal wind is generally

an overestimate of the true zonal wind in the zones of strong westerly

winds. This is due to the fact that the geostrophic wind is a non-accelerated

wind whereas zonal winds with trajectories similar to latitude circles must

be decelerated, and this is approximately true of winds in the vicinity of

the STJ (see Lorenz, 1967, p. 33). Hence in general

$$[u]_{(t,\lambda)} < [u_g]_{(t,\lambda)} \tag{5}$$

(see also Oort and Rasmusson, 1971, p. 17-18).

The effect of this on the relationship between $[\zeta]_{(t,\lambda)}$ and $[\zeta_g]_{(t,\lambda)}$

could not be studied for the 1969-70 period since we were not computing

$[u]_{(t,\lambda)}$. But a check was possible through the Oort and Rasmusson (op. cit.)

data.

In Appendix 7 we present the values of $[\zeta]_{(t,\lambda)}$ obtained from the

$[u]_{(t,\lambda)}$ data of Oort and Rasmusson (1971, p. 76-77). A comparison of

these values with the $[\zeta_g]_{(t,\lambda)}$ values for the same period (see Appendix 6)

shows that the geostrophic vorticity is an overestimate of the vorticity

associated with the observed zonal wind. Thus, in general

$$|[\zeta]_{(t,\lambda)}| < |[\zeta_g]_{(t,\lambda)}| \tag{6}$$

Hence the values of the different vorticity parameters presented in this

paper must all be considered to be slight overestimates of the observed

values. (See also Reiter 1963, p. 18.)

A consideration of the $[\zeta_g]_{(t,\lambda)}$ distributions of Appendices 4 and 6

shows that the magnitudes of $[\zeta_g]_{(t,\lambda)}$ in the period 1969-70 were comparable

to the mean vorticity in the 5-year period analyzed by Oort and Rasmusson.

The ratio of our data to the Oort and Rasmusson data at the 200 mb level at 40N

in January - where the annual maximum of $[\zeta_g]_{(t,\lambda)}$ occurs - is approximately

11:9 which is comparable to the ratio of the $[u_g]_{(t,\lambda)}$ maxima which is 10:9.

Table 2

The Magnitudes and Latitudes of Occurrence of

$[u_g]_{(t,\lambda)}$ Maxima in January and April

Units: ms^{-1}

LAT. DEG. NORTH	JAN		APR	
	ORa	SRI	ORa	SRI
27.5	45.3	48.1	33.3	30.8
32.5	44.8	50.9	34.2	33.5
37.5				31.0

NB: ORa stands for Oort and Rasmusson (1971).
SRI stands for the present report.
All maxima are at the 200 mb level.

5. **The Distribution of Mass or** $[H]_{(t,\lambda)} - [H]_{(t,\lambda,\phi)}$

Because of the inter-relationship between the distribution of $[H]_{(t,\lambda)} - [H]_{(t,\lambda,\phi)}$ and the field of $[u_g]_{(t,\lambda)}$ (see Equ. 3) the former is of considerable meteorological interest. Although the literature abounds with statistics of the latter parameter (see, for example, Lorenz, 1967, p. 32-39) the related distribution of mass has never been presented in the form $[H]_{(t,\lambda)} - [H]_{(t,\lambda,\phi)}$, as far as the author knows. This might be due to the difficulty in establishing an acceptable value of $[H]_{(t,\lambda,\phi)}$. The difficulty arises because of the observed fact that the thermal equator of our planet does not coincide with its geographical equator. The thermal equator is a surface which has considerable variability in the ϕ, λ, t coordinates and also to a lesser extent in p over a belt of (ϕ, λ, t). Thus the true value of $[H]_{(t,\lambda,\phi)}$ which could only be obtained by averaging the values of (t, λ, ϕ, p) in a "meteorological hemisphere," i.e., a hemisphere defined with respect to the meteorological equator, becomes a considerable task. If the value of $[H]_{(t,\lambda,\phi)}$ were not exact, the zero isopleth of the $[H]_{(t,\lambda)} - [H]_{(t,\lambda,\phi)}$ distribution will be misplaced and so also all the other isopleths.

On the other hand the $[u_g]_{(t,\lambda)}$ distribution depends only upon the local geopotential height gradients measured over isobaric surfaces, and does not involve assumptions about the mean mass field.

Despite all these considerations the author chooses to present the mean mass fields for the different months considered in Figures 2a to 2d. Here the value of $[H]_{(t,\lambda,\phi)}$ has been assumed to be $[H]_{(t,\lambda)}$ arithmetically averaged over the latitudinal belt equator to 80N. The magnitudes of the isopleths in these diagrams could not be given much significance in view of the above considerations, especially in July when the meteorological equator is

well into the northern hemisphere continents. However, Figures 2b to 2d are probably representative of the actual mean mass distribution in the northern "meteorological hemisphere" because the meteorological equator is southward of the geographical equator, thus equalizing the effects of lack of data north of 80N.

The relative concentration of the isopleths of $[H]_{(t,\lambda)} - [H]_{(t,\lambda,\phi)}$ in a zonal belt is an indicator of the intensity of $[u_g]_{(t,\lambda)}$ in that belt. Comparisons of Figures 2a to 2d and the tabulated values of $[u_g]_{(t,\lambda)}$ for the corresponding months in Appendix 3 reveals the mutual agreement of the data.

6. Some Properties of $\{\zeta_g\}_{(t)}$ and K

Some of the mathematical properties of the parameter K which is defined through Equ. 1 have been discussed in Section 3 above. Several of the meteorological properties and uses of K were described in Paper A. Here we shall treat the mathematics of the process of taking root mean square values of meteorological quantities and consider their implications to the general circulation of the atmosphere.

First of all, we shall consider some of the fundamental reasons under-lying this study.

The distinguishing feature of the root mean square averaging procedure as applied to an inhomogeneous array of positive and negative numbers is that the signs of the numbers are not taken into account but only the magnitudes. The vorticity of extratropical eddies might be considered as constituting such an array (in time) at each different location (ϕ,λ,p). The temporal arithmetic average of such an array enables us to quantitatively state the mean cyclonic vorticity or anticyclonic vorticity of these locations.

These mean quantities could be further averaged with respect to meridians to obtain zonal-and-time averages, such as are presented in Figures 1a to 1d; these then represent the temporal mean cyclonic vorticity and anticyclonic vorticity of the different latitudes or zonal belts.

These mean values have considerable significance if the array is reasonably homogeneous, i.e., if the fluctuations from the mean state are of small magnitudes. Symbolically, any meteorological parameter -- and here we shall consider geostrophic relative vorticity -- could be represented at each location (t, λ, ϕ, p) by

$$\zeta_g = [\zeta_g]_{(t)} + (\zeta_g)_{(t)}$$

$$= \underset{a}{[\zeta_g]_{(t,\lambda)}} + \underset{b}{([\zeta_g]_{(t)})_{(\lambda)}} + \underset{c}{[(\zeta_g)_{(t)}]_{(\lambda)}}$$

$$+ \underset{d}{(\zeta_g)_{(t,\lambda)}} \tag{7}$$

Here term a represents the vorticity of the zone-and-time averaged zonal geostrophic wind, or, in Lorenz's (1967, p. 32) terminology the vorticity of the long-term (geostrophic) zonal circulation; term b represents the vorticity of the standing eddies; term c that of the transient zonal circulations; and term d the vorticity of the transient eddies.

Let us consider the effect of arithmetic averaging on these four terms. Taking the temporal mean first,

$$[\zeta_g]_{(t)} = \underset{a}{[\zeta_g]_{(t,\lambda)}} + \underset{b}{([\zeta_g]_{(t)})_{(\lambda)}} \tag{8}$$

Here the second average with respect to time is omitted on the right hand side since it is not necessary, being already included in the two terms. From Equ. 8 we see that the time averaging has eliminated the

transient eddies and the transient zonal circulations. Let us consider regions of the globe where

$$|c| + |d| >> |a| + |b| \qquad (9)$$

where the letters denote the terms in Equ. 7. Then maps of $[\zeta_g]_{(t)}$ are not good representatives of the normal weather conditions of these locations, as might be seen from Equ. 8.

The arithmetic averaging of Equ. 8 with respect to meridians leads to

$$[\zeta_g]_{(t,\lambda)} = [\zeta_g]_{\underset{a}{(t,\lambda)}} \cdot$$

Thus the distribution of $[\zeta_g]_{(t,\lambda)}$ would not represent normal meteorological conditions fairly if

or,

$$\left.\begin{array}{c} |b| + |c| + |d| >> |a| \\[2mm] \left| \left([\zeta_g]_{(t)}\right)_{(\lambda)} \right| + \left| \left[(\zeta_g)_{(t)}\right]_{(\lambda)} \right| + \left| (\zeta_g)_{(t,\lambda)} \right| \\[2mm] >> \left| [\zeta_g]_{(t,\lambda)} \right| \end{array}\right\} \qquad (10)$$

Inequality (10) is quite valid in the extratropics where the observed synoptic state is usually a disturbed state, and leads to an inequality such as (22) below.

Eddies are of very considerable importance in the extratropics. In fact neither the climate nor the weather of the extratropics could be understood without accounting for the eddies.

One way to study these eddy phenomena is to study the variances of the observed wind, temperature and other fields as is done in the extensive literature on the subject of available potential energy (see, for example,

Lorenz, 1967, and Reiter 1969b, for complete lists of references).
However, there is a need to represent the normal state of the extratropical
atmospheric circulation systems in time and time-and-longitude averaged
distributions (see Paper A).

The distributions of $\{\zeta_g\}_{(t)}$ and of K will be shown to filfill this
need.

From Equ. 7, ζ_g^2 could be obtained in the following form by simple
algebraic expansion:

$$\zeta_g^2 = \left[[\zeta_g]_{(t,\lambda)} + ([\zeta_g]_{(t)})_{(\lambda)} \right]^2$$

$$+ \left[([\zeta_g]_{(\lambda)})_{(t)} + (\zeta_g)_{(t,\lambda)} \right]^2$$

$$+ 2 \left[[\zeta_g]_{(t,\lambda)} + ([\zeta_g]_{(t)})_{(\lambda)} \right] \left[([\zeta_g]_{(\lambda)})_{(t)} + (\zeta_g)_{(t,\lambda)} \right] \tag{11}$$

Here and in what follows the heavy square brackets do not have any significance
in averaging. Equ. 11 could be further expanded to give:

$$\zeta_g^2 = \underset{I}{[\zeta_g]^2_{(t,\lambda)}} + \underset{II}{([\zeta_g]_{(t)})^2_{(\lambda)}}$$

$$+ \underset{III}{([\zeta_g]_{(\lambda)})^2_{(t)}} + \underset{IV}{(\zeta_g)^2_{(t,\lambda)}}$$

$$+ \underset{V}{2[\zeta_g]_{(t,\lambda)}([\zeta_g]_{(t)})_{(\lambda)}} + \underset{VI}{2 ([\zeta_g]_{(\lambda)})_{(t)}(\zeta_g)_{(t,\lambda)}}$$

$$+ \underset{VII}{2[\zeta_g]_{(t,\lambda)}([\zeta_g]_{(\lambda)})_{(t)}} + \underset{VIII}{2 [\zeta_g]_{(t,\lambda)}(\zeta_g)_{(t,\lambda)}}$$

$$+ \underset{IX}{2([\zeta_g]_{(t)})_{(\lambda)}([\zeta_g]_{(\lambda)})_{(t)}} + \underset{X}{2([\zeta_g]_{(t)})_{(\lambda)}(\zeta_g)_{(t,\lambda)}} \tag{12}$$

In Equ. 12 term I is merely the square of the vorticity of the longterm zonal circulation; terms II, III and IV represent the variances of the vorticity due to standing eddies, transient zonal circulations and transient eddies, respectively. The other six terms represent the correlations between the terms a, b, c and d of Equ. 7. Term V represents the correlation between the vorticity of the longterm zonal circulation and of the standing eddies; term VI represents the correlation between transient zonal circulations and transient eddies. It might be noted that in time-averaging ζ_g^2 these terms will not disappear, there being no reason to assume *a priori* that transient zonal circulations and transient eddies are totally uncorrelated. However, terms VII to X will all disappear in time-averaging because each of these is the product of one transient and one non-transient component. Hence:

$$[\zeta_g^2]_{(t)} = [[\zeta_g]^2_{(t,\lambda)}]_{(t)} + [([\zeta_g]_{(t)})^2_{(\lambda)}]_{(t)}$$

$$+ [([\zeta_g]_{(\lambda)})^2_{(t)}]_{(t)} + [(\zeta_g)^2_{(t,\lambda)}]_{(t)}$$

$$+ 2[[\zeta_g]_{(t,\lambda)}([\zeta_g]_{(t)})_{(\lambda)}]_{(t)}$$

$$+ 2[([\zeta_g]_{(\lambda)})_{(t)}(\zeta_g)_{(t,\lambda)}]_{(t)} \qquad (13)$$

Further averaging of Equ. 13 with respect to meridians eliminates the 5th and 6th right hand side terms because both of these terms involve one component which is a departure from the zonal average. Hence:

$$[[\zeta_g^2]_{(t)}]_{(\lambda)} = [\{\zeta_g\}^2_{(t)}]_{(\lambda)}$$

$$= [[\zeta_g]^2_{(t,\lambda)}]_{(t,\lambda)} + [([\zeta_g]_{(t)})^2_{(\lambda)}]_{(t,\lambda)}$$

$$+ [([\zeta_g]_{(\lambda)})^2_{(t)}]_{(t,\lambda)} + [(\zeta_g)^2_{(t,\lambda)}]_{(t,\lambda)} \qquad (14)$$

It is immediately seen that Equ. 14 is just an expanded meteorological form of the well-known statistical equation:

$$\sigma_x^2 = \overline{x^2} - \overline{x}^2$$

or,

$$\overline{x^2} = \overline{x}^2 + \sigma_x^2 \qquad (15)$$

where σ_x is the standard deviation of the parameter x in some independent variable k with respect to which arithmetic averaging (denoted by $-$) is done.

In order to obtain mathematical expressions for the parameters used in this report we take the square-root of Equ. 13. Hence:

$$\{\zeta_g\}_{(t)} = \left[[[\zeta_g]^2_{(t,\lambda)}]_{(t)} + [([\zeta_g]_{(t)})^2_{(\lambda)}]_{(t)} \right.$$

$$+ [([\zeta_g]_{(\lambda)})^2_{(t)}]_{(t)} + [(\zeta_g)^2_{(t,\lambda)}]_{(t)}$$

$$+ 2[[\zeta_g]_{(t,\lambda)}([\zeta_g]_{(t)})_{(\lambda)}]_{(t)}$$

$$\left. + 2[([\zeta_g]_{(\lambda)})_{(t)}(\zeta_g)_{(t,\lambda)}]_{(t)} \right]^{1/2} \qquad (16)$$

Thus the $\{\zeta_g\}_{(t)}$ values are seen to contain the correlation between the vorticity of the longterm zonal circulation and of the standing eddies, that between the vorticity of the transient zonal circulations and of the transient eddies (the 5th and 6th r.h.s. terms in Equ. 16) as well as the variances of the deviations from the vorticity of the longterm circulation

(the 2nd, 3rd and 4th r.h.s. terms of Equ. 16) and the square of the vorticity of the longterm zonal circulation (the 1st r.h.s. term of Equ. 16).

In order to study the importance of the correlation terms of Equ. 16, for which a qualitative explanation does not seem to exist at the present time as far as the author knows, an expression for the zonal r.m.s. value of $\{\zeta_g\}_{(t)}$ was obtained. This is given by

$$\{\{\zeta_g\}_{(t)}\}_{(\lambda)} = \left[[[\zeta_g]^2_{(t,\lambda)}]_{(t,\lambda)} + [([\zeta_g]_{(t)})^2_{(\lambda)}]_{(t,\lambda)} \right.$$
$$\left. + [([\zeta_g]_{(\lambda)})^2_{(t)}]_{(t,\lambda)} + [(\zeta_g)^2_{(t,\lambda)}]_{(t,\lambda)} \right]^{1/2} \tag{17}$$

The 5th and 6th r.h.s. terms of Equ. 16 drop out in zonal averaging because each involves one component which is a deviation from the zonal mean.

A comparison of Equ. 17 with Equ. 14 shows that

$$\{\{\zeta_g\}_{(t)}\}_{(\lambda)} = [\{\zeta_g\}_{(t)}^2]_{(\lambda)}^{1/2} \tag{18}$$

which serves as a check for the correctness of our previous equations.

In Appendices 8 and 9 we present the values of $\{\{\zeta_g\}_{(t)}\}_{(\lambda)}$ for October 1969 and of $\{\{\zeta_g\}_{(\lambda)}\}_{(t)}$ for all the months considered. A comparison of these values with one another and with the tabulated results of Appendices 1a, 1b and 1c shows that the parameter K is given by

$$K = [\{\zeta_g\}_{(\lambda)}]_{(t)} \doteq [\{\zeta_g\}_{(t)}]_{(\lambda)}$$
$$\doteq \{\zeta_g\}_{(t,\lambda)} \tag{19}$$

whereby it is denoted that

$$\{\zeta_g\}_{(t,\lambda)} = \{\{\zeta_g\}_{(t)}\}_{(\lambda)} \doteq \{\{\zeta_g\}_{(\lambda)}\}_{(t)}$$

$$= \{\zeta_g\}_{(\lambda,t)} \tag{20}$$

Since the values of $\{\zeta_g\}_{(t,\lambda)}$ do not include the effects of any correlation terms, whereas those of $[\{\zeta_g\}_{(t)}]_{(\lambda)}$ do include these, the results of comparing Appendices 1a, 1b, 1c, 8 and 9 are quite encouraging and reveal that correlations such as those represented by the 5th and 6th r.h.s. terms of Equ. 16 are not very important. Hence $\{\zeta_g\}_{(t)}$ could be approximated as follows:

$$\{\zeta_g\}_{(t)} \doteq \left[[[\zeta_g]^2_{(t,\lambda)}]_{(t)} + [([\zeta_g]_{(t)})^2_{(\lambda)}]_{(t)} \right.$$

$$\left. + [([\zeta_g]_{(\lambda)})^2_{(t)}]_{(t)} + [(\zeta_g)^2_{(t,\lambda)}]_{(t)} \right]^{1/2} \tag{21}$$

Thus for all practical purposes $\{\zeta_g\}_{(t)}$ and the parameter K both contain only the square-roots of the squared vorticity of the longterm zonal circulation and the variances of the vorticity deviations from the mean state. Thus they represent the summed (vorticity) effects of the longterm zonal circulation and the deviations from it.

The above equations and remarks show that the parameter K. and $\{\zeta_g\}_{(t)}$ are indeed representatives of the normal state of the atmosphere, especially when inequalities (9) and/or (10) are valid.

Some results obtained by applying these parameters to the geopotential height data of the extratropics of the Northern Hemisphere will be discussed below.

7. <u>The Distributions of K</u>

7A. <u>Properties of the K maxima</u>

We present the distributions of K in the four months considered in

Figures 3a to 3d. A comparison of these with the distributions of

$[\zeta_g]_{(t,\lambda)}$ in Figures 1a to 1d shows that with the exception of January

the values of $[\zeta_g]_{(t,\lambda)}$ and K in each month could be related by

$$\left| [\zeta_g]_{(t,\lambda)} \right| << K \tag{22}$$

Hence the time-and-longitude average of the moduli of eddy vorticity is

much greater than the vorticity of the $[u_g]_{(t,\lambda)}$ distribution in the

troposphere and the lower stratosphere.

As was discussed in Paper A we find the densities of the K isopleths to

be considerably different in the stratosphere and the troposphere. Thus a

stratosphere which extends downward in the poleward direction is revealed

in each month.

The maxima of K must occur at those levels where the isotach maxima

imbedded in jet streams occur most frequently and/or with the largest

magnitudes. These are also latitude belts in which the tropopause break

will occur most frequently (see Paper A). From the studies of the transport

of stratospheric radioactive debris into the troposphere (Reiter et al.,

1967; Mahlman, 1967; and others) it is known that most of this transport

is accomplished in regions of tropopause-break associated with lower

tropospheric fronts. Hence the latitude belts of occurrence of K maxima

are in general the regions most actively receiving stratospheric radio-

active debris. An exception to this is the January maximum, which occurs

in conjunction with the isotach maxima in the STJ-PFJ confluence regions

(see Paper A). Since the STJ does not have a baroclinic or frontal zone extending into the lower troposphere (see, for example, Reiter and Whitney, 1969) the southern part of the K maximum in January does not represent an important region for the radioactive debris transport into the lower troposphere. However, the partitioning of this maximum is difficult because of the day-to-day variability of jet stream location (see Reiter and Whitney, op. cit.)

The author wishes to re-emphasize here the possible significant anomalies of K in the period (1969-70) studied. Such anomalies would make the locations of K maxima given in Figures 3a to 3d non-typical. For true climatological location of these several more years of data would have to be studied. Even then great difficulties in the forecasting of debris transfer will remain because of seasonal anomalies and intra-monthly variability. (For a detailed discussion of the stratospheric-tropospheric exchange processes see Reiter 1972, p. 61 to 102).

7B. The seasonal changes and migrations of extratropical jet streams

The distributions of K in the four months studied enable us to locate the time-and-zonal average positions of the extratropical jet streams approximately.

A comparison of Figures 3a to 3d shows that there is considerable similarity in the distribution of K in the mid-troposphere in all the four months. At the 700 mb level the maximum value of K is reached in January ($K = 2.5 \times 10^{-5} s^{-1}$). But in the other 3 months, at this level, the values of K are not much smaller ($K = 2 \times 10^{-5} s^{-1}$).

But as the altitude increases the pattern of K changes from month to month.

The upper tropospheric distributions of K in July and October have considerable similarity, the maxima of K constituting a single unbroken "roll" from 25N to 75N in each month.

Similarly the upper tropospheric distributions of K in January and April have much similarity. In both these months the maxima of K are bifurcated and exhibit distinct relative minima somewhere in the extratropics.

In JULY the maximum isopleths of K at jet-stream level have the smallest magnitudes of any month studied here. The highest isopleth in Figure 3a $(4.25 \times 10^{-5}s^{-1})$ is quite well spread-out across latitude circles, extending from approximately 38N to 55N. Another feature of the K maximum in this month is the higher altitude at which it occurs compared to the maximum, for example, of October. The Extratropical Frontal Jet Streams of January, April and October have the maximum K isopleth at approximately the 300 mb level and only lower value contours extend to the 250 mb or 200 mb level. Thus the maximum value of K in July occurs at higher altitudes than the maxima (associated with the EFJ) of the other three months. The reason for this must be the poleward migration of the subtropical high pressure systems in summer (see Fig. 2a). This migration tends to raise the tropopause in the midlatitudes in summer. Figure 3 e, which is an analysis of the radiosonde data of some coastal North American stations for July 1969, is presented in support of this statement. (Here the tropopause has been defined to be any isothermal or inversion layer 10 mb or more thick that occurs above the 400 mb level.) More extensive analyses of tropopause heights might be found in the U. S. Dept. of Commerce Daily Aerological Cross Sections (1962-63). The basic reasons for this raising of tropopause heights in summer are

the weakening of the pole to equator temperature gradient and the relative increase of small-scale (Cb) convection in summer (see Gray, 1972).

The change in the maximum observed magnitude of K from July to OCTOBER is as striking as the change in the geographical distribution of $\{\zeta_g\}_{(t)}$ over this period (see Section 8). From an observed minimum in July, the maximum of K rises in October to an absolute maximum of any month studied here: The highest contour drawn in Figure 3b has a value of $5.25 \times 10^{-5} s^{-1}$. This very large value of K which occurs in conjunction with the PFJ is due to the common occurrence of low index type patterns of circulation at the 300 mb level almost every in this month. This leads to the simultaneous occurrence of large shears and large curvatures of streamlines resulting in the very high values of vorticity observed; during the other three months studied large shears were generally observed when the flow was quasi-zonal. In support of these observations we present Figures 6, 7 and 8 which are the geopotential height distributions of the 300 mb surface on Oct. 17, 1969; Oct. 30, 1969; and Apr. 2, 1970 respectively. An example for January 1970 has already been presented in Paper A.

The distribution of K in JANUARY 1970 is presented in Figure 3c. This distribution has already been discussed in detail in Paper A, and the reader is referred to it. The important feature of this diagram is the definite bifurcation of K in the upper troposphere with a maximum in the midlatitudes (approximately 30N to 50N) and another in the subpolar latitudes (60N to 70N) with a relative minimum at 55N. These maxima display the expected characteristics of the STF combined with the PFJ, and AFJ. The maximum value of K in the subtropics (28N to 35N) occurs

at a lower pressure (approximately 200 mb) than the maximum at 40N, which occurs in conjunction with the PFJ at a higher pressure (300 mb). The upward slope of the K isopleths in the equatorward direction in these latitudes in the troposphere is quite significant. From these observations we could infer the following:

1) The midlatitude (30N to 50N) maximum of K in January is largely due to the confluence regions of the STJ and the PFJ (see Krishnamurti, 1961).

2) The K maximum associated with the STJ is confined largely to the upper troposphere whereas the maximum associated with the PFJ extends downward considerably, because of the horizontal wind shears in the polar frontal zone.

3) The time-and-zonal average position of the STJ is at a higher level than that of the PFJ, as is the case with daily meridional cross-sections.

The location of the secondary maximum of K in the subpolar latitudes, which is due to the Arctic Front Jet Stream (see Paper A), leads to a fourth observation:

4) The Arctic Front Jet Stream occurs at a lower altitude than both the STJ and the PFJ. The K maximum associated with this jet stream also extends downward, thus indicating the similarity between the AFJ and the PFJ.

5) Since the maxima of K must occur in zonal belts where the highest wind speeds are most frequently observed[*], these are also

---

[*] That this would lead to the maxima of K is seen from the definition of jet streams: "(A jet stream) is a strong, narrow current, concentrated along a quasi-horizontal axis in the upper troposphere or in the stratosphere, characterized by strong vertical and lateral wind shears..." (WMO, Res. 25 [EC-IX]).

zonal belts in which the phenomenon of tropopause break or folding will be observed most frequently (see Paper A).

Combining observations 3, 4 and 5 we could state the following:

6) Tropopause breaks must in general occur at increasingly lower altitudes (or higher pressures) in the poleward direction. Thus the tropopause itself slopes downward in the poleward direction. The time-and-zonal mean tropopause in the extratropics could probably be represented by a line joining the major axes of the ellipses of K maxima.

It might be seen from Figure 3b that the maximum of K in October 1969 occurred at 50N. This maximum is entirely due to the PFJ since "the Subtropical Jet Stream essentially outlines the poleward limit of the tropical cell of the general circulation" (Riehl, 1962, p. 30) and this limit never seems to be northward of 40 N (see Krishnamurti, 1961; and   Oort and Rasmusson, 1971, p. 23 to 24). Thus the time-and-zonal mean location of the PFJ in October 1969 was approximately 50N, whereas it was (again, approximately) 40N in January 1970. Such a large change is not likely to be anomalous. Hence we add the following remark to those made above, although this has to be verified by several more years of data analysis:

7) The PFJ tends to migrate toward the latitude of the STJ when the latter appears in the extratropical troposphere as the mean meridional circulation of the tropics intensifies in winter.

The distribution of K in APRIL (Figure 3d) has considerable semblance to the distribution of K in January. But the midlatitude maximum of K in the jet stream layer has broadened and extends to almost 65N and the bifurcation of midlatitude and subpolar maxima of K occurs (approximately) over the latitude belt 65N to 70N. The subpolar

maximum again occurs at lower altitudes than the midlatitude maximum but the structure of this maximum is not completely known since our data do not extend beyond 75N.

An important feature of the midlatitude upper tropospheric maximum of K in April 1970 is that the maximum value observed is at 300 mb at 45N and has a magnitude of $4.96 \times 10^{-5} s^{-1}$ as read from our computer output. At the 250 mb level (for which a special analysis was performed for this month) the observed maximum is again at 45N but has a magnitude of $4.8 \times 10^{-5} s^{-1}$. Thus the April maximum of K is entirely due to the PFJ which normally occurs at about the 300 mb level. However, the remnants of the STJ still linger in the atmosphere as might be seen from the distribution of the $4.5 \times 10^{-5} s^{-1}$ isopleth in the latitude belt 35N to 55N, as well as the general upward slope of the K isopleths in the equatorward direction just as in January. The separation of the K maxima associated with the STJ and the PFJ is quite conspicuous in Fig. 3d. Hence we make the following inference:

8) As the Hadley cell begins to weaken in spring the STJ also weakens; and the PFJ migrates poleward and away from the region of occurrence of the STJ. Simultaneously, the AFJ also moves poleward.

From the above, the following statements could be made concerning the time-and-zonal average location of the PFJ:

9) The southernmost location of the PFJ is in winter, and is approximately 40N. In the transitional seasons as well as in summer it occurs at approximately 45N to 50N. In these seasons the relatively broad distribution of the K maxima indicates the significant meanders of the PFJ.

The above observation is completely verified by the geographical distributions of $\{\zeta_g\}_{(t)}$ and $[\zeta_g]_{(t)}$ (see section 8) at the jet-stream

level, from which it is seen that the extratropical land masses are dominated in the transitional seasons by maxima of $\{\zeta_g\}_{(t)}$ which are essentially due to transient eddies. Thus:

10) The observation of synoptic meteorologists that the extratropical cyclones of the transitional seasons are much more intense than those of winter is seen to be valid.

7C. <u>A historical perspective: Some early results of Rossby</u>

The splitting of the Extratropical Frontal Jet Stream and the separate occurrence of Arctic Fronts and Polar Fronts have been known to synoptic meteorologists for a long time. But the interest in the study of the long term zonal circulation $[u]_{(t,\lambda)}$ has attracted meteorologists to study parameters such as $[u]_{(t,\lambda)}$, $[v]_{(t,\lambda)}$, $[w]_{(t,\lambda)}$ etc. The distribution of $[u]_{(t,\lambda)}$ has a single maximum in every calendar month which occurs in the upper troposphere. Peculiarly enough, even the parameter $[\frac{1}{2}(u^2 + v^2)]_{(t,\lambda)}$ which considers the moduli of the horizontal components of the wind tends to have a single maximum in the northern hemisphere troposphere (see Oort and Rasmusson, 1971, p.88-89). These results have led to the assumption that there is only a single zone of concentration of baroclinicity in the atmosphere. The frontal jet streams were assumed to have such large meanders that they would not appear in mean distributions such as that of $[u]_{(t,\lambda)}$.

This is indeed the case. But the distribution of the parameter K clearly brings out the presence of two jet-stream related maxima of monthly normal vorticity in the upper troposphere in winter and spring.

Rossby (1949) was able to obtain these two jet streams in a time-mean (but not zonal-mean) cross-section. He considered the geostrophic

zonal wind distribution in a vertical-meridional cross-section over North America analyzed by Dr. S. L. Hess. This diagram is reproduced here as Fig. 3f. Rossby plotted the data from this diagram at the 12 Km level as a latitude vs. Rossby number diagram, which is reproduced here as Figure 3g. This diagram indicates the presence of two jet stream-related $[u_g]_{(t)}$ maxima in the extratropics. It might be noted that these two maxima coincide with the K maxima at the 200 mb level in January 1970, presented here as Figure 3h.

Rossby (op. cit.) commented as follows on these maxima: "It is of interest to note that the averaging process has not fully erased the sharpness of the jet. There is also some evidence for a second, weaker jet located in about latitude 55^oN. To some extent this second jet may be the statistical result of averaging over a large number of jet positions; but inspection of available upper-level charts suggests that the simultaneous occurrence of two jets is not uncommon."

8. The Geographical Distributions of $[\zeta_g]_{(t)}$ and $\{\zeta_g\}_{(t)}$

We shall consider these two types of distributions together. In Figures 4a to 4d the distributions of $[\zeta_g]_{(t)}$ for the four months considered. are presented and in Figures 5a to 5d those of $\{\zeta_g\}_{(t)}$. All these distri-butions are for the 300 mb level, or approximately the level of the Polar Front Jet Stream. As discussed in section 6 above (see also Paper A) the distributions of $[\zeta_g]_{(t)}$ do not include transient eddies whereas those of $\{\zeta_g\}_{(t)}$ do include them. Thus the difference

$$\{\zeta_g\}_{(t)} - \left| [\zeta_g]_{(t)} \right|$$

is a measure of the time-mean magnitude of the transient eddy vorticity at any given location (ϕ, λ, p).

Hence a simultaneous consideration of the $[\zeta_g]_{(t)}$ and $\{\zeta_g\}_{(t)}$ fields should enhance our knowledge of the relative importance of transient eddies in different regions of the extratropics of the Northern Hemisphere at the level of the PFJ.

JULY (Figures 4a and 5a)

We shall first consider the latitudinal belt 25N to 40N. In this belt the isopleth that occurs most commonly in the $[\zeta_g]_{(t)}$ field is the $2 \times 10^{-5} s^{-1}$ one, with the exception of West Asia and the Mediterranean Sea region.

The values of $\{\zeta_g\}_{(t)}$ in the same region lie between $2.5 \times 10^{-5} s^{-1}$ and $3.5 \times 10^{-5} s^{-1}$. Thus the difference

$$\{\zeta_g\}_{(t)} - \left| [\zeta_g]_{(t)} \right|$$

is small. This is expected in view of the poleward migration of the subtropical high pressure systems in summer, especially over the oceans (see also Figures 2a to 2d), and the resulting reduction in the frequency of occurrence of extratropical cyclones in the latitude belt considered.

In the same latitude belt over West Asia and the Mediterranean the $[\zeta_g]_{(t)}$ isopleth values increase to $4 \times 10^{-5} s^{-1}$ while the isopleths of $\{\zeta_g\}_{(t)}$ have maximum values of $5.5 \times 10^{-5} s^{-1}$ over West Asia and $6.5 \times 10^{-5} s^{-1}$ over parts of Italy, Greece and Turkey. Thus the vorticity contribution by transient eddies is seen to be relatively small in these regions also.

In contrast to these is the region stretching from the Greenwich Meridian to 90W and meridionally extending from 45N to about 65N. Here the values of $[\zeta_g]_{(t)}$ are cyclonic and of an average value of about

$2.5 \times 10^{-5} s^{-1}$ whereas the $\{\zeta_g\}_{(t)}$ values have an approximate mean magnitude of $5 \times 10^{-5} s^{-1}$. Thus the transient eddy vorticity is of the same magnitude as the sum of the standing eddy and $[u_g]_{(t,\lambda)}$ field vorticity components. This is also true of northern USSR, particularly the 60N to 75N belt between 70E and 100E.

OCTOBER (Figures 4b and 5b)

The changes in the field of $\{\zeta_g\}_{(t)}$ from July to October are quite striking. The vorticity field intensifies very significantly during this period, especially over the middle latitudes. Whereas the July midlatitude maximum of $\{\zeta_g\}_{(t)}$ is over the north Atlantic, the October maxima seem to be very pronounced over land. Thus the maximum at 110W, 40N (over Utah in the USA) has a value in excess of $8 \times 10^{-5} s^{-1}$; over a large portion of the Hudson Bay the values of $\{\zeta_g\}_{(t)}$ exceed $6 \times 10^{-5} s^{-1}$; just east of the Urals a maximum of nearly $8 \times 10^{-5} s^{-1}$ is seen; and just west of the Sea of Japan, over the People's Republic of China, there is another maximum of value $7 \times 10^{-5} s^{-1}$. In contrast to these the only pronounced maximum over the Oceans (the Aleutian Low) is located over the northern Pacific and reaches a maximum value of nearly $8 \times 10^{-5} s^{-1}$. The values of $[\zeta_g]_{(t)}$ in these regions are observed to be rather small, ranging from $2 \times 10^{-5} s^{-1}$ to $4 \times 10^{-5} s^{-1}$, the sole exception being the North Pacific region where $[\zeta_g]_{(t)}$ values reach a maximum of nearly $6 \times 10^{-5} s^{-1}$. Thus almost all of the important maxima of $\{\zeta_g\}_{(t)}$ over land are due to transient eddies whereas the maximum over the Pacific owes itself to the vorticity of the standing eddies since that of $[u_g]_{(t,\lambda)}$ is quite small (see Figure 1b). This is probably due to the steadiness of the PFJ in this region.

Figures 6 and 7 might be considered in this connection. They are distributions of geopotential height at the 300 mb level on 17 October 1969 and 30 October 1969 respectively. These patterns are rather typical of the daily 300 mb height fields in this month. The height fields on the two days presented here are seen to be typical of low index type circulation and the jet stream systems are northward of 30 N. These Figures had been discussed further above (see section 7).

Another important feature of Figure 4b is the cyclonic vorticity observed over northern India. In July the observed time-mean vorticity is anticyclonic (see Figure 4a), and provides ventilation for the air converging into the monsoonal trough below. With the retreat of the southwest monsoon upper-level cyclonic conditions are seen to be re-established. The remnants of the summer anticyclone over Tibet are, however, still observed in October. From Figures 4b and 5b it is seen that one half or more of the temporal r.m.s. vorticity over northern India is due to transient eddies.

APRIL (Figures 4d and 5d)

This spring month has characteristics which could be identified with one or the other of the three other months considered.

The remnants of the 3 wave pattern of January are still discernible: In the field of $[\zeta_g]_{(t)}$ the maximum over southern Asia and the Mediterranean has disappeared. However, the lows over the east coasts of Asia and North America are still present -- with significant magnitudes: Over both the Atlantic and the Pacific the maxima exceed $5 \times 10^{-5} s^{-1}$ -- but are displaced into the oceanic regions.

Over northern India the intense cyclonic vorticity ($[\zeta_g]_{(t)} > 3 \times 10^{-5} s^{-1}$) of January has been replaced by near-neutral ($[\zeta_g]_{(t)} \approx 0.7 \times 10^{-5} s^{-1}$ at 80E, 35N) conditions, and the very beginnings of the summer anticyclone over Tibet are

visible (the area covered is very small and the intensity slightly in excess of $-2 \times 10^{-5} s^{-1}$). Other features of the July distribution of $[\zeta_g]_{(t)}$ are also present: For example, the subtropical high pressure system has moved quite northward over the Pacific, off the North American coast.

Despite all these, April seems to resemble October most, especially in the continental distribution of $[\zeta_g]_{(t)}$ and $\{\zeta_g\}_{(t)}$. Extremely large values of $\{\zeta_g\}_{(t)}$ are observed over land: Over California the $\{\zeta_g\}_{(t)}$ maximum has a value in excess of $7 \times 10^{-5} s^{-1}$; in the vicinity of the Great Lakes the highest isopleth observed is $6 \times 10^{-5} s^{-1}$; over Greenland the maximum exceeds $7 \times 10^{-5} s^{-1}$; over the Mediterranean Sea and Europe the maxima exceed $5 \times 10^{-5} s^{-1}$; and near Japan there is a maximum of value $5 \times 10^{-5} s^{-1}$. One feature that distinguishes these maxima is the observed values of $[\zeta_g]_{(t)}$ in these regions, which range from zero to $2 \times 10^{-5} s^{-1}$. Thus all of the $\{\zeta_g\}_{(t)}$ maxima over land are due to transient eddies. This might be contrasted against the constitution of the oceanic maxima mentioned above. The maximum value of $\{\zeta_g\}_{(t)}$ for the Atlantic "low" (off Newfoundland) is $6.8 \times 10^{-5} s^{-1}$ and the maximum value of $[\zeta_g]_{(t)}$ in the same location is $5.3 \times 10^{-5} s^{-1}$; similarly the highest value of $\{\zeta_g\}_{(t)}$ south of Kamchatka is nearly $8 \times 10^{-5} s^{-1}$ and the maximum value of $[\zeta_g]_{(t)}$ here is $5.5 \times 10^{-5} s^{-1}$. Thus both of the oceanic maxima of $\{\zeta_g\}_{(t)}$ seem to owe their existence to standing eddies (the contribution by the distribution of $[\zeta_g]_{(t,\lambda)}$ being very small as seen from Figure 1d).

Thus the maxima of $\{\zeta_g\}_{(t)}$ over land and ocean have distinctly different amounts of contribution by standing eddies and transient eddies, the differences between the two types being the same in October and April.

JANUARY (Figures 4c and 5c)

These have already been discussed in Paper A. Here we shall merely summarize the conclusions made there, and relate them to the observed features of the $[\zeta_g]_{(t)}$ and $\{\zeta_g\}_{(t)}$ distributions of the other 3 months studied.

One outstanding feature of the January distribution of $[\zeta_g]_{(t)}$ is the very intense 3 wave pattern that dominates the middle latitudes. The cyclonic vorticity maxima imbedded in this 3 wave pattern have a quasi-zonal distribution and are very sharply cutoff inland. The absolute maxima of $[\zeta_g]_{(t)}$ and especially of $\{\zeta_g\}_{(t)}$ tend to occur exactly over the coasts of Asia and North America, in the case of the oceanic extrema. The maximum $[\zeta_g]_{(t)}$ over southern Asia has a single extremal isopleth of value 5 x 10^{-5} s^{-1} over India; but when the transient eddy contributions of vorticity are added to this distribution two extremal isopleths each of value 5 x $10^{-5} s^{-1}$ appear over India and the Mediterranean, as seen from the $\{\zeta_g\}_{(t)}$ distribution of Figure 5c.

A comparison of Figures 4c and 5c shows that both the oceanic maxima of $\{\zeta_g\}_{(t)}$ are composed largely of stationary eddies and the vorticity of the long term zonal circulation. The latter is of significance only in January and then only in the midlatitudes (see Fig. 1c). The maximum of $\{\zeta_g\}_{(t)}$ over India is also composed essentially of these constituents. But the maxima of $\{\zeta_g\}_{(t)}$ over the Mediterranean, Scandinavia and northern USSR are all composed largely of transient eddies. If all these three $\{\zeta_g\}_{(t)}$ maxima were considered to be inland maxima and the maximum over India considered as a non-typical inland maximum, then the following generalization could be made concerning the componental contribution to the $\{\zeta_g\}_{(t)}$ maxima:

Except in summer all the oceanic maxima of $\{\zeta_g\}_{(t)}$ are essentially

due to the vorticity of the standing eddies and of $[\zeta_g]_{(t,\lambda)}$; and all the

inland maxima are essentially due to the vorticity of the transient eddies.

The reverse is true in summer. Hence the observed componental constitution

of $\{\zeta_g\}_{(t)}$ maxima is not due to variations in the density of the radio-

sonde network system over oceans and land masses.

The above remarks lead to the conclusion that in general the normal

(or temporal r.m.s.) vorticity of the jet-stream level winds over land

are no smaller than that observed over the oceans. However, the contin-

ental maxima of normal vorticity are generally not observed in conventional

climatological maps for the simple reasons that these are arithmetic

averages which eliminate the transient eddies, and that the continental

maxima of normal vorticity are composed largely of transient eddies.

Surely, then, our knowledge of the earth's climate is increased by a

study of the temporal r.m.s. values of parameters such as vorticity.

9. Conclusions and Recommendations

Northern hemisphere geopotential height distributions of the 700 mb;

500 mb; 400 mb; 300 mb; 200 mb; and 100 mb surfaces in four months typical

of the four seasons of the year have been used in a study of the geostrophic

relative vorticity (ζ_g) distribution in the lower atmosphere.

The temporal arithmetic mean of ζ_g is immediately seen to be superior

to the time-mean geopotential height in depicting *some* deviations from the

mean zonal flow. (For the 500 mb monthly-mean geopotential height fields

in January and July and a discussion of these please see Palmen and Newton,

1969, p. 67-69.)

However, only the temporal r.m.s. fields of ζ_g are capable of por-

traying *all* of the deviations from the zonal-mean flow. This is due

to the reasons that the time-mean fields do not include transient eddies,

and that the *continental maxima* of monthly-normal (or r.m.s.) vorticity are constituted largely of transient eddies in the transitional seasons and winter. (In July *oceanic maxima* are thus constituted.)

Thus a full understanding of the eddy distributions in the atmosphere would not be obtained with the help of time-mean charts alone.

It is recommended that future climatological atlases include the temporal r.m.s. fields of parameters -- such as vorticity -- which are capable of describing the temporal normal eddy fields in the different seasons.

The zonal average of the temporal r.m.s. values of ζ_g -- the parameter K -- is shown to be a parameter which could be used to locate the zones in which the different extratropical jet streams are most commonly (or least commonly, as the case may be) observed.

The distributions of K in the four months studied indicate: 1) that there are at least three jet streams in the extratropical troposphere in January and April, 2) that there is probably only one jet stream in the extratropical troposphere in July and October, 3) that the PFJ moves toward the latitude of occurrence of the STJ when the latter appears in the winter atmosphere in conjunction with the intensification of the Hadley Cell, 4) that the PFJ moves poleward and away from the STJ when the latter weakens in spring and 5) that, as a consequence, the highest values of K in the upper troposphere over the latitude belt 45N to 55N are observed in the months of April and October.

REFERENCES

Gray, William M., 1972. Cumulus Convection and Larger-scale Circulations, Part III: Broadscale and Mesoscale Considerations. Atmospheric Science Paper No. 190, Dept. of Atmospheric Science, Colorado State University, Fort Collins, Colorado, 80pp.

Krishnamurti, Tiruvalem N., 1961. The Subtropical Jet Stream of Winter, J. Meteorol., 18:172-191.

Lorenz, Edward N., 1967. The Nature and Theory of the General Circulation of the Atmosphere, World Meteorological Organization, No. 218. TP. 115, 161pp.

Mahlman, J. D., 1967. Further Studies on Atmospheric General Circulation and Transport of Radioactive Debris, Atmospheric Science Paper No. 110, Dept. of Atmospheric Science, Colorado State University, Fort Collins, Colorado, 68 pp.

Oort, Abraham H., and Eugene M. Rasmusson, 1971. Atmospheric Circulation Statistics, NOAA Professional Paper 5, (U. S. Govt. Printing Office, Washington, D. C. Stock Number 0317-0045). 323 pp.

Palmen, E., and C. W. Newton, 1969. Atmospheric Circulation Systems: Their Structure and Physical Interpretation, Academic Press, New York and London, 603 pp.

Reiter, Elmar R., 1969a. Mean and Eddy Motions in the Atmohphere. Mon. Wea. Rev., 97:200-204.

Reiter, Elmar R., 1969b. Atmospheric Transport Processes, Part 1: Energy Transfers and Transformations. TID-24868, U. S. Atomic Energy Commission, Division of technical Information Extension, Oak Ridge, Tenn. 253 pp.

Reiter, Elmar R., 1972. Atmospheric Transport Processes, Part 3: Hydrodynamic Tracers. TID-25731, U. S. Atomic Energy Commission, Division of Technical Information Extension, Oak Ridge, Tenn. 212 pp.

Reiter, Elmar R., M. E. Glasser, and J. D. Mahlman, 1967. The Role of the Tropopause in Stratospheric-Tropospheric Exchange Processes. Atmospheric Science Paper No. 107, Dept. of Atmospheric Science, Colorado State University, Fort Collins, Colo., 60 pp.

Reiter, Elmar R., and L. F. Whitney, 1969. Interaction Between Subtropical and Polar-Front Jet Stream. Mon. Wea. Rev., 97:432-438.

Riehl, Herbert, 1962. Jet Streams of the Atmosphere, Technical Report No. 32, Dept. of Atmospheric Science, Colorado State University, Fort Collins, Colo., 117 pp.

Rossby, Carl-Gustaf, 1949. On the Nature of the General Circulation
     of the Lower Atmosphere, Chapter II, p. 16-48 *in the* Atmospheres
     of the Earth and Planets (Kuiper, Ed.) The University of Chicago
     Press, 366 pp.

Srivatsangam, Srinivasan, 1973. A Contribution to the Synoptic
     Climatology of the Extratropics. Atmospheric Science Paper No. 203,
     Dept. of Atmospheric Science, Colorado State University,
     Fort Collins, Colo., 34 pp.

U. S. Dept. of Commerce, 1962-63. Daily Aerological Cross Sections:
     Pole to Pole along Meridian 75°W for the IGY Period (July 1957 to
     Dec. 1958). For sale by the Superintendent of Documents, U. S.
     Govt. Printing Office, Washington, D. C. Price (each month) $1.75.

APPENDIX 1a

$[\{\tau_g\}_{(\lambda)}]_{(t)}$ and $[\{\tau_g\}_{(t)}]_{(\lambda)}$ for July 1969

Units: $10^{-7}s^{-1}$

(For an explanation of symbols see Table 1)

$[\{\tau_g\}_{(\lambda)}]_{(t)}$

PRES mb	25N	30N	35N	40N	45N	50N	·55N	60N	65N	70N	75N
700	148	143	155	145	165	195	195	201	189	172	184
500	177	174	211	213	236	270	267	270	255	248	249
400	199	217	257	274	300	334	324	330	310	307.	302
300	239	283	333	372	401	425	402	405	377	373	358
200	297	343	387	438	430	423	349	313	262	242	227
100-	234	217	207	165	152	139	121	103	88	74	78

$[\{\tau_g\}_{(t)}]_{(\lambda)}$

PRES mb	25N	30N	35N	40N	45N	50N	55N	60N	65N	70N	75N
700	144	·140	151	146	167	191	188	200	190	175	192
500	174	173	206	213	238	266	261	271	258	251	261
400	195	214	253	273	302	326	318	332	313	311	314
300	235	280	326	371	401	415	395	411	382	376	372
200	291	340	379	439	431	421	345	319	263	248	238
100	212	210	195	167	151	140	117	103	90	81	81

APPENDIX 1b

Same as Appendix 1a But for October 1969

$[\{\tau_g\}_{(\lambda)}]_{(t)}$

PRES mb	25N	30N	35N	40N	45N	50N	55N	60N	65N	70N	75N
700	162	175	179	193	229	259	-243	227	195	179	189
500	204	237	263	289	349	372	343	319	274	255	257
400	238	288	318	361	437	463	428	391	341	313	308
300	277	357	386	433	522	558	502	457	402	373	360
200	313	387	418	442	492	482	402	356	309	277	261
100	228	215	212	189	202	193	177	166	159	149	142

$[\{\tau_g\}_{(t)}]_{(\lambda)}$

PRES mb	25N	30N	35N	40N	45N	50N	55N	60N	65N	70N	75N
700	157	167	177	186	219	251	235	220	192	178	186
500	199	227	259	280	338	364	335	315	277	254	261
400	235	278	309	351	420	454	419	386	346	315	313
300	275	347	375	423	504	549	494	453	408	375	364
200	311	377	408	432	474	474	395	351	312	279	264
100	223	209	208	185	195	191	173	163	159	152	146

APPENDIX 1c

Same as Appendix 1a But for April 1970

$$[\{\tau_g\}_{(\lambda)}]_{(t)}$$

PRES mb	25N	30N	35N	40N	45N	50N	55N	60N	65N	70N	75N
700	157	176	165	194	240	253	226	198	182	169	206
500	218	247	284	284	351	344	306	286	267	262	320
400	270	310	353	363	434	419	376	350	326	322	376
300	332	385	430	444	510	488	426	393	352	343	364
200	368	423	453	439	441	388	301	266	224	222	229
100	236	214	206	202	182	170	143	118	112	123	136

$$[\{\tau_g\}_{(t)}]_{(\lambda)}$$

PRES mb	25N	30N	35N	40N	45N	50N	55N	60N	65N	70N	75N
700	152	172	183	190	229	246	223	196	177	164	205
500	213	244	281	281	338	338	302	281	260	258	312
400	266	306	349	358	421	413	372	344	319	317	367
300	327	381	427	440	496	483	425	388	346	337	355
200	363	420	451	435	427	380	298	262	219	215	222
100	233	209	204	198	174	164	140	115	108	116	132

APPENDIX 2

$[H]_{(t,\lambda)}$ for the 4 Months analyzed. Units: Geopotential Meters.

JULY 1969

LAT	700 MB	500 MB	300 MB	200 MB	100 MB
0 N	3147.7	5852.7	9665.0	12396.0	16562.0
5 N	3176.0	5885.5	9694.5	12438.5	16608.5
10 N	3155.0	5878.0	9706.7	12455.3	16643.6
15 N	3145.7	5864.6	9691.7	12421.7	16633.1
20 N	3160.5	5892.7	9703.8	12436.1	16629.7
25 N	3170.8	5899.2	9710.9	12450.5	16666.0
30 N	3176.2	5898.9	9710.7	12453.6	16691.4
35 N	3172.1	5885.1	9681.7	12420.8	16691.9
40 N	3153.2	5843.1	9604.9	12330.9	16659.5
45 N	3119.6	5782.6	9503.3	12204.9	16606.5
50 N	3079.7	57.8.6	9401.0	12081.1	16551.9
55 N	3042.7	5661.6	9315.3	11987.2	16507.7
60 N	3011.0	5612.0	9239.2	11910.3	16478.3
65 N	2994.4	5582.3	9190.6	11863.7	16461.4
70 N	2978.2	5557.4	9156.7	11831.2	16449.5
75 N	2951.4	5518.6	9105.1	11791.6	16436.4
80 N	2916.0	5463.8	9031.7	11739.8	16419.3
AVG HGT	3091.2	5752.7	9477.2	12189.0	16570.4

OCTOBER 1969

LAT	700 MB	500 MB	300 MB	200 MB	100 MB
0 N	3137.3	5845.7	9662.0	12400.3	16510.0
5 N	3161.0	5880.0	9704.0	12452.0	16639.0
10 N	3149.4	5864.4	9688.3	-12430.6	16625.6
15 N	3153.5	5868.6	9688.5	12428.3	16598.6
20 N	3153.4	5870.3	9663.7	12377.5	16547.1
25 N	3152.6	5857.5	9632.6	12338.7	16530.2
30 N	3142.1	5827.1	9570.5	12264.3	16492.4
35 N	3119.7	5777.5	9481.3	12153.9	16427.8
40 N	3083.4	5704.6	9364.2	12017.0	16339.3
45 N	3029.9	5610.8	9223.1	11862.4	16237.3
50 N	2971.9	5520.8	9085.5	11716.3	16138.9
55 N	2923.4	5446.6	8973.3	11596.9	16050.9
60 N	2884.1	5385.6	8882.9	11498.5	15970.6
65 N	2856.8	5342.8	8820.0	11425.7	15898.2
70 N	2829.4	5297.7	8755.3	11355.1	15831.8
75 N	2801.7	5250.4	8684.9	11286.2	15771.7
80 N	2784.9	5218.8	8635.2	11237.8	15724.7
AVG HGT	3019.7	5621.7	9265.6	11931.9	16254.9

APRIL 1970

LAT	700 MB	500 MB	300 MB	200 MB	100 MB
0 N	3144.7	5862.7	9693.7	12452.7	16589.0
5 N	3170.0	5900.0	9751.3	12469.0	16766.3
10 N	3159.0	5887.7	9728.5	12491.2	16694.5
15 N	3163.2	5879.8	9694.5	12436.5	16632.0
20 N	3163.7	5875.7	9654.4	12356.4	16566.0
25 N	3155.4	5847.4	9595.5	12281.8	16495.1
30 N	3131.4	5793.3	9497.6	12164.3	16419.7
35 N	3100.2	5723.6	9376.3	12015.4	16323.9
40 N	3056.2	5640.4	9239.5	11859.2	16223.6
45 N	2998.2	5545.3	9098.8	11711.9	16126.4
50 N	2945.8	5463.2	8979.3	11588.7	16041.2
55 N	2904.8	5398.0	8882.9	11491.2	15970.3
60 N	2868.3	5338.3	8794.8	11408.9	15912.2
65 N	2837.4	5285.6	8717.9	11338.4	15861.9
70 N	2809.9	5227.2	8632.9	11266.7	15814.3
75 N	2791.3	5178.1	8559.6	11205.1	15772.6
80 N	2784.6	5158.1	8521.9	11168.0	15743.5
AVG HGT	3010.8	5588.5	9201.1	11865.0	16232.5

JANUARY 1970

LAT	700 MB	500 MB	300 MB	200 MB	100 MB
0 N	3145.7	5857.7	9674.7	12407.7	16536.0
5 N	3166.7	5886.3	9710.7	12456.3	16662.3
10 N	3156.3	5872.4	9692.1	12426.7	16625.4
15 N	3156.5	5866.4	9669.0	12391.2	16578.0
20 N	3152.5	5843.0	9603.4	12303.0	16497.6
25 N	3125.4	5783.9	9503.8	12188.2	16414.9
30 N	3077.1	5693.0	9347.5	12004.5	16284.9
35 N	3015.5	5582.7	9163.1	11778.4	16126.5
40 N	2949.2	5469.4	8984.6	11576.7	15972.6
45 N	2891.3	5377.3	8847.6	11427.8	15840.8
50 N	2852.4	5315.9	8757.4	11324.1	15734.4
55 N	2825.5	5270.0	8688.3	11249.1	15656.2
60 N	2802.9	5227.6	8629.0	11193.2	15601.9
65 N	2796.9	5204.4	8594.3	11161.7	15571.4
70 N	2797.6	5193.8	8571.8	11141.3	15561.2
75 N	2794.6	5182.5	8552.5	11127.3	15565.8
80 N	2781.6	5157.7	8526.5	11112.6	15576.2
AVG HGT	2969.9	5516.7	9089.2	11721.8	16047.4

APPENDIX 3

$[u_g]_{(t,\lambda)}$ Calculated from $[\Pi]_{(t,\lambda)}$ in Appendix 2

Units: ms^{-1}

JULY 1969
DEG. LAT. NORTH

PRES mb	17.5	22.5	27.5	32.5	37.5	42.5	47.5	52.5	57.5	62.5	67.5	72.5	77.5
700	-6.0	-3.3	-1.4	.9	3.8	6.0	6.5	5.6	4.5	2.3	2.1	3.4	4.4
500	-11.3	-2.1	.1	3.1	8.3	10.8	10.5	8.7	7.1	4.1	3.3	4.9	6.8
300	-4.9	-2.2	.1	6.5	15.3	18.2	16.8	13.1	10.9	6.6	4.4	6.5	9.1
200	-5.8	-4.6	-.8	7.4	17.9	22.6	20.3	14.3	11.0	6.4	4.3	5.0	6.4
100	1.4	-11.5	-6.7	-.1	6.4	9.5	9.0	6.7	4.2	2.3	1.6	1.7	2.1

OCTOBER 1969
DEG. LAT. NORTH

PRES mb	17.5N	22.5N	27.5N	32.5N	37.5N	42.5N	47.5N	52.5N	57.5N	62.5N	67.5N	72.5N	77.5N
700	.0	.3	2.8	5.0	7.2	9.6	9.5	7.4	5.6	3.7	3.6	3.5	2.1
500	-.7	4.0	8.0	11.2	14.5	16.8	14.8	11.3	8.7	5.8	5.9	6.0	3.9
300	10.0	9.8	16.3	20.1	23.3	25.3	22.6	17.1	13.0	8.6	8.5	8.9	6.2
200	20.4	12.3	19.5	24.9	27.2	27.7	24.0	18.2	14.1	9.9	9.2	8.7	6.0
100	20.7	5.3	9.9	14.5	17.6	18.3	16.1	13.4	11.5	9.9	8.7	7.6	5.8

JANUARY 1970
DEG. LAT. NORTH

PRES mb	17.5N	22.5N	27.5N	32.5N	37.5N	42.5N	47.5N	52.5N	57.5N	62.5N	67.5N	72.5N	77.5N
700	1.6	8.6	12.7	13.9	13.2	10.4	6.4	4.1	3.2	.8	-.1	.4	1.6
500	9.4	18.7	23.8	24.8	22.5	16.5	10.1	7.0	6.1	3.2	1.4	1.4	3.1
300	26.4	31.5	40.9	41.5	35.5	24.5	14.8	10.5	8.5	4.7	2.9	2.4	3.2
200	35.5	36.3	48.1	50.9	40.1	26.7	17.0	11.4	8.0	4.3	2.7	1.8	1.8
100	32.3	26.1	34.1	35.7	30.6	23.6	17.5	11.9	7.8	4.2	1.3	-.6	-1.3

APRIL 1970
DEG. LAT. NORTH

PRES mb	17.5	22.5	27.5	32.5	37.5	42.5	47.5	52.5	57.5	62.5	67.5	72.5	77.5
700	-.2	2.6	6.3	7.0	8.7	10.4	8.6	6.3	5.2	4.2	3.6	2.4	.8
500	1.6	8.9	14.2	15.7	16.5	17.0	13.5	9.9	8.6	7.2	7.6	6.2	2.5
300	16.1	18.6	25.6	27.3	27.2	25.2	19.6	14.7	12.6	10.5	11.1	9.3	4.7
200	32.2	23.6	30.8	33.5	31.0	26.4	20.2	14.9	11.8	9.6	9.4	7.8	4.6
100	26.6	22.4	19.8	21.6	19.9	17.4	14.0	10.8	8.3	6.9	6.2	5.3	3.6

APPENDIX 4

$[t_g]_{(t,\lambda)}$ Calculated from the $[u_g]_{(t,\lambda)}$ values of Appendix 3.

Units: $10^{-7}s^{-1}$

JULY 1969

PRES mb	20N	25N	30N	35N	40N	45N	50N	55N	60N	65N	70N	75N
700	-51.2	-34.9	-42.3	-48.4	-34.3	.3	27.7	31.1	50.4	9.9	-11.1	5.0
500	-170.3	-39.1	-53.1	-88.0	-32.1	22.7	50.5	46.1	70.3	26.5	-12.3	.7
300	-49.3	-42.2	-113.6	-145.2	-30.7	52.8	94.8	65.6	101.0	58.0	-14.2	-.1
200	-25.3	-69.3	-144.6	-174.8	-57.9	74.1	140.3	87.6	107.8	55.7	6.2	8.4
100	228.3	-93.4	-120.8	-114.5	-44.4	24.0	54.6	57.7	43.3	19.9	5.1	2.8

OCTOBER 1969

PRES mb	20N	25N	30N	35N	40N	45N	50N	55N	60N	65N	70N	75N
700	-3.7	-43.9	-37.7	-32.3	-31.5	16.1	54.0	46.3	47.2	14.7	16.6	42.2
500	-84.2	-66.1	-49.0	-45.7	-21.0	61.3	86.6	68.7	72.3	18.5	24.0	66.6
300	8.3	-106.3	-52.2	-33.5	-4.0	85.9	135.6	108.3	108.3	30.6	29.3	94.1
200	156.4	-118.5	-76.5	-13.7	27.5	107.3	143.2	109.9	108.0	44.6	47.9	92.5
100	284.2	-76.5	-72.5	-37.1	11.4	65.2	76.7	62.2	58.7	52.5	54.5	71.8

JANUARY 1970

PRES mb	20N	25N	30N	35N	40N	45N	50N	55N	60N	65N	70N	75N
700	-122.3	-65.8	-9.9	27.4	66.0	84.9	50.9	23.7	49.1	17.6	-7.9	-16.3
500	-158.8	-76.8	3.7	67.8	134.1	136.4	71.3	31.2	65.1	39.6	5.3	-16.3
300	-75.2	-143.9	27.1	151.2	236.5	206.1	100.4	57.9	85.9	45.1	20.6	2.7
200	6.0	-182.2	-5.1	244.9	285.5	208.0	127.0	83.3	83.7	41.0	25.7	9.7
100	128.4	-120.5	2.7	127.9	161.4	142.8	127.1	96.5	81.6	60.1	36.2	7.2

APRIL 1970

PRES mb	20N	25N	30N	35N	40N	45N	50N	55N	60N	65N	70N	75N
700	-50.2	-62.7	-7.2	-22.3	-17.0	47.1	56.1	31.2	31.2	24.2	35.2	36.9
500	-128.3	-85.6	-13.8	2.6	13.2	88.0	85.4	45.6	46.2	16.7	55.5	93.0
300	-34.8	-110.3	-5.9	32.2	70.3	135.7	120.4	67.8	70.1	24.8	77.0	124.2
200	171.5	-109.7	-20.2	50.2	121.8	147.5	129.1	85.0	68.5	36.1	65.4	94.2
100	88.5	63.3	-14.0	52.3	70.1	86.3	80.2	66.1	47.2	33.3	41.8	56.4

APPENDIX 5

$[u_g]_{(t,\lambda)}$ Calculated from the 5-year Mean Values of $[H]_{(t,\lambda)}$ Presented by Oort and Rasmusson (1971, p. 84). Units: ms^{-1}.

JULY

DEG. LAT. NORTH

PRES mb	17.5	22.5	27.5	32.5	37.5	42.5	47.5	52.5	57.5	62.6	67.5	72.5
700	1.2	-1.3	-3.1	.7	5.2	6.8	6.1	4.6	3.0	1.9	2.1	2.4
500	-2.4	-2.2	-1.3	3.6	8.9	11.1	10.2	7.3	5.2	3.7	3.7	4.1
300	-6.4	-4.1	1.3	8.8	15.5	18.1	16.1	11.6	8.2	6.3	6.2	6.6
200	-8.4	-5.7	1.6	10.1	18.3	21.8	19.0	12.8	8.7	5.7	5.1	5.7
100	-14.9	-12.0	-5.0	1.1	5.4	7.5	9.2	6.3	4.2	1.0	.8	1.8

OCTOBER

DEG. LAT. NORTH

PRES mb	17.5	22.5	27.5	32.5	37.5	42.5	47.5	52.5	57.5	62.6	67.5	72.5
700	-1.6	.3	1.8	4.5	7.0	8.8	9.5	8.7	6.7	4.8	3.7	2.7
500	-1.2	3.5	7.6	10.1	12.9	14.9	14.8	13.1	10.3	7.6	6.3	4.7
300	-.8	7.9	16.0	22.1	23.3	22.2	21.3	18.8	14.9	11.2	9.3	7.9
200	.8	8.9	19.6	27.9	28.6	25.1	22.5	19.5	15.8	11.7	10.1	8.5
100	-5.2	-.3	10.5	18.2	19.1	16.1	15.8	14.8	13.2	10.0	9.8	9.3

JANUARY

DEG. LAT. NORTH

PRES mb	17.5	22.5	27.5	32.5	37.5	42.5	47.5	52.5	57.5	62.6	67.5	72.5
700	4.4	7.9	8.6	9.9	10.9	10.0	8.2	5.9	4.3	3.0	2.4	2.0
500	10.5	17.4	19.1	19.8	19.7	16.5	12.1	8.7	6.7	5.7	4.7	4.1
300	18.5	32.6	37.5	35.8	31.4	24.4	17.6	12.5	9.2	7.8	7.2	6.3
200	22.1	37.3	45.3	44.8	36.8	26.3	19.4	14.6	11.2	9.8	9.0	7.0
100	12.1	23.7	31.2	32.6	28.6	21.7	18.0	14.5	14.8	10.9	10.7	12.3

APRIL

DEG. LAT. NORTH

PRES mb	17.5	22.5	27.5	32.5	37.5	42.5	47.5	52.5	57.5	62.6	67.5	72.5
700	2.0	4.4	5.8	7.9	8.9	8.4	6.9	5.6	4.9	4.1	3.3	2.3
500	5.2	9.8	12.6	16.2	16.7	14.1	11.2	9.1	8.2	7.2	6.0	4.7
300	14.5	21.2	25.4	26.8	25.4	21.3	16.9	14.0	12.3	10.8	9.0	6.6
200	18.9	26.9	33.3	34.2	28.8	21.8	16.9	13.7	12.0	10.0	8.2	5.8
100	11.3	15.2	20.7	23.2	19.1	13.3	10.5	9.0	8.9	7.5	6.3	4.6

APPENDIX 6

$[\zeta_g]_{(t,\lambda)}$ Calculated for the 5-year Mean Oort and Rasmusson (1971) Data. Units: 10^{-7}s^{-1}

JULY
DEG. LAT. NORTH

PRES mb	20	25	30	35	40	45	50	55	60	65	70
700	44.5	32.2	-69.9	-77.6	-21.6	23.3	36.9	36.6	26.5	3.4	4.0
500	-4.9	-17.5	-87.4	-89.2	-25.7	33.4	67.7	52.8	38.7	12.7	9.6
300	-44.9	-98.6	-129.9	-107.6	-24.4	62.9	106.7	83.6	53.9	23.1	19.5
200	-53.7	-132.2	-148.8	-131.1	-37.7	82.7	141.8	97.2	74.1	29.4	12.5
100	-59.4	-132.9	-111.6	-72.8	-30.3	-16.9	67.3	49.3	64.6	6.0	-12.3

OCTOBER
DEG. LAT. NORTH

PRES mb	20	25	30	35	40	45	50	55	60	65	70
700	-35.0	-26.5	-45.2	-37.8	-22.4	1.0	31.9	52.4	51.1	34.1	31.7
500	-83.7	-70.1	-37.6	-37.5	-16.7	25.0	55.8	76.4	72.8	47.8	52.3
300	-154.7	-136.7	-92.3	3.6	48.8	49.9	83.9	106.8	102.7	68.4	62.8
200	-142.1	-184.0	-127.3	18.5	99.2	83.9	92.6	106.9	110.3	66.3	68.6
100	-90.0	-190.6	-126.6	5.4	76.5	31.6	45.9	60.1	89.8	35.7	51.2

JANUARY
DEG. LAT. NORTH

PRES mb	20	25	30	35	40	45	50	55	60	65	70
700	-59.1	-7.3	-14.3	-7.0	30.0	47.1	53.9	41.1	33.4	20.6	15.4
500	-116.7	-17.9	5.3	24.2	81.4	100.4	81.6	52.4	35.2	35.8	30.7
300	-238.4	-62.7	63.2	116.2	163.5	155.2	119.1	84.1	48.4	35.5	44.7
200	-256.2	-114.2	50.2	189.6	229.5	161.2	116.8	91.1	53.2	45.9	71.6
100	-199.3	-114.3	2.5	106.2	158.2	96.3	94.6	27.6	104.5	39.6	21.5

APRIL
DEG. LAT. NORTH

PRES mb	20	25	30	35	40	45	50	55	60	65	70
700	-41.6	-20.4	-31.9	-9.9	20.9	39.5	34.2	25.6	26.3	27.1	29.8
500	-78.0	-41.8	-52.4	9.4	66.2	73.7	55.2	36.9	38.0	44.0	47.0
300	-110.4	-59.1	-1.2	53.1	105.1	109.3	80.6	60.0	59.5	64.6	77.6
200	-130.3	-93.2	13.5	132.0	158.8	119.4	85.8	59.0	67.6	61.4	73.8
100	-62.8	-86.3	-25.0	97.3	126.2	68.1	45.3	21.9	47.3	45.1	54.3

APPENDIX 7

$[\zeta]_{(t,\lambda)}$ Calculated from the $\text{-}[u]_{(t,\lambda)}$ Data of Oort and Rasmusson (1971, p. 76-77). Units: $10^{-7}s^{-1}$.

JULY

PRES mb	20N	25N	30N	35N	40N	45N	50N	55N	60N	65N	70N
700	- 15	- 21	- 34	- 31	- 17	3	28	37	22	5	1
500	- 23	- 47	- 68	- 62	- 25	23	54	54	32	11	9
300	- 25	- 59	-109	-107	- 31	56	94	82	46	20	19
200	- 42	- 71	-128	-135	- 39	70	122	109	59	26	23
100	- 52	- 94	-119	-103	- 39	23	54	52	30	11	3

OCTOBER

PRES mb	20N	25N	30N	35N	40N	45N	50N	55N	60N	65N	70N
700	- 39	- 43	- 37	- 28	- 21	- 8	21	46	49	39	29
500	- 63	- 63	- 44	- 26	- 13	8	43	67	63	49	44
300	- 92	- 86	- 52	- 9	16	39	70	88	80	63	57
200	-104	- 98	- 57	1	43	64	83	94	85	69	60
100	- 77	- 86	- 65	- 26	13	35	47	54	52	51	57

JANUARY

PRES mb	20N	25N	30N	35N	40N	45N	50N	55N	60N	65N	70N
700	- 77	- 50	- 15	15	30	39	43	37	27	21	19
500	-133	- 57	19	57	70	72	68	51	31	24	26
300	-170	- 96	30	125	146	131	101	63	39	34	39
200	-168	-109	27	150	180	149	108	69	45	40	47
100	-134	- 92	- 2	75	94	79	58	44	41	48	65

APRIL

PRES mb	20N	25N	30N	35N	40N	45N	50N	55N	60N	65N	70N
700	- 65	- 42	- 15	5	17	21	27	29	26	26	31
500	- 84	- 48	- 10	18	35	44	49	47	38	39.	50
300	-105	- 41	18	54	73	80	80	66	49	55	70
200	-123	- 53	39	108	121	102	85	69	53	54	62
100	- 94	- 61	4	59	75	65	51	38	31	35	44

APPENDIX 8

$\{\{\zeta_g\}_{(t)}\}_{(\lambda)}$ in January 1970. Units: $10^{-7}s^{-1}$.

PRES mb	25N	30N	35N	40N	45N	50N	55N	60N	65N	70N	75N
700	186	181	201	229	241	246	241	258	237	234	257
500	251	262	302	354	350	332	326	362	360	343	362
300	354	406	459	515	483	429	402	435	418	401	396
200	373	425	508	493	413	326	295	306	290	280	269
100	256	230	244	251	235	211	185	185	185	178	174

$\{\{\zeta_g\}_{(t)}\}_{(\lambda)}$ for October 1969. Units: $10^{-7}s^{-1}$.

PRES mb	25N	30N	35N	40N	45N	50N	55N	60N	65N	70N	75N
700	163	173	180	196	231	261	244	229	201	184	194
500	204	235	264	294	352	374	344	324	284	259	265
400	240	288	318	368	439	464	428	395	352	319	317
300	279	359	387	445	524	558	502	461	413	380	368
200	317	387	420	451	493	482	403	357	319	284	266
100	232	215	213	192	203	195	177	168	165	156	147

APPENDIX 9

$\{\{\zeta_g\}_{(\lambda)}\}$ (t) in units: $10^{-4} s^{-1}$

JULY 1969

PRES mb	25N	30N	35N	40N	45N	50N	55N	60N	65N	70N	75N
700	.150	.143	.157	.146	.167	.196	.197	.203	.191	.174	.189
500	.178	.175	.213	.215	.238	.274	.269	.273	.258	.250	.254
400	.200	.218	.259	.277	.303	.339	.327	.333	.313	.310	.307
300	.241	.285	.334	.375	.403	.431	.405	.408	.380	.377	.362
200	.299	.345	.388	.441	.432	.427	.350	.315	.264	.245	.230
100	.235	.222	.208	.166	.153	.140	.121	.105	.089	.076	.079

OCTOBER 1969

PRES mb	25N	30N	35N	40N	45N	50N	55N	60N	65N	70N	75N
700	.163	.177	.180	.195	.232	.262	.245	.230	.199	.183	.193
500	.205	.239	.264	.291	.353	.375	.345	.323	.281	.258	.261
400	.239	.290	.320	.364	.443	.466	.430	.395	.349	.317	.313
300	.280	.360	.388	.439	.529	.561	.505	.460	.409	.376	.364
200	.315	.390	.420	.449	.496	.486	.404	.357	.315	.281	.264
100	.229	.217	.214	.192	.204	.196	.178	.167	.164	.153	.144

JANUARY 1970

PRES mb	25N	30N	35N	40N	45N	50N	55N	60N	65N	70N	75N
700	.186	.180	.200	.226	.245	.247	.239	.252	.240	.238	.259
500	.251	.259	.300	.352	.351	.329	.321	.356	.365	.352	.369
400	.298	.334	.370	.442	.418	.388	.376	.417	.417	.398	.404
300	.355	.403	.459	.513	.486	.423	.397	.430	.425	.409	.406
200	.374	.422	.512	.492	.413	.321	.289	.304	.295	.288	.274
100	.257	.229	.245	.253	.236	.210	.182	.183	.186	.179	.173

APRIL 1970

PRES mb	25N	30N	35N	40N	45N	50N	55N	60N	65N	70N	75N
700	.158	.177	.187	.198	.243	.257	.230	.202	.184	.172	.210
500	.219	.251	.289	.292	.355	.349	.311	.291	.271	.267	.327
400	.272	.316	.357	.370	.438	.423	.381	.354	.330	.327	.382
300	.334	.39]	.436	.453	.513	.491	.431	.396	.355	.346	.368
200	.370	.430	.457	.443	.443	.390	.304	.270	.228	.225	.231
100	.237	.216	.209	.204	.184	.171	.145	.119	.113	.124	.138

A Note on the Illustrations:

In the computer analyzed maps of $[\zeta_g]_{(t)}$ and $\{\zeta_g\}_{(t)}$ the analyses are not valid north of 75N and south of 25N, being merely extrapolations of the values at 75N and 25N respectively.
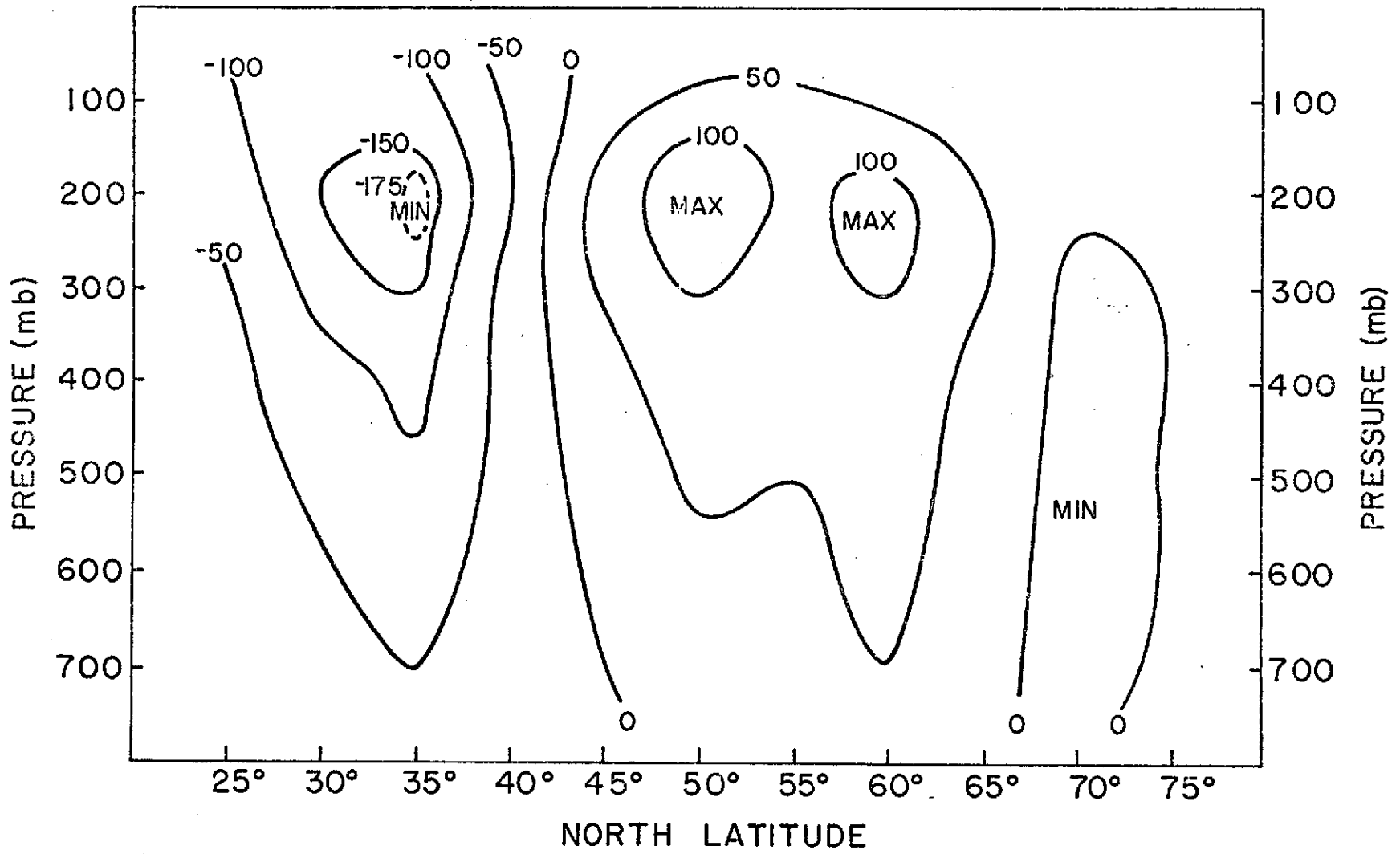
Figure 1a. The distribution of $[\zeta_g]_{(t,\lambda)}$ in July 1969. Units: $10^{-7}s^{-1}$.
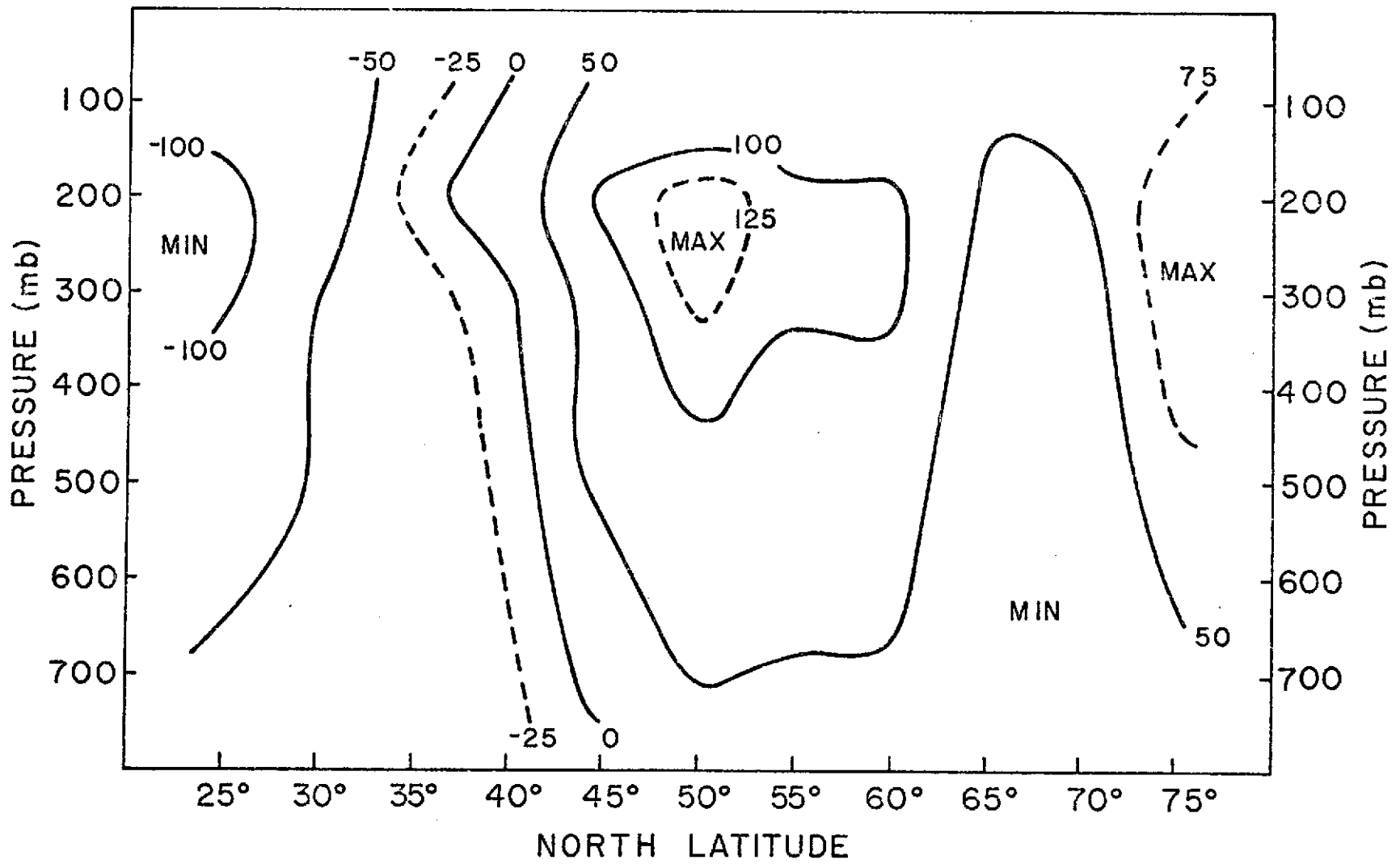
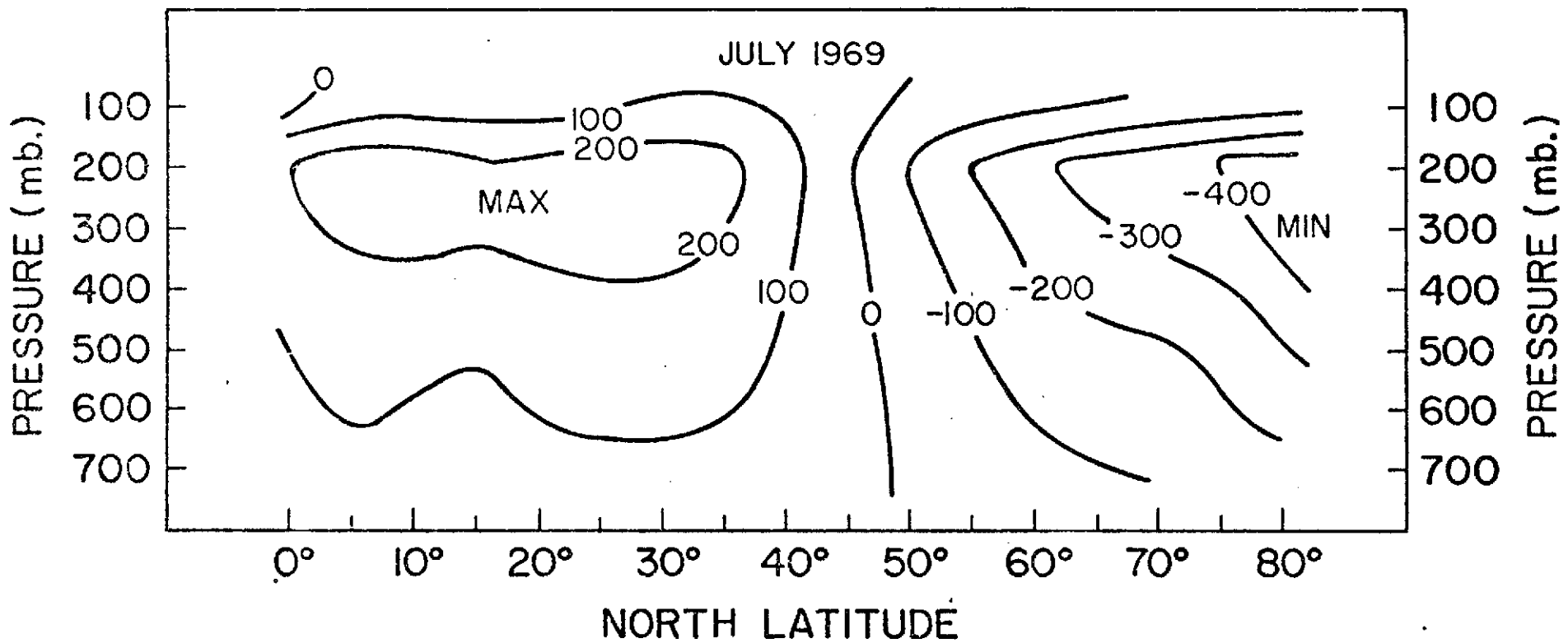Figure 1b. The distribution of $[\zeta_g]_{(t,\lambda)}$ in October 1969. Units: 10^{-7}s^{-1}.
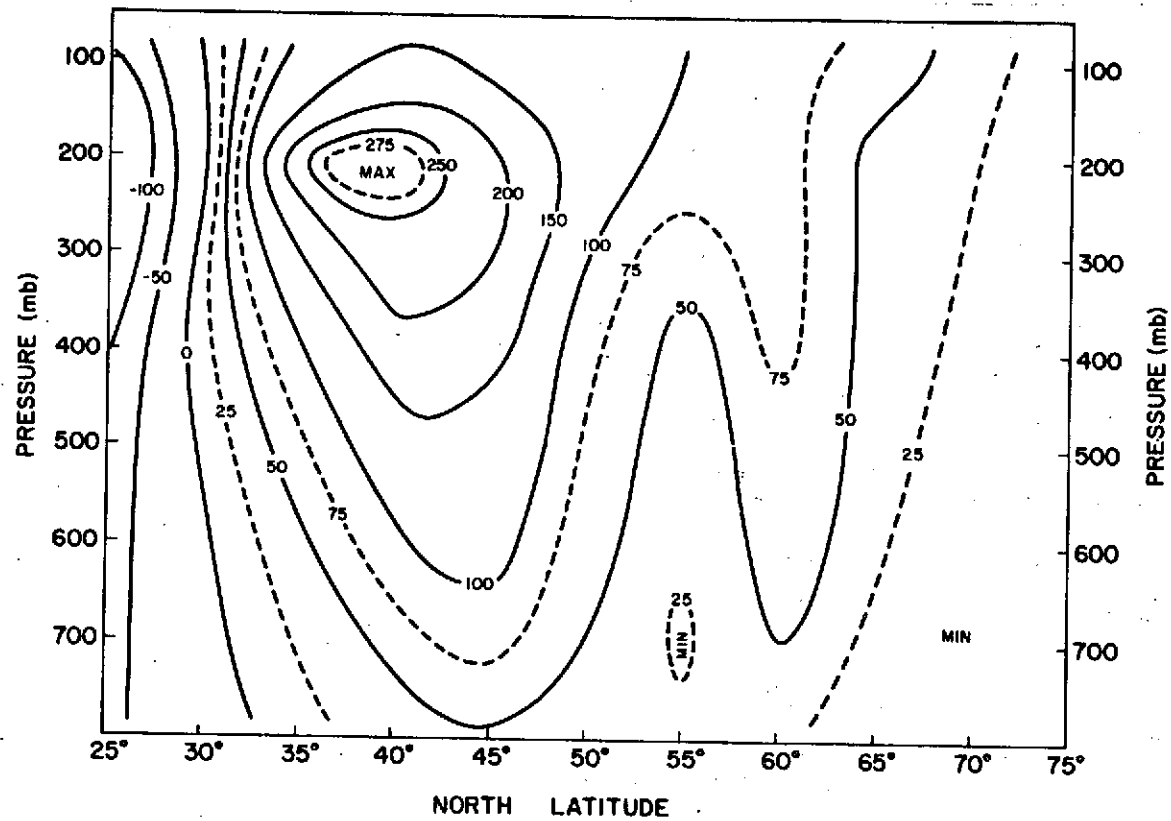
Figure 1c. The distribution of $[\zeta_g]_{(t,\lambda)}$ in January 1970. Units: $10^{-7} s^{-1}$.
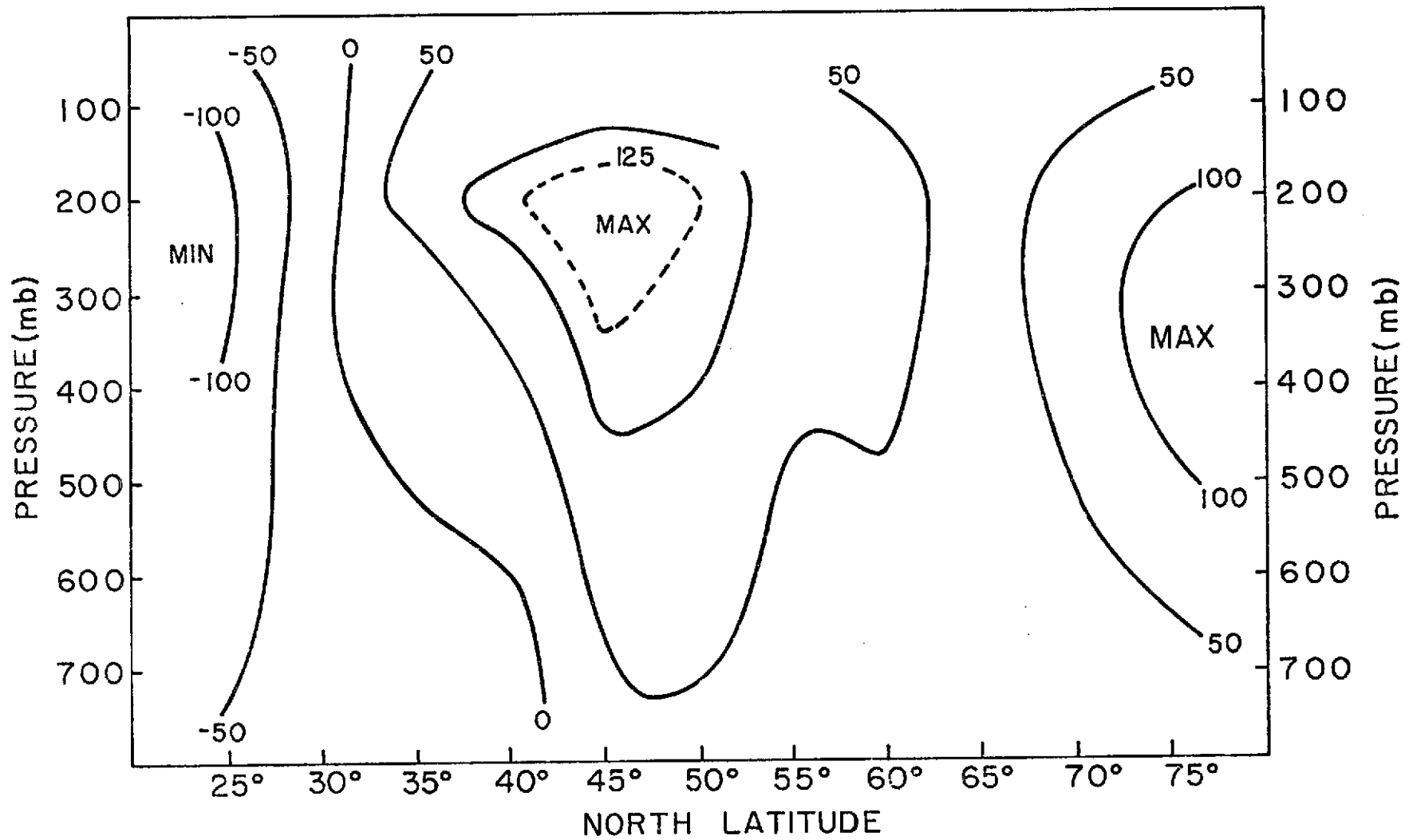
Figure 1d. The distribution of $[\zeta_g]_{(t,\lambda)}$ in April 1970. Units: $10^{-7}s^{-1}$.

JULY 1969

0

100

200

MAX

200

100

0

-100

-200

-300

-400

MIN

PRESSURE (mb.)

100
200
300
400
500
600
700

PRESSURE (mb.)

100
200
300
400
500
600
700

0° 10° 20° 30° 40° 50° 60° 70° 80°

NORTH LATITUDE

53

Figure 2a. The distribution of $[H]_{(t,\lambda)} - [H]_{(t,\lambda,\phi)}$ in July 1969. Units: geopotential meters.
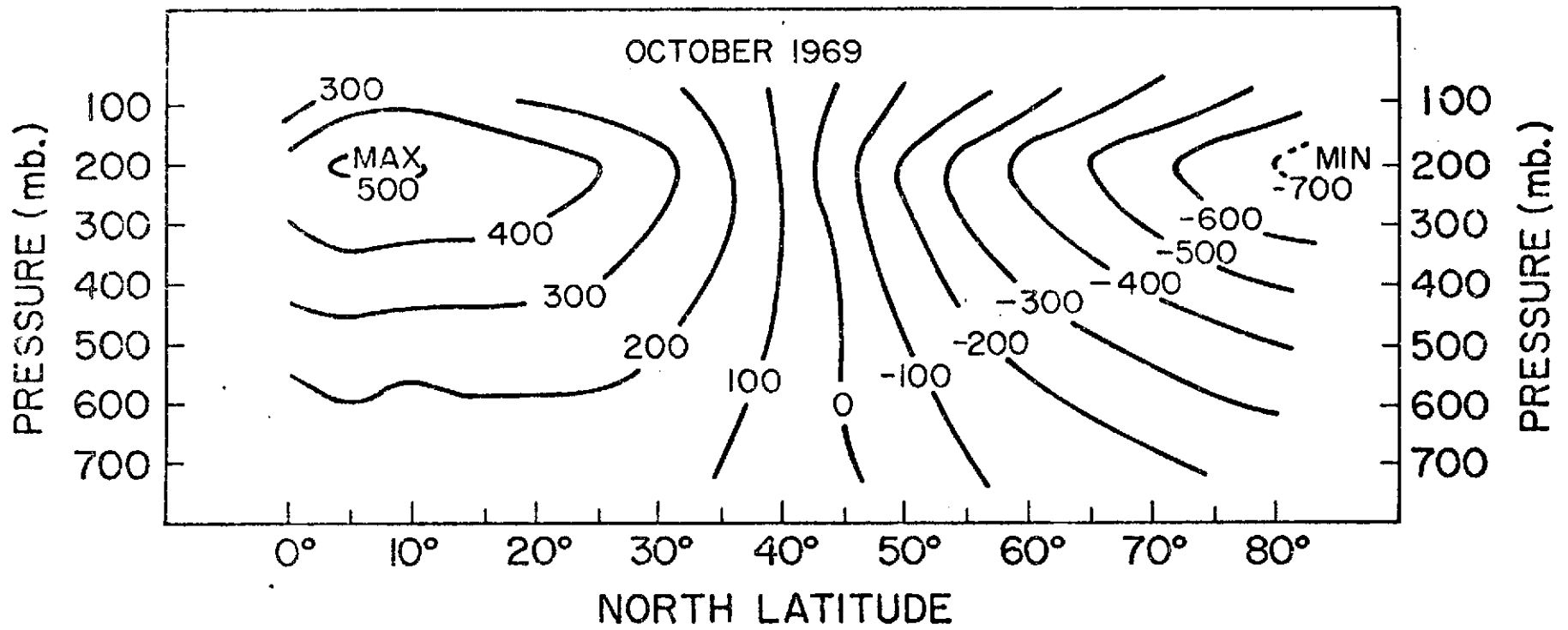
Figure 2b. The distribution of $[H]_{(t,\lambda)} - [H]_{(t,\lambda,\phi)}$ in October 1969. Units: geopotential meters.
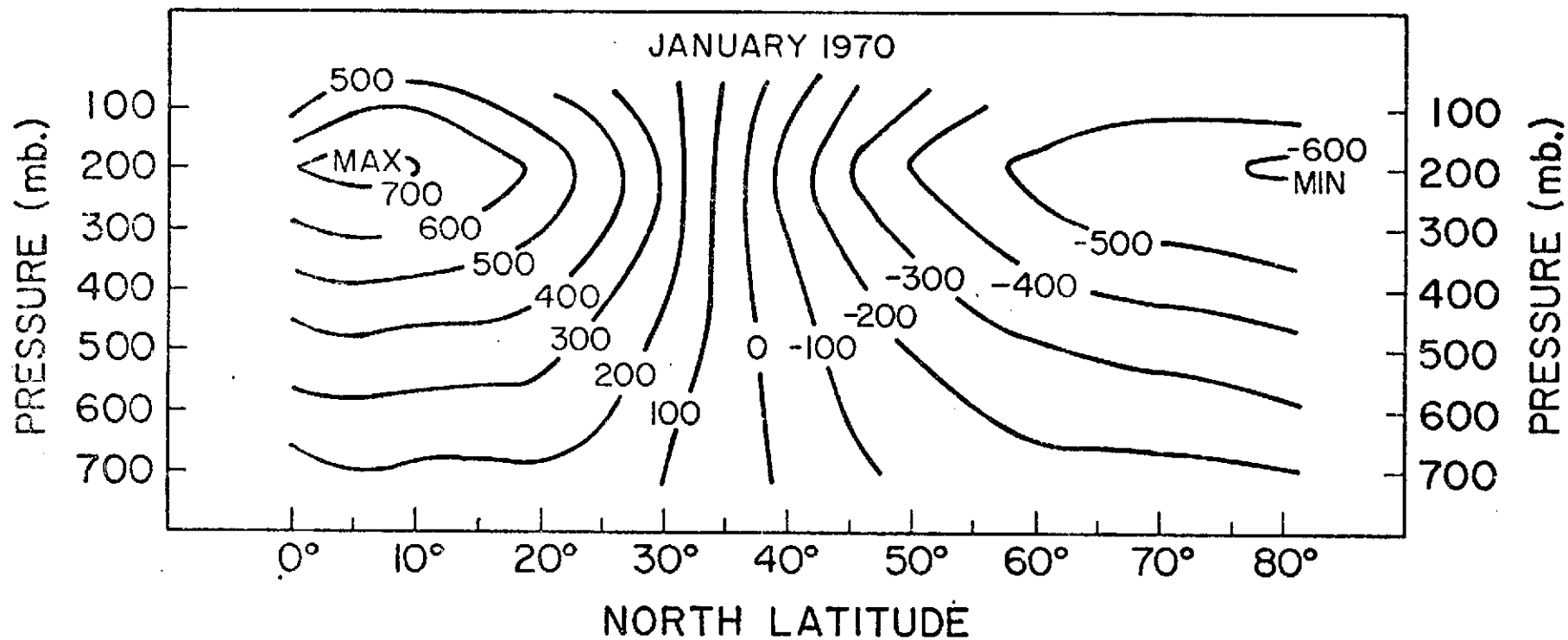
Figure 2c.   The distribution of $[H]_{(t,\lambda)} - [H]_{(t,\lambda,\phi)}$ in January 1970.   Units: geopotential meters.
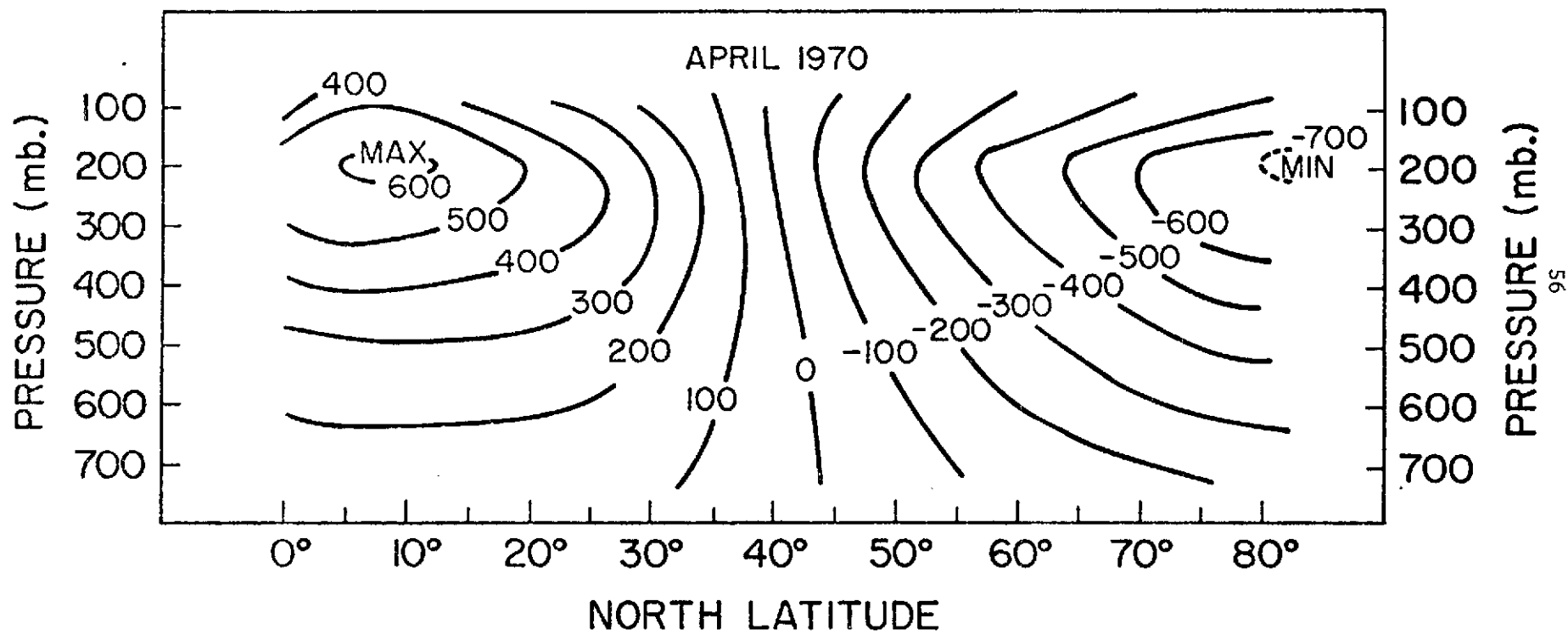
Figure 2d. The distribution of $[H]_{(t,\lambda)} - [H]_{(t,\lambda,\phi)}$ in April 1970. Units: geopotential meters.
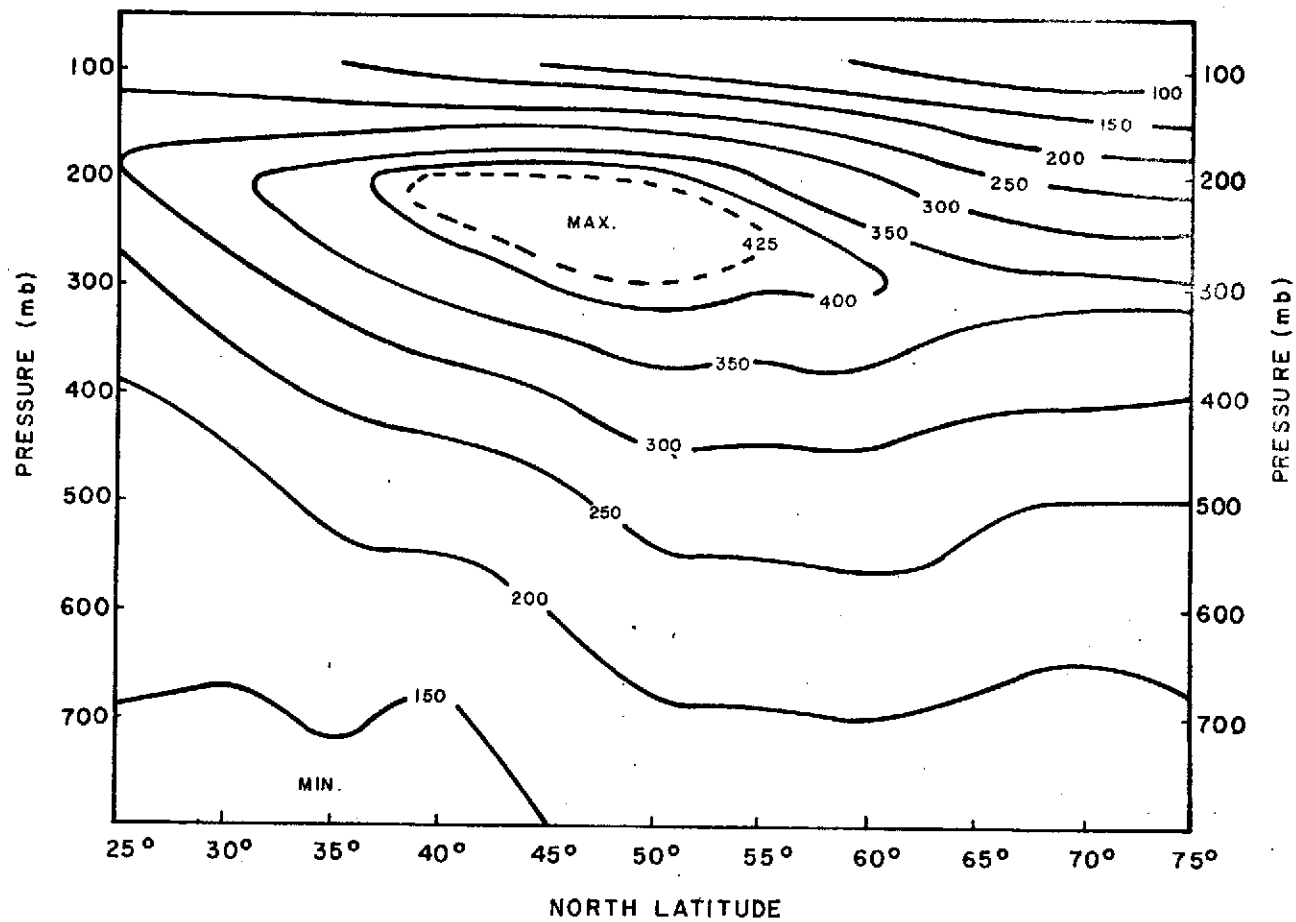
Figure 3a.   The distribution of K in July 1969.
Units: $10^{-7}s^{-1}$.
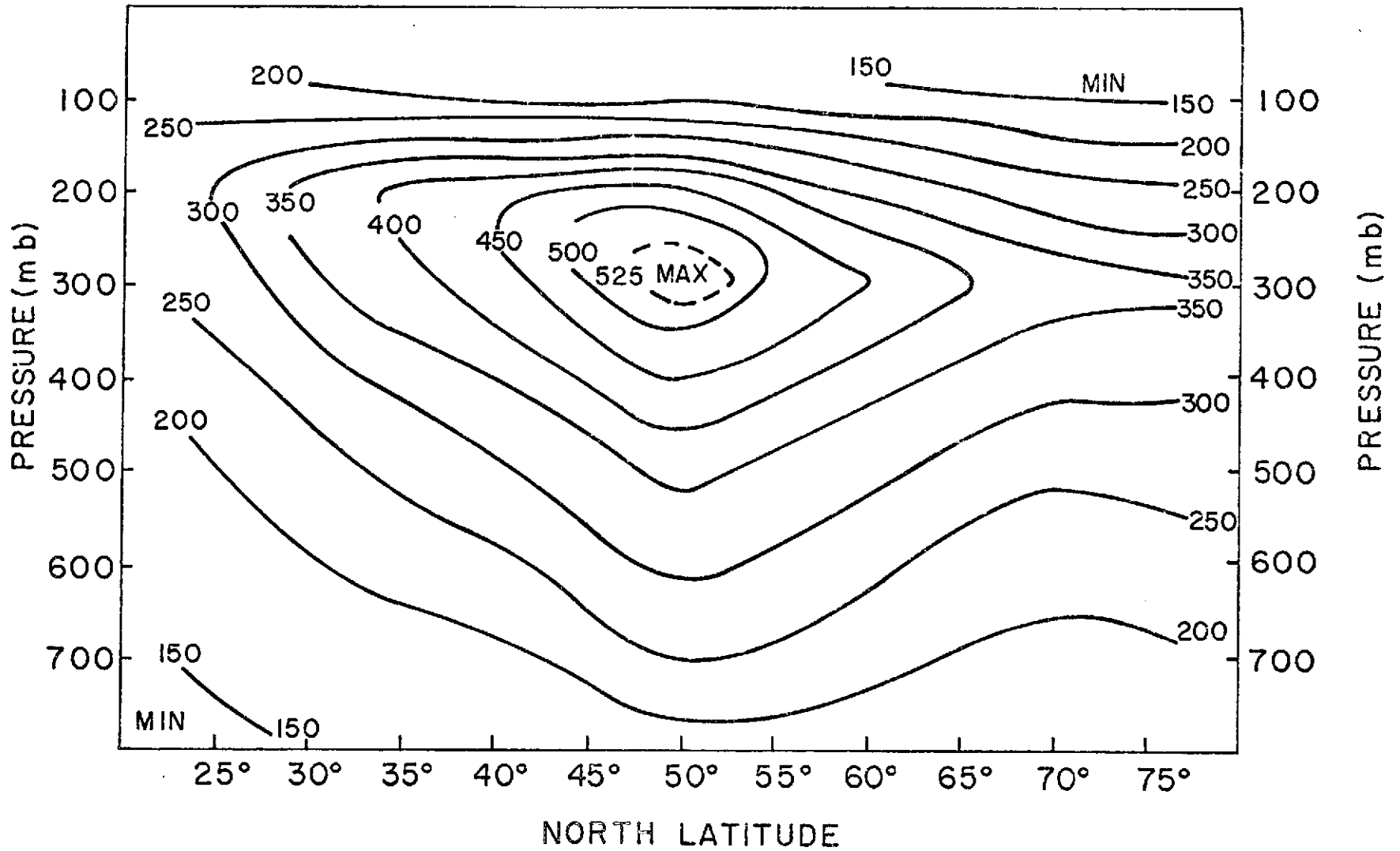
Figure 3b. The distribution of K in October 1969.
Units: $10^{-7}s^{-1}$.
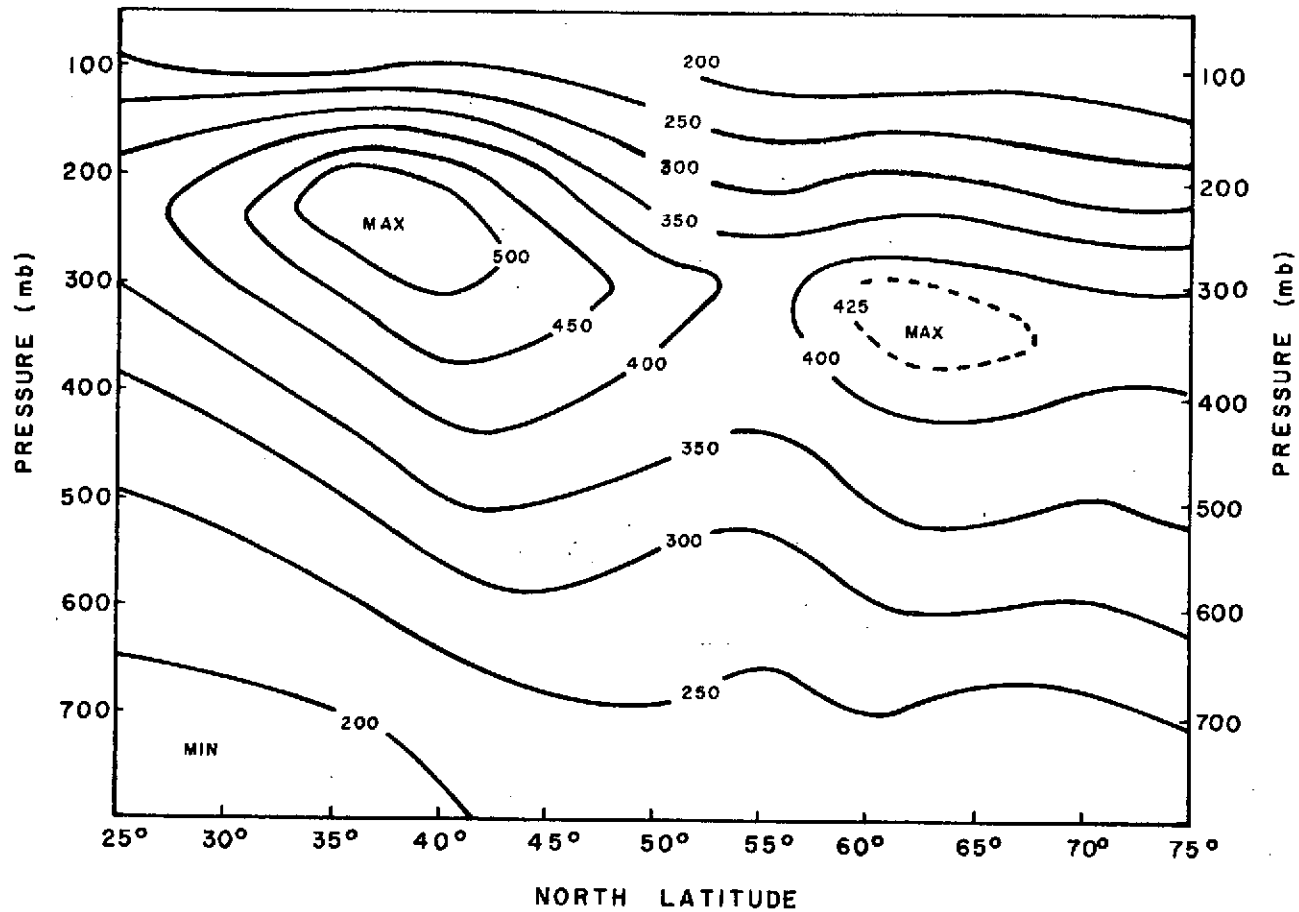
Figure 3c. The distribution of K in January 1970.
Units: $10^{-7} s^{-1}$.
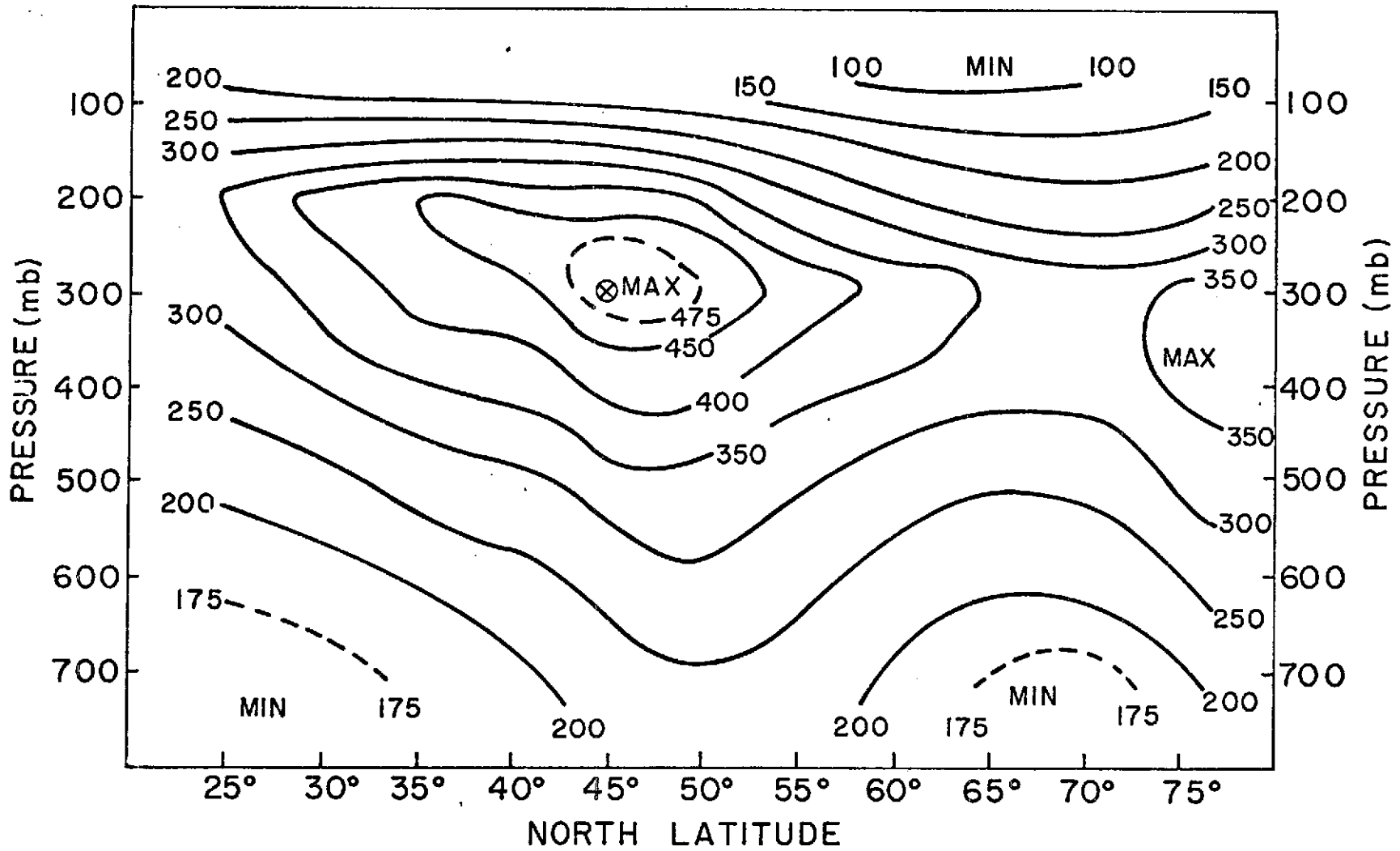
Figure 3d. The distribution of K in April 1970.
Units: $10^{-7}s^{-1}$.
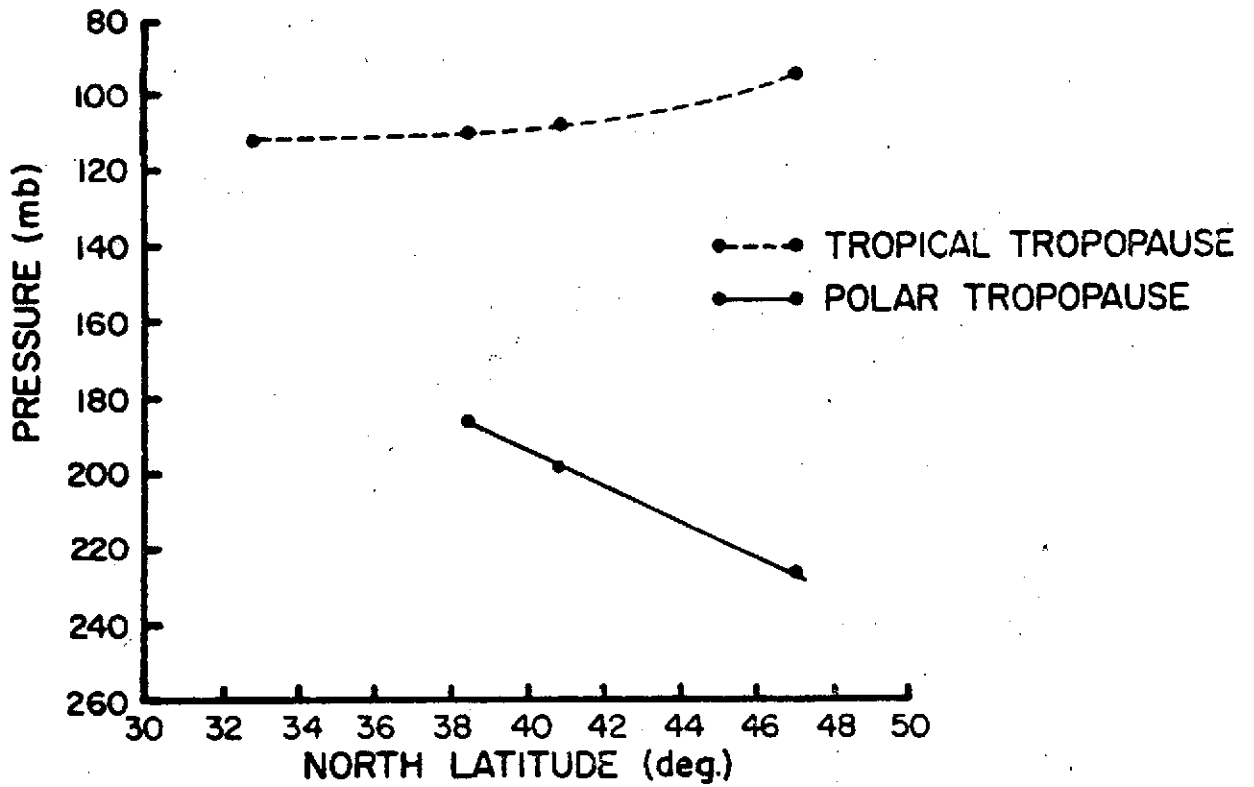
Fig. 3e.- Mean July 1969 tropopauses along North American coastal regions.
A tertiary region of stability exists at about the 140 mb level
at most latitudes considered here.
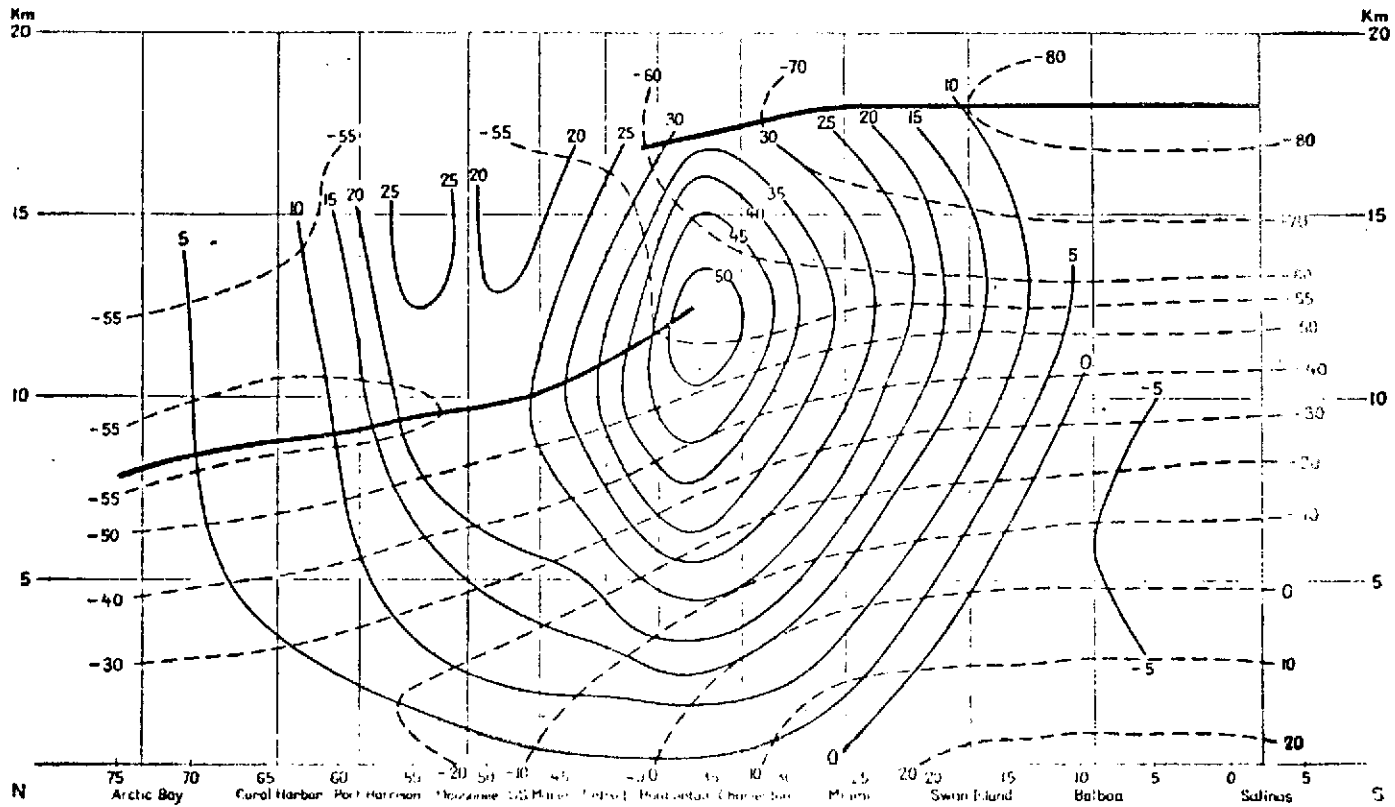
Figure 3f. Observed mean temperatures and mean geostrophic zonal winds, computed from the observed pressure and temperature data in a vertical north-south section through North and Central America. Computed and drawn by Dr. Seymour L. Hess; based on daily radiosonde data for January and February, 1941 through 1945 (winter conditions). (From Rossby (1949).)
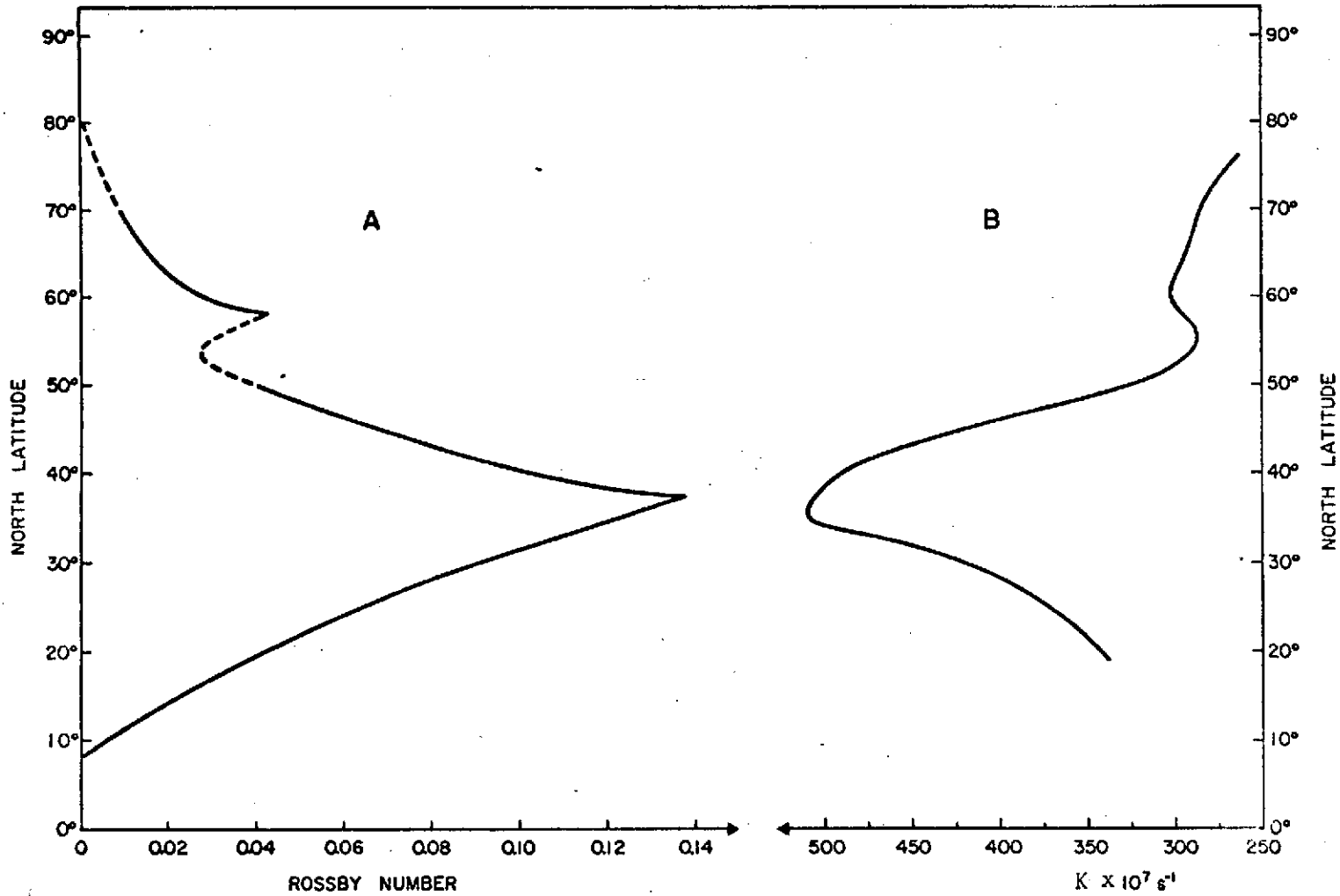
Figure 3g. Mean zonal-wind profile for 12-km level in winter. The data for this curve are taken from the section in Fig. 10. Note the indications of a second, weaker jet near 55N. (After Rossby (1949)).

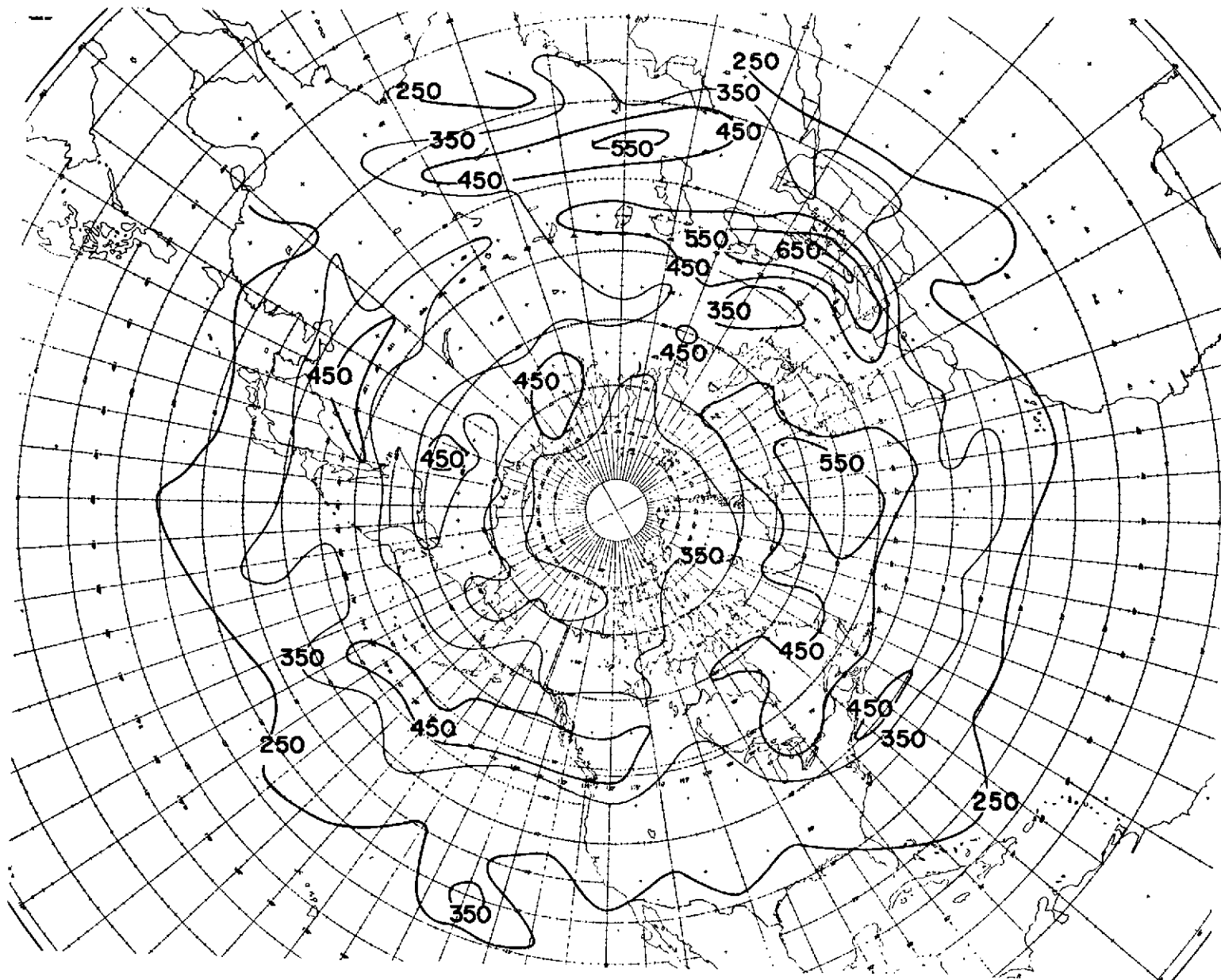Figure 3h. The parameter K at the 200 mb level in January 1970.
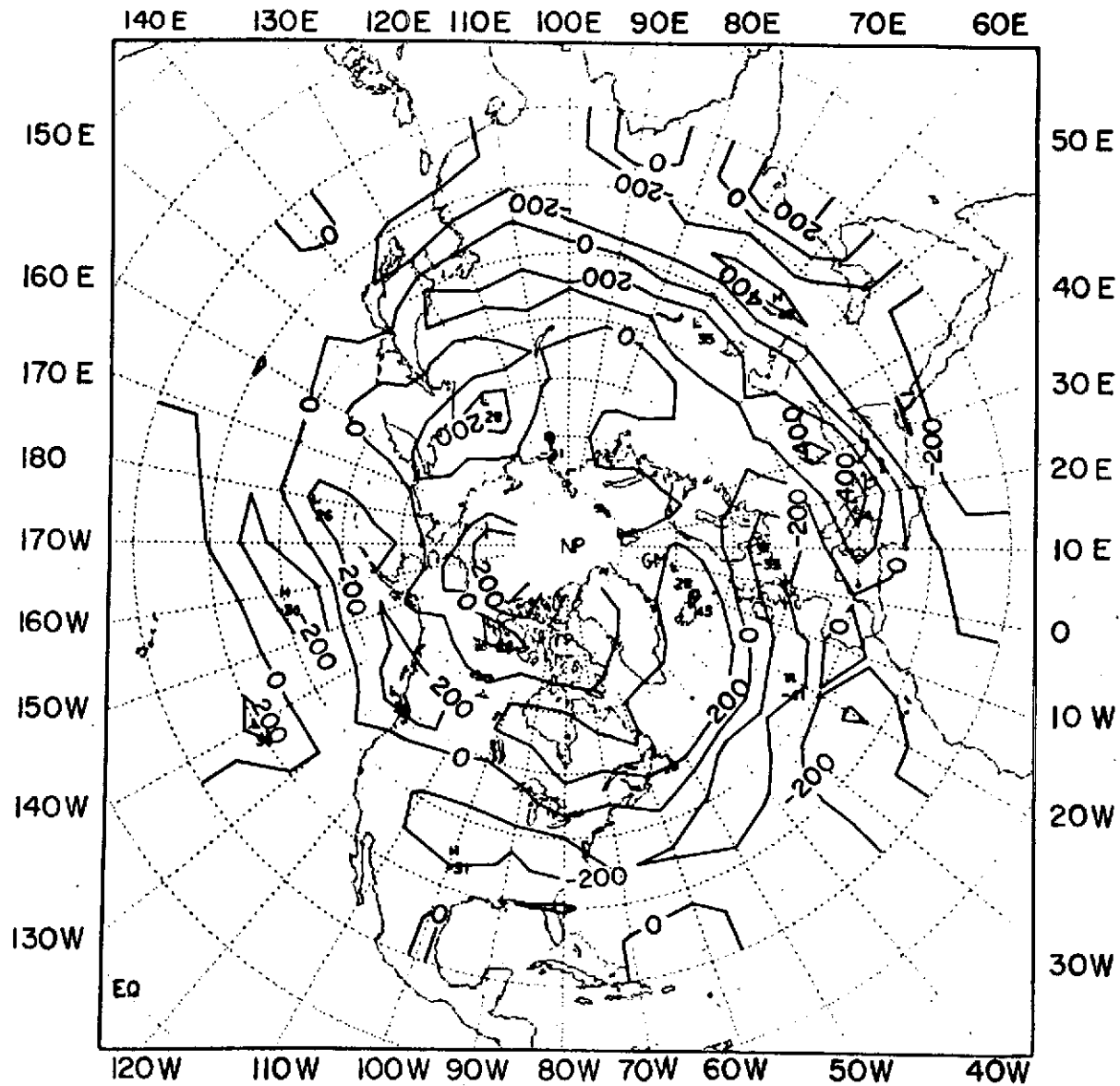
Figure 4a. The geographical distribution of $[\zeta_g]_{(t)}$ in July 1969, at the 300 mb level. Units: $10^{-7}s^{-1}$.
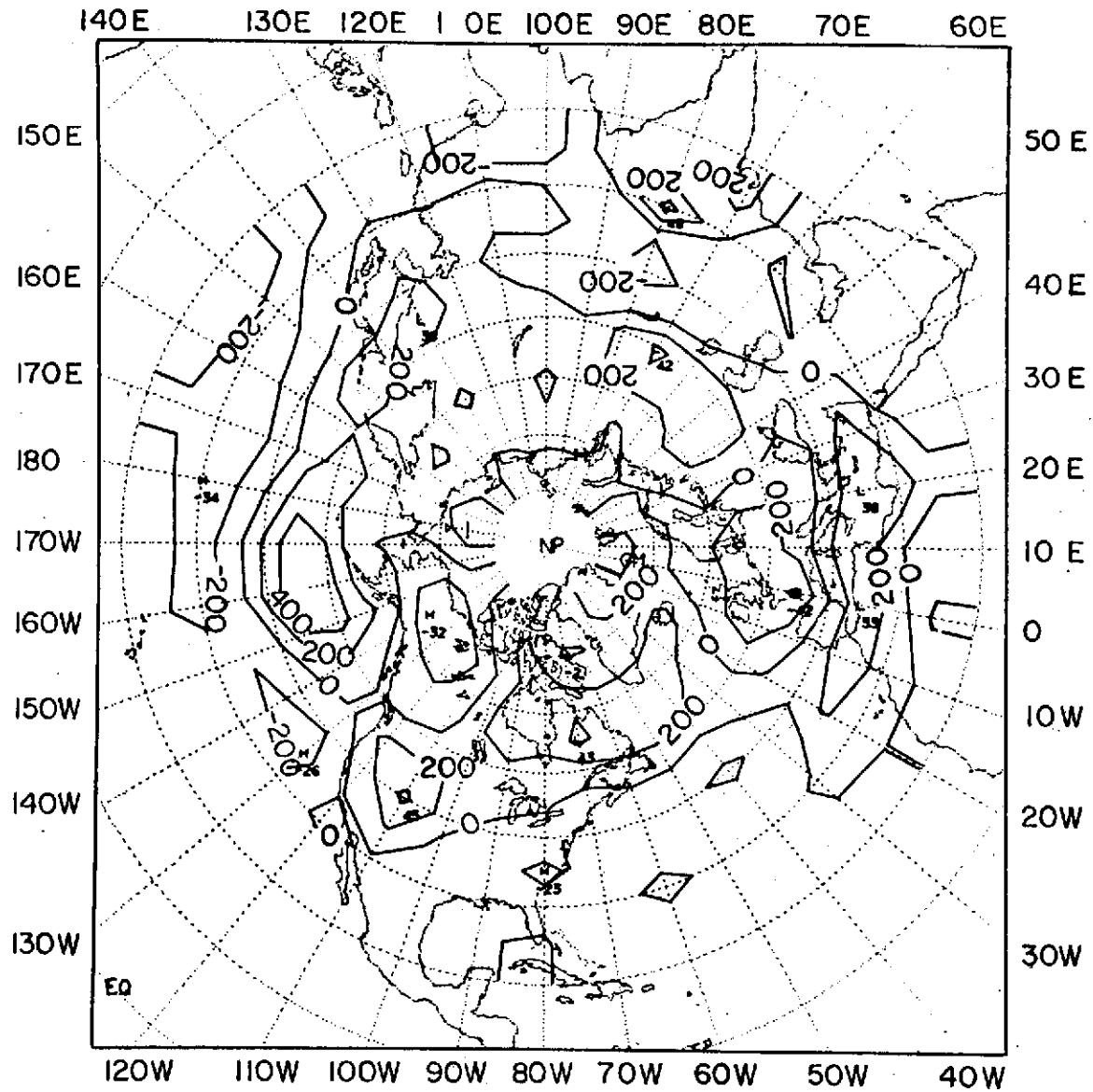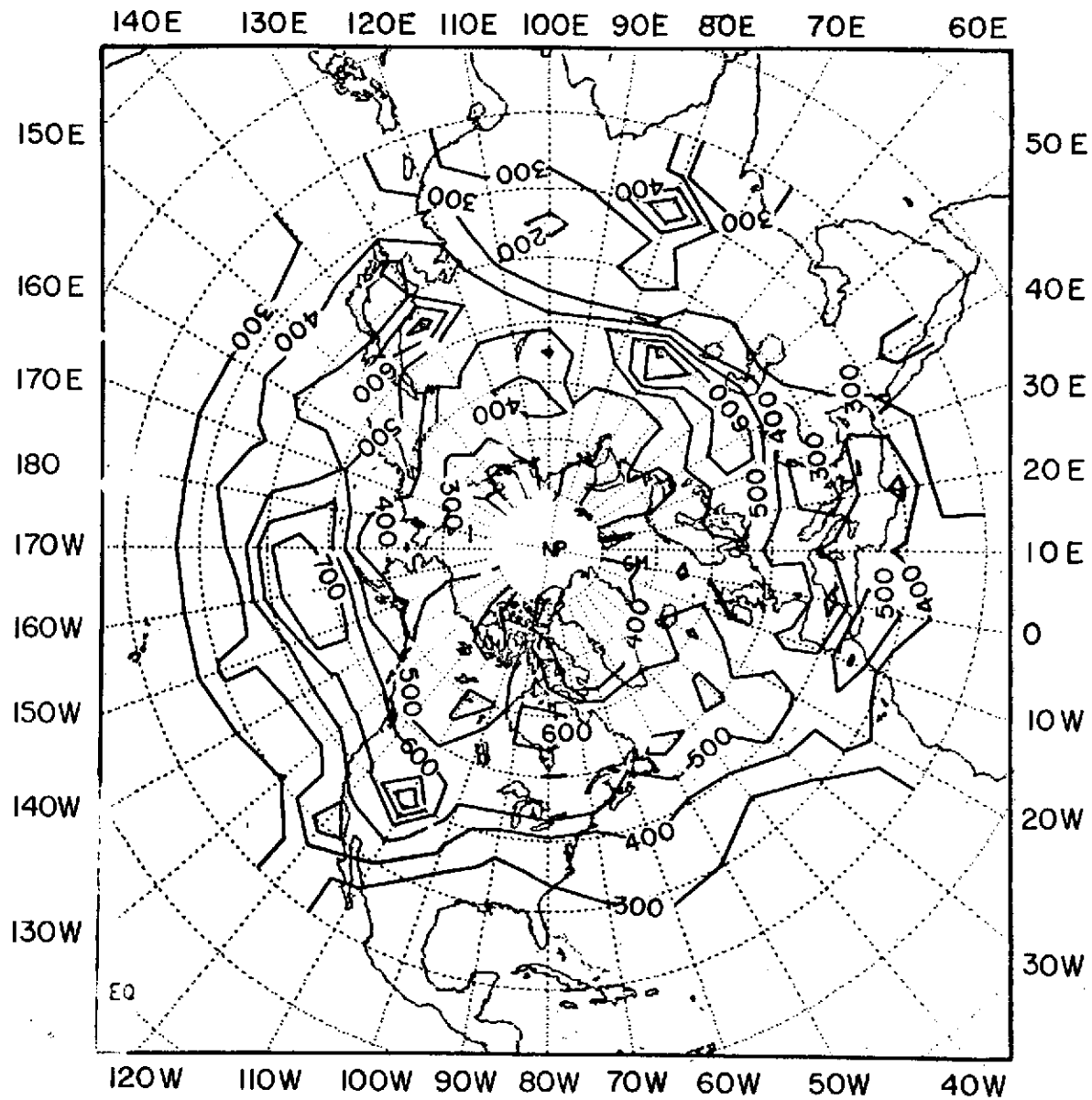
Figure 4b. The geographical distribution of $[\zeta_g]_{(t)}$ in
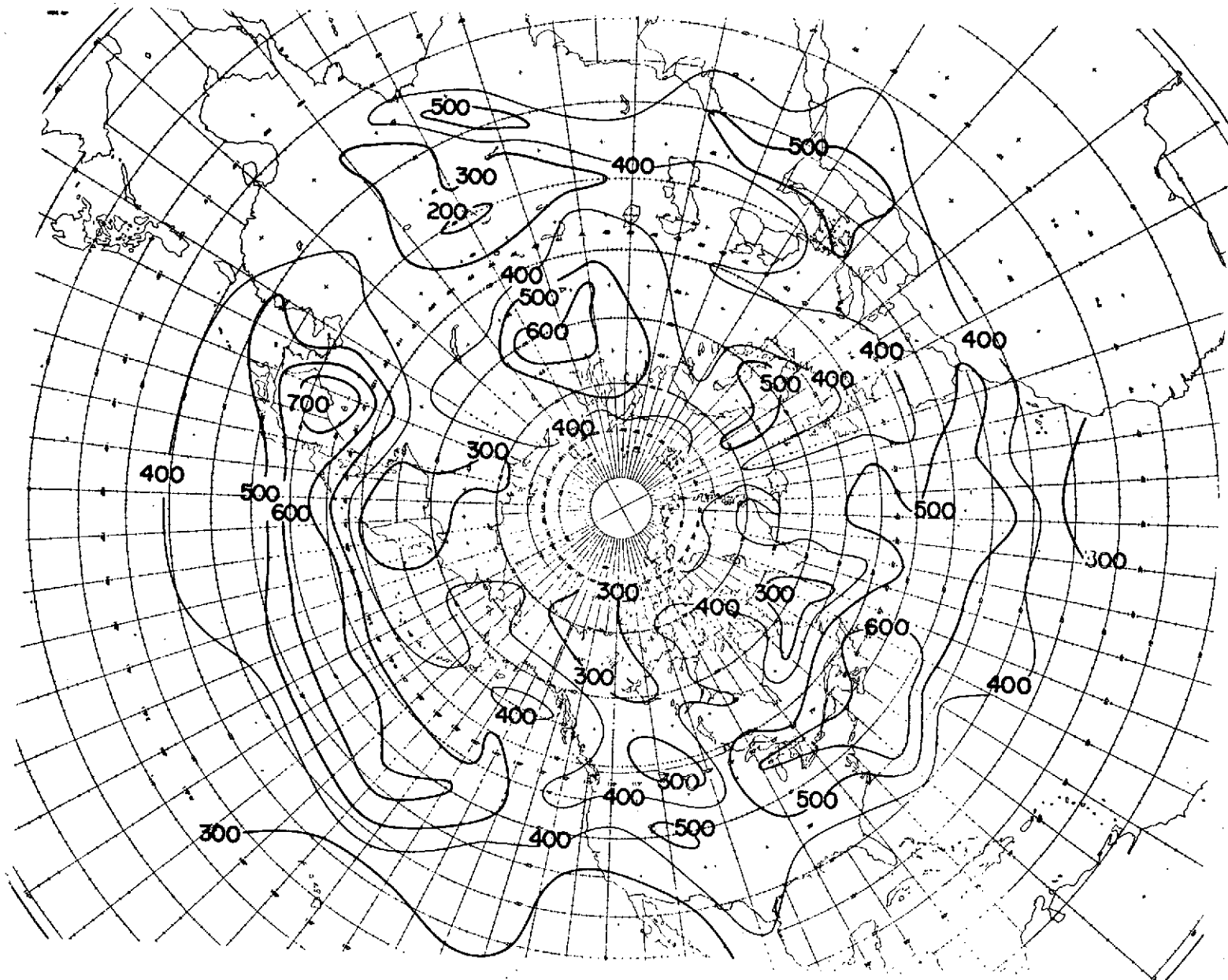October 1969, at the 300 mb level. Units:
$10^{-7} s^{-1}$.
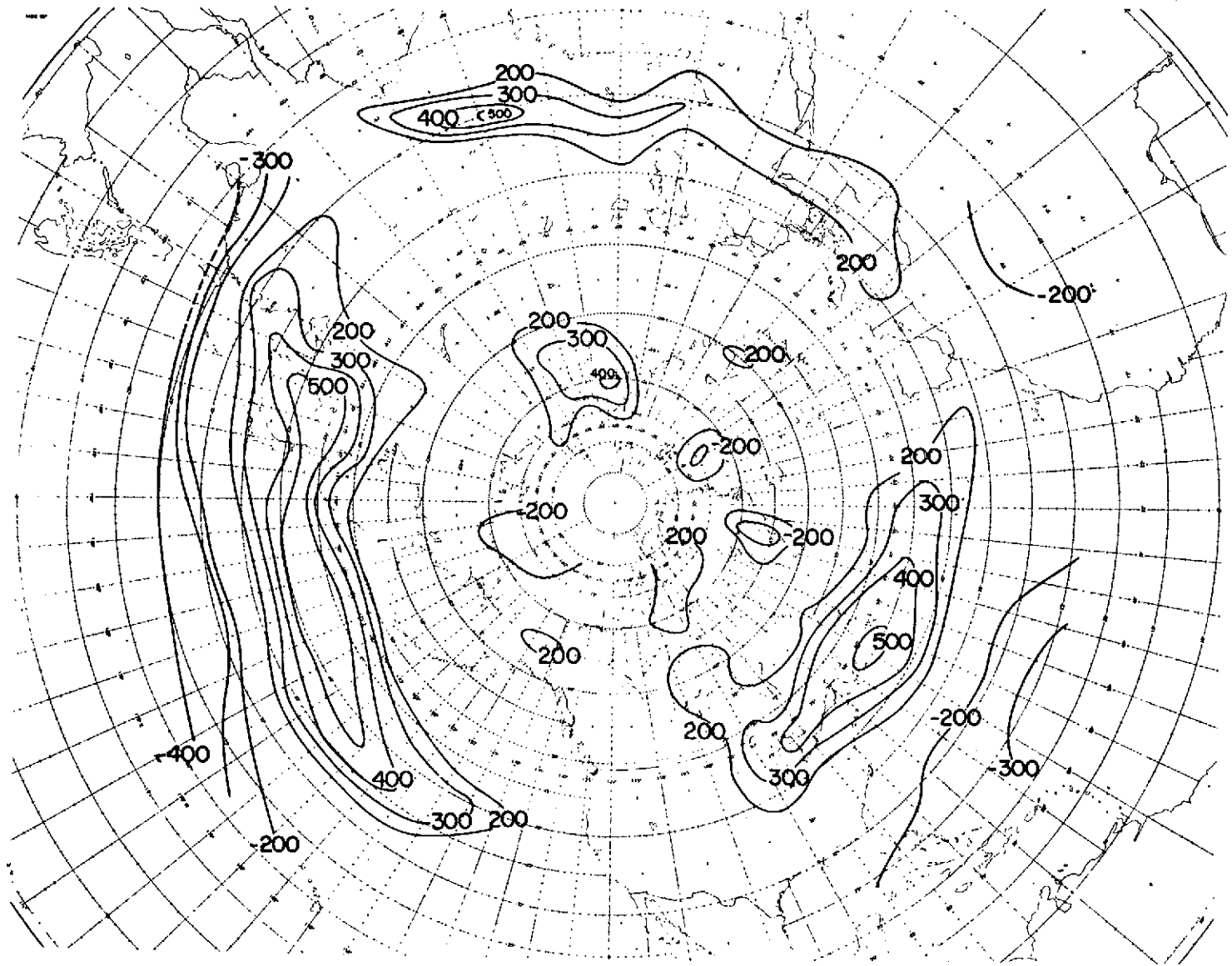
Figure 4c. The geographical distribution of $[\zeta_g]_{(t)}$ in January 1970, at the 300 mb level. Units: $10^{-7} s^{-1}$.
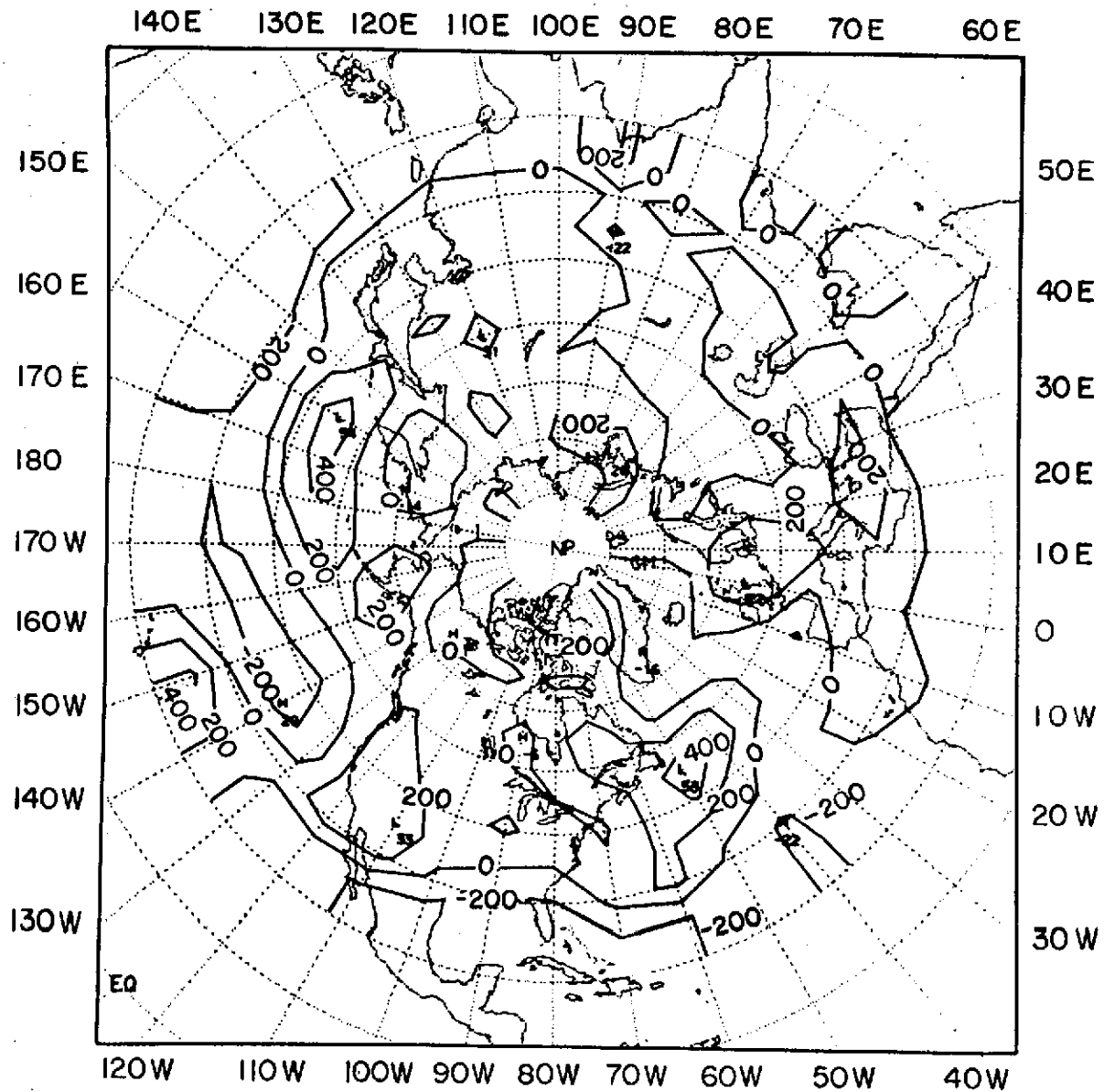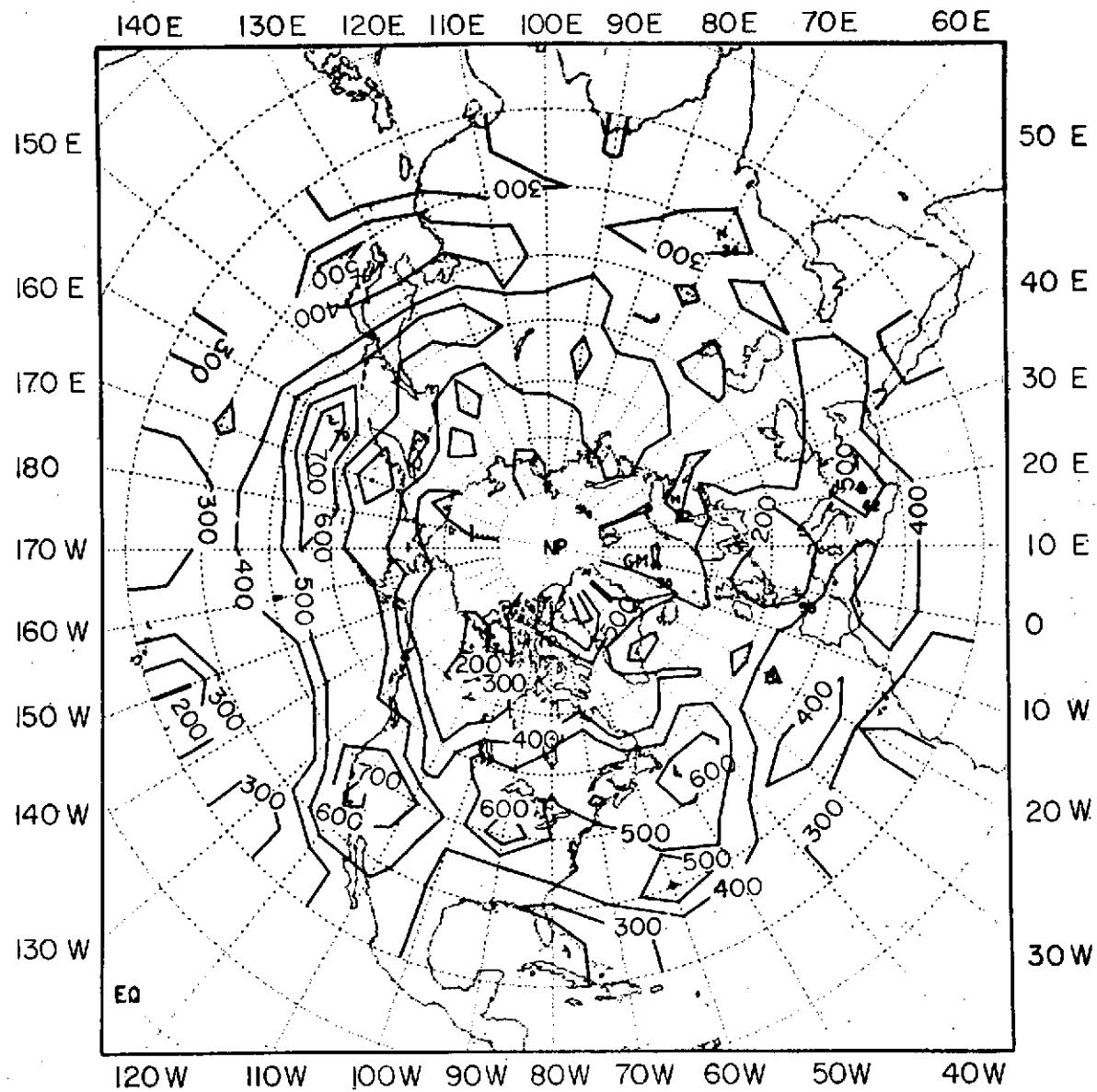
Figure 4d. The geographical distribution of $[\zeta_g]_{(t)}$ in April 1970, at the 300 mb level. Units: $10^{-7}s^{-1}$.

Figure 5a. The geographical distribution of $\{\zeta_g\}_{(t)}$ in July 1969, at the 300 mb level. Units: 10^{-7}s^{-1}.

Figure 5b. The geographical distribution of $\{\zeta_g\}_{(t)}$ in
October 1969, at the 300 mb level. Units:
$10^{-7}s^{-1}$.

Figure 5c. The geographical distribution of $\{\zeta_g\}_{(t)}$ in January 1970, at the 300 mb level. Units: $10^{-7}s^{-1}$.

Figure 5d. The geographical distribution of $\{\zeta_g\}_{(t)}$ in

April 1970, at the 300 mb level. Units:

$10^{-7}s^{-1}$.
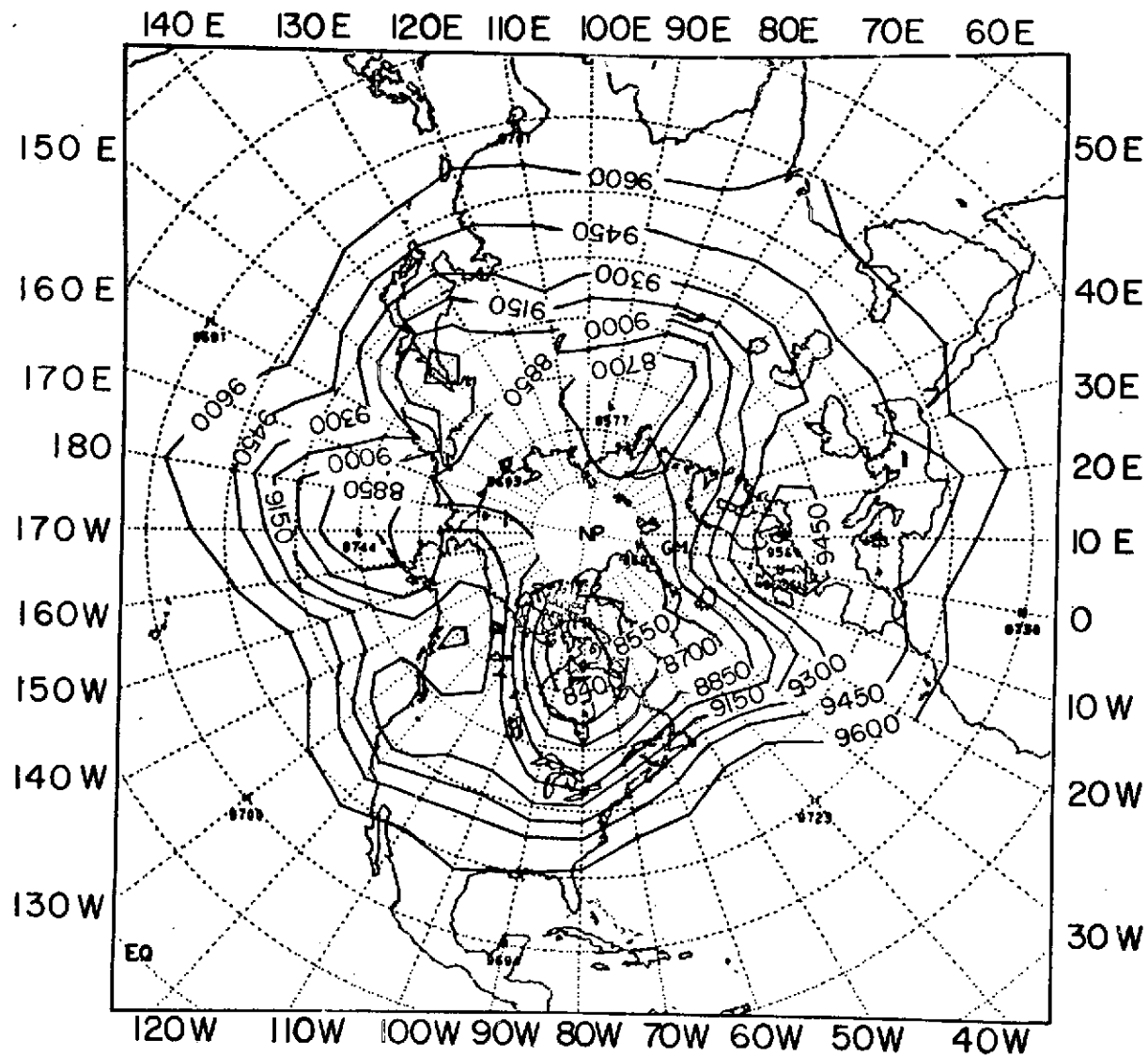
Figure 6. The geopotential height distribution at the 300 mb
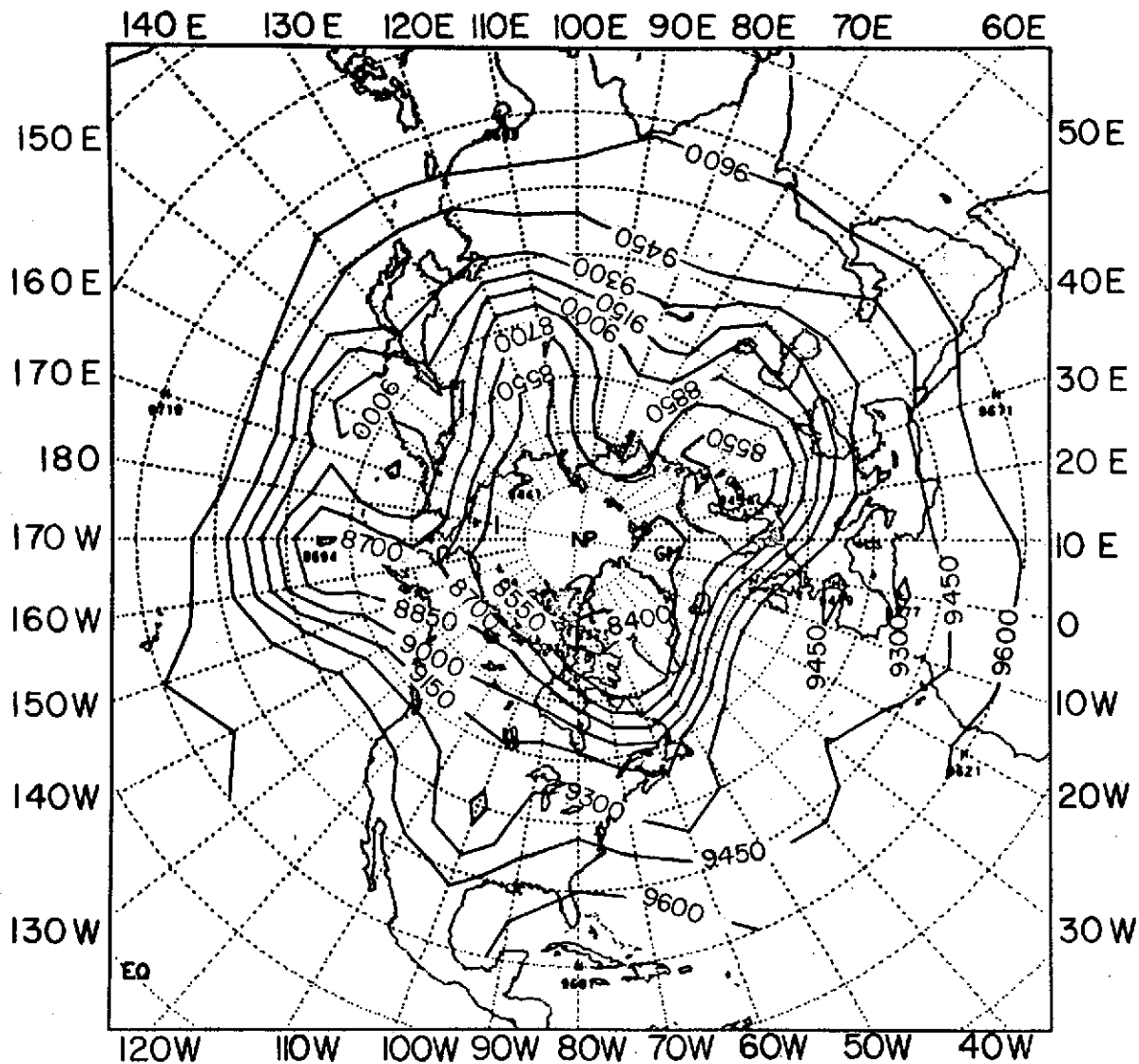level on October 17, 1970. Units: geopotential
meters.

Figure 7. The geopotential height distribution at the 300 mb level on October 30, 1970. Units: geopotential meters.
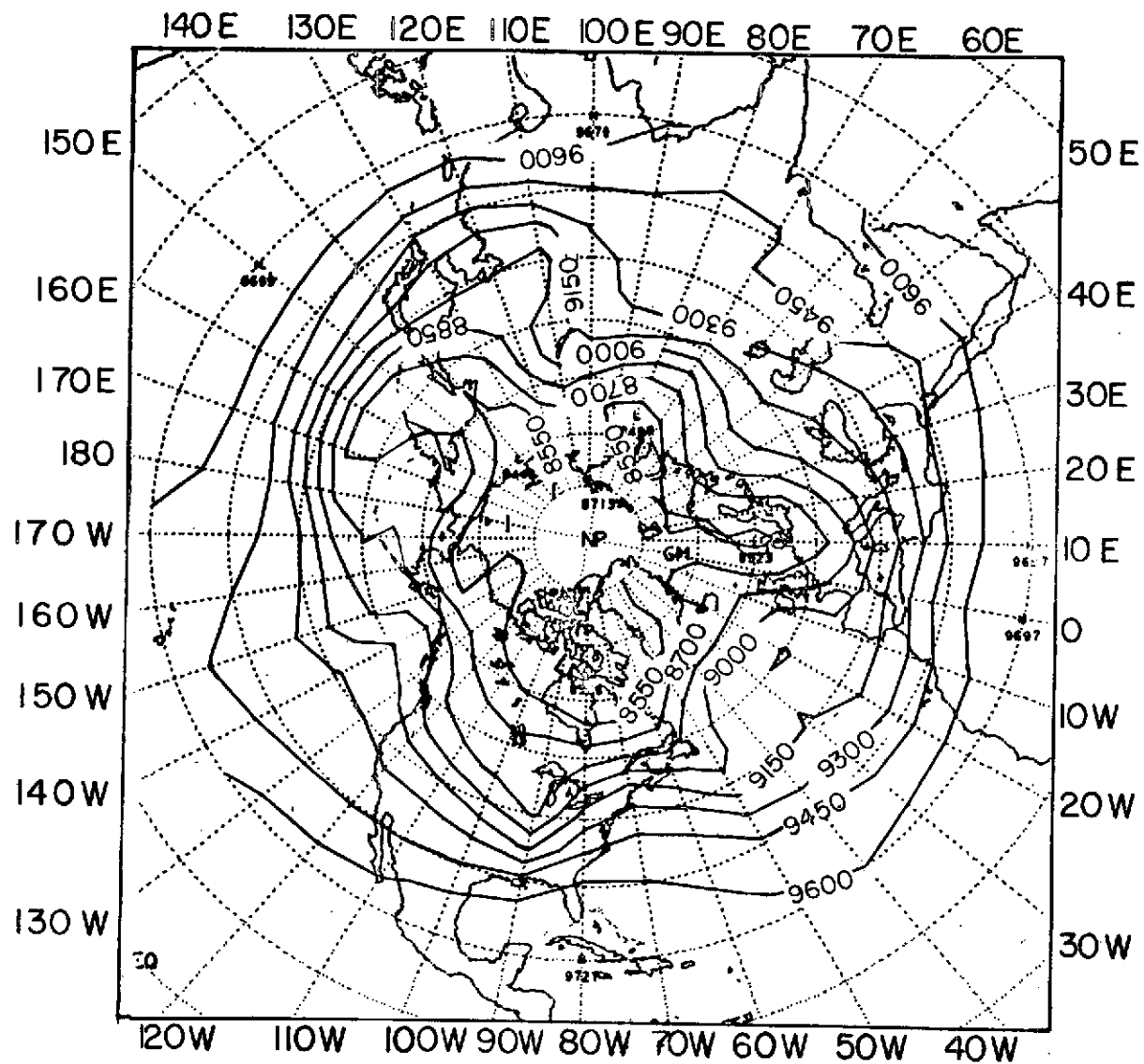
Figure 8. The geopotential height distribution at the 300 mb
level on April 2, 1970. Units: geopotential
meters.